Radiological Assessments for the Neutrino Project: The Cern Neutrino Beam To Gran Sasso

Dissertation

zur Erlangung des Grades eines Doktors
der Technischen Wissenschaften
an der Technischen Universität Graz

vorgelegt von

Dipl. Ing. Herbert Heinz Vincke

am Institut für Theoretische Physik

Begutachter: Ao.Univ.-Prof. DI. Dr. Ewald Schachinger

und Ao.Univ.-Prof. DI. Dr. Peter Kindl

Graz, 1999

2247625

CERN LIBRARIES, GENEVA

CM-P00068929

Contents

CHAPTER 1 1

INTRODUCTION 1

CHAPTER 2 4

PHYSICS AND DESIGN BACKGROUND 4

2.1 NEUTRINO AND NEUTRINO OSCILLATION 4
2.1.1 The Discovery of the Neutrino 4
2.2.2 Neutrino Oscillation 5
2.2 EVIDENCE OF NEUTRINO OSCILLATION 12
2.3 LONG BASELINE NEUTRINO FACILITIES 12
2.4 BEAM REQUIREMENTS 13
2.5 THE CERN NEUTRINO PROGRAMS 14
2.5.1 The West Area Neutrino Facility 14
2.5.2 The NGS-Facility 16
2.6 THE MONTE CARLO CODE FLUKA 26
2.6.1 Non-elastic Nuclear Interactions 26
2.6.2 Isotope Production 28
2.6.3 Elastic Nuclear Interaction 29
2.6.4 Particle Transport in Matter 29
2.6.5 Geometry 34
2.6.6 Biasing 35
2.6.7 Tracking 35
2.6.8 Scoring 35
2.6.9 Applications 36

CHAPTER 3 37

PRODUCTION OF RADIOACTIVE ISOTOPES IN MOLASSE 37

3.1 MOLASSE SAMPLES 37
3.2 IRRADIATION 38
3.3 DETAILS OF THE SIMULATIONS 42
3.4 GAMMA SPECTROSCOPY 45
3.5 ACTIVITIES IN THE MOLASSE SAMPLES 45
3.5.1 Natural Radioactivity 45
3.5.2 Induced Radioactivity 46

3.6 Results of the Monte-Carlo Calculations 48
3.6.1 Star Density *48*
3.6.2 Residual Nuclei *49*
3.6.3 Track-lengths *49*
3.7 Production of Radioactive Isotopes in Molasse per Star 52

CHAPTER 4 55

SIMULATIONS 55

4.1 NGS-Simulations 55
4.2 From NGS-98 to NGS-99 57

CHAPTER 5 73

RADIOLOGICAL PARAMETERS 73

5.1 Radioactivity in the Molasse-Rock 73
NGS-98 ..... *73*
NGS-99 ..... *74*
5.2 Radioactivity in the Concrete Walls 78
NGS-98 ..... *78*
NGS-99 ..... *78*
5.3 Radioactivity in the Groundwater 83
5.4 Determination of Radioactivity in the Air 85
5.5 Tritium Production in the Helium Circuits 100
5.6 Activity in Iron 102
5.7 Activity in the Graphite Core 111
5.8 Activity in the Aluminum 113
5.9 Activity in the Cooling Water 114
5.10 Activity in the Concrete Shielding Blocks 117
5.11 Activity in the Marble 118
5.12 Dose-rates from Neutrinos 119
5.12.1 Neutrino Fluence *119*
5.12.2 Dose Rates for NGS-99 ..... *121*

CHAPTER 6 123

SUMMARY 123

Appendix A 126
Reference parameter list (NGS-98) *126*
Updated Reference Parameter List (NGS-99) *129*
Appendix B 133
Decay data for isotopes produced in molasse *133*
Appendix C 136
Neutron capture cross-sections *136*

BIBLIOGRAPHY 139

ACKNOWLEDGMENTS 145

Chapter 1

Introduction

The Standard Model (SM), which is a combination of the Glashow-Weinberg-Salam theory [Gla69] of electroweak interactions and the Quantum Chromo-Dynamics (QCD), is one of the greatest achievements of particle physics in the 20th century. However, the Standard Model cannot be the final theory of elementary particles physics because it is a theory of weak, electromagnetic and strong interactions but with the exception of gravity. At the moment major efforts are directed towards the search for a theory of elementary particles that could generalize the Standard Model. Most of these theories predict non-zero neutrino mass whereas within the Standard model, neutrinos are considered to be massless. Nevertheless, recent results of a non-zero neutrino mass force revisions in the Standard Model.

The mass of neutrinos and the possibility of their oscillations have been eluding researchers for many years. From their first hypothetical introduction by Pauli in 1930, in order to explain the energy missing in neutron decay, it was obvious that neutrinos have little or no mass. The whole case was largely a phenomenon until the famous experiment of Ray Davis in the gold mine in South Dakota which revealed that there were less electron neutrinos than predicted by solar models. Neutrino oscillations were immediately suspected as the cause of this deficit, but it has not been proved even until today.

Many experiments aimed at directly measuring neutrino mass, which is a very difficult task. They only produced upper limits of a few eV in neutrino mass. Indeed, cosmology tells us that the sum of the masses of all sequential neutrino flavours cannot be more than about 40 eV [Raf97] otherwise the universe would have collapsed already. It is noteworthy that even tiny nonzero neutrino masses could result in an important neutrino contribution to the mass density of the universe.

In view of recently obtained data, namely, that neutrinos have a non-zero mass, coming from Super-Kamiokande detector, 1000 meters underground in a Japanese mine, it is tempting to confirm in an unambiguous way that neutrino oscillations are indeed the cause of the effects seen in the atmospheric neutrino experiments. If this turns out to be the case, the next task will be to measure with great accuracy the oscillation parameters. At present, the experimental motivation for accelerator based neutrino oscillations continues to grow, and the scientific community is discussing the best experimental strategy to accomplish this task.

One of the most promising projects in Europe is the Neutrino Beam to Gran Sasso experiment (NGS) at the European Particles Physics Laboratory CERN near Geneva in Switzerland. Typically, searching for possible neutrino oscillations implies the need for a high-energy beam and a massive detector to maximize the neutrino interaction probability.

The NGS project at CERN will produce a high-energy beam of neutrinos to enable long baseline experiments whose primary goal is to detect and study neutrino oscillations. Therefore, a beam of protons from the Super Proton Synchrotron (SPS) will be used to produce the neutrino beam. Interactions of the proton beam in a target will produce mesons which decay to muons and neutrinos during their flight through the decay tunnel. A hadron stopper downstream of the decay region will remove the remaining protons and mesons from the beam. An intervening shield will absorb the muons while the neutrinos continue through it to the detectors at the Gran Sasso National Laboratory, 732 km away from CERN.

In this work two aspects being important for this particular project are discussed:

1. The Design of the NGS Facility.

The initial design of the new neutrino facility (NGS-98) was fixed beginning of 1998 but necessary technical changes in the beam optics alignment required a completely new shielding layout (NGS-99). One essential consideration in the design of the NGS facility was the desire to maintain the flexibility to accommodate a variety of neutrino beam configurations. This flexibility includes designing the target hall in which the location of the beam components, such as the target and the focusing horns may vary depending on the desired range of neutrino energy. Maintaining this flexibility has also an impact on the layout of the radiation shield because of the desire to minimize the reconfiguration of the target hall shielding after the facility started operation. Nevertheless, inherent in the design is the fact that most serious difficulties arise in the target area due to very high intensity beams foreseen. Radiation protection is of greatest importance in both, primary and secondary beam areas and, therefore, these areas must be provided with sufficient shielding to protect the adjacent environment.

2. Determination of Radiological Parameters.

The choice of this aspect arose from the lack of radiological parameters for NGS-98, as well as, NGS-99. Therefore, a complete assessment which involved the estimation of the quantities and concentrations of radioactivity which will be produced in the rock, groundwater, concrete and air in and around the installation was essential. The baseline design of the NGS shielding is based on the use of the Monte-Carlo cascade program FLUKA. The output of the Monte-Carlo calculations are subsequently converted to activations or dose equivalents or are used to determine the probability of radionuclide production in the different materials. The induced activities can then be compared to the various limits for each type of radiation exposure.

Finally, this thesis involves experimental work in re-measuring the cross-sections for the production of radioactivity in the molasse rock around the installation. The existing cross sections were based on old data taken from rock close to the CERN-PS and it was useful for the NGS project to have data of the actual molasse at the correct depths. It should be

emphasized that the study of this data is not only of interest for the NGS project but also for the LHC (Large Hadron Collider) and other future projects at CERN.

The thesis is organized as follows. Chapter 2 gives an outline of the physical background of the NGS project at CERN. The first part of this chapter covers the basic information concerning neutrinos and neutrino oscillations and the second part gives an overview of the Monte-Carlo particle transport code FLUKA. Furthermore, it contains a general survey of long baseline neutrino facilities in combination with its beam requirements. The second part, in particular, describes the facilities at CERN, namely the West Area Neutrino Facility and the Neutrino Beam to Gran Sasso.

The experiment which determines the amount of radioactivity, produced in the molasse rock, is subject of Chapter 3. In addition, this experiment was also simulated with FLUKA, and both, the results from the real measurements, as well as, those from the simulations are discussed and compared.

Chapter 4 details the new developments concerning the NGS facility, which has always been scrutinized and improved, and, finally, provides an updated layout of the NGS-99 facility. The purpose of this chapter is to explain the various simulations of the hadron fluence, based on FLUKA, which guided the design of the radiation protection systems in the project.

Chapter 5 defines the estimates of the radiological parameters of concern for the environment, as well as, maintenance work, according to NGS-98 and NGS-99. This includes detailed calculations and analysis of the induced radioactivity in the rock, concrete, air, ground- and cooling water, and different shielding materials used in the facility.

Finally, in Chapter 6 results are summarized.

Chapter 2

Physics and Design Background

This chapter provides a short description of the discovery of the neutrino and of the quantum-mechanical phenomena of neutrino oscillation. Furthermore, this chapter outlines the present evidence of neutrino oscillation and explains different experiments with steadily improving precision, in particular, the NGS-project at CERN.

2.1 Neutrino and Neutrino Oscillation

2.1.1 The Discovery of the Neutrino

Neutrinos, elementary particles of unknown nature, have always been a source of fascination ever since the Austrian physicist Wolfgang Pauli predicted their existence in 1930. He postulated the neutrino as a possibility to save the laws of energy and momentum conservation in explaining observations of nuclear beta decay which is a natural form of radioactivity wherein a parent nucleus decays to a daughter with the same atomic mass, but an atomic number changed by one unit, with the missing charge carried off by an electron or positron

$$(A,Z) \rightarrow (A,Z \pm 1) + e^{\mp}. \qquad (2.1)$$

The decay of a free neutron into a proton and an electron, with a half-life of about 15 minutes is one well-known example. But, contrary to all expectations, a continuous spectrum of electron decay energies was observed which varied over a large energy range. Pauli proposed an unobserved, not detectable, neutral particle as being emitted together with the electron, sharing the available energy. In 1934 Enrico Fermi incorporated these particles in his famous theory of beta decay. The weak interaction of neutrinos with matter was the reason that the first neutrino could not be observed before 1956. Fred Reines and Clyde Cowan Jr. were the first who observed the direct detection of the anti-neutrino through the inverse β^+ decay

$$p + \overline{\nu}_e \rightarrow n + e^+. \qquad (2.2)$$

Their experiment was carried out at the Savannah River reactor in South Carolina, which provided a flux of 10^{13} anti-neutrinos per cm^2 [Cow56]. Their detector contained 200 liters of water in two tanks with up to 40 kg of dissolved $CdCl_2$. The positron produced was detected by its slowing down and annihilating with an electron producing two 0.511 MeV gamma rays in opposite direction. The pair of gamma rays was detected in time coincidence in liquid scintillators above and below the water by photomultiplier tubes. In addition, the neutron was captured by cadmium microseconds after the positron capture. As a result, several gamma rays were emitted which were also detected in the scintillator. Furthermore, there was no evidence for an inverse beta$^-$ decay

$$n + \nu_e \rightarrow p + e^- , \tag{2.3}$$

which would have been an indication for the same nature of the neutrino and the anti neutrino.

The idea that neutrinos come in different flavors became accepted in 1962, when Leon Lederman, Melvin Schwartz, Jack Steinberger and collaborators demonstrated in an experiment at the Brookhaven National Laboratory the evidence of a neutrino from pion decay at a target and discovered that almost all events had a muon, but not an electron, emerging from the point of the neutrino interaction.

In 1975 the third kind of neutrinos was found at the Stanford Linear Accelerator Center, in proposing that the missing energy and momentum in a τ decay is "carried away" by the τ neutrino. From a more recent experiment at the Large Electron Positron Collider (LEP) at CERN, which counted the number of neutrino types in decays of neutral weak boson Z^0, we know that there are exactly three neutrino species, a result that had been predicted by cosmologists.

2.2.2 Neutrino Oscillation

The fundamental question of whether neutrinos have mass has been unanswered for decades. In 1968, the pioneer chlorine radiochemical experiment by Davis and collaborators [Dav94] at the Homestake mine in South Dakota, saw less electron neutrinos than predicted by solar models. The method consisted in measuring the production rate of ^{37}Ar from the capture reaction

$$\nu_e + {}^{37}Cl \rightarrow e^- + {}^{37}Ar \tag{2.4}$$

which occurred in a 390 m^3 tank filled with 615 t of perchlorethylene (C_2Cl_4). The ratio of the measured value to the theoretical prediction was 0.4 [Lel]. The effect of this 30 year old 'solar neutrino problem' could result from the possible transformation of electron neutrinos into neutrinos of another type, not detectable by the experiment. This transformation may occur accordingly to the quantum-mechanical phenomenon of neutrino oscillation which is a consequence of the hypothesis of neutrino mixing. This idea was proposed by the Russian physicist Bruno Pontecorvo [Pon58] and independently by Maki et al. [Mak62]. The concept

of neutrino oscillation was originally introduced for the process $\nu_e \leftrightarrow \overline{\nu}_e$ but after the discovery of ν_μ it was adapted to transitions between different neutrino flavours. To observe neutrino oscillation two conditions have to be fulfilled

- Neutrinos which have mass
- violation of lepton flavour number.

The most straightforward way to introduce these conditions is to assume that the three known neutrino flavours, ν_e, ν_μ, and ν_τ, are not mass eigenstates but quantum-mechanical superpositions of three mass eigenstates, ν_1, ν_2, and ν_3 with mass eigenvalues m_1, m_2, and m_3, respectively. More generally, the linear superposition can be written

$$\nu_l = \sum_a U_{la} \nu_a \tag{2.5}$$

where the subscript l would run over the states ν_e, ν_μ, ν_τ etc. and ν_a would stand for the mass eigenstates and U_{la} indicates the unitary mixing matrix.

From the quantum-mechanical point of view, neutrino oscillations are similar to the very-well known oscillation of neutral kaons

$$K^0 \leftrightarrow \overline{K}^0 . \tag{2.6}$$

In addition, this formalism is analogous to the quarksector, where strong and weak eigenstates are not identical and the resultant matrix is described by a unitary mixing matrix.

Kinematic distributions observed in weak decay can be used in order to determine upper limits on the mass of e, μ, and τ neutrinos, see Table 2.1.

From this table, it can be concluded, that $m_3 \gg m_2 \gg m_1$ where m_1, m_2, and m_3 indicate the ν_e, ν_μ, and ν_τ neutrino-mass, respectively. This would result in decoupling of the oscillation phenomena and a two generation mixing model is a good approximation. [Bil98]

Table 2.1: *Direct neutrino mass measurements* [Bar98].

Type of neutrino	Mass limit	Process
ν_e	< 10 eV	$^3H \rightarrow {}^3He + e^- + \overline{\nu}_e$
ν_μ	< 170 keV	$\pi^+ \rightarrow \mu^+ + \nu_\mu$
ν_τ	< 18.2 MeV	$\tau \rightarrow 5\pi(\pi^0) + \nu_\tau$

Hence, the mixing to two neutrinos, for example, the ν_e and ν_μ flavour states are related to the states ν_1 and ν_2 of definite mass m_1 and m_2 by

$$\begin{pmatrix} \nu_e \\ \nu_\mu \end{pmatrix} = \begin{pmatrix} \cos\theta & \sin\theta \\ -\sin\theta & \cos\theta \end{pmatrix} \begin{pmatrix} \nu_1 \\ \nu_2 \end{pmatrix}. \tag{2.7}$$

Suppose one creates a neutrino beam at $t = 0$, described by the state

$$\begin{aligned} |\nu(0)\rangle = |\nu_\alpha\rangle &= \cos\alpha\,|\nu_e\rangle + \sin\alpha\,|\nu_\mu\rangle \\ &= \cos(\theta+\alpha)\,|\nu_1\rangle + \sin(\theta+\alpha)\,|\nu_2\rangle. \end{aligned} \tag{2.8}$$

After a time t, the state would evolve to

$$|\nu(t)\rangle = e^{-iHt}\,|\nu_\alpha\rangle = e^{-iE_1 t}\cos(\theta+\alpha)\,|\nu_1\rangle + e^{-iE_2 t}\sin(\theta+\alpha)\,|\nu_2\rangle. \tag{2.9}$$

In realistic neutrino oscillation experiments the neutrino masses are probed in the sub keV regions whereas experimentally accessible neutrino momenta are in the MeV and GeV range. Therefore, a simplifying assumption of ultra-relativistic neutrinos is valid and can be expressed by

$$E_i = \sqrt{p^2 + m_i^2} \approx p + \frac{m_i^2}{2p}. \tag{2.10}$$

Hence, equation (2.9) becomes

$$|\nu(t)\rangle = e^{-iE_1 t}\,[\cos(\theta+\alpha)\,|\nu_1\rangle + e^{-i\Delta E t}\sin(\theta+\alpha)\,|\nu_2\rangle]. \tag{2.11}$$

The probability to detect a neutrino state ν_β at time t can then be calculated

$$\left|\left\langle \nu_\beta \middle| \nu(t) \right\rangle\right|^2 = \left|\cos(\theta+\alpha)\cos(\theta+\beta) + e^{-i\Delta Et}\sin(\theta+\alpha)\sin(\theta+\beta)\right|^2$$

$$\frac{1}{2}\left[1+\cos(2\theta+2\alpha)\cos(2\theta+2\beta)+\sin(2\theta+2\alpha)\sin(2\theta+2\beta)\cos\left(\frac{\Delta m^2}{2E}t\right)\right]$$

$$\frac{1}{2}\left[1+\cos(2\alpha-2\beta)\right]-\sin(2\theta+2\alpha)\sin(2\theta+2\beta)\cos\left(\frac{\Delta m^2}{4p}t\right). \qquad (2.12)$$

In particular, if we consider $\alpha=\beta$ which would mean that we try to find the same state that was created at $t = 0$, we obtain the survival probability of that state

$$P_{surv} = 1-\sin^2(2\theta+2\alpha)\sin^2\left(\frac{\Delta m^2}{4p}t\right). \qquad (2.13)$$

On the other hand, if $\left|\nu_\beta\right\rangle$ is orthogonal to the original state $\left|\nu_\alpha\right\rangle$ we obtain the conversion probability, which is

$$P_{conv} = \sin^2(2\theta+2\alpha)\sin^2\left(\frac{\Delta m^2}{4p}t\right). \qquad (2.14)$$

If we furthermore consider only the pure flavour states, i.e., ν_e or ν_μ for the initial and the final state, α is either 0 or $\pi/2$. In both cases, we obtain

$$P_{surv} = 1-\sin^2(2\theta)\sin^2\left(\frac{\Delta m^2}{4p}t\right), \qquad (2.15)$$

and

$$P_{conv} = \sin^2(2\theta)\sin^2\left(\frac{\Delta m^2}{4p}t\right). \qquad (2.16)$$

In more familiar units we can then describe the probability that one neutrino transforms into another in an neutrino oscillation experiment by

$$P_{conv} = \sin^2(2\theta)\sin^2\left(1.27\frac{\Delta m^2 L}{E}\right), \tag{2.17}$$

where $\sin^2(2\theta)$ is the, so called, mixing angle, Δm^2 is the difference in mass squares of the two neutrinos, $L=ct$ is the distance in m (in km) from the neutrino production point to the experiment, and E is the neutrino energy in MeV (in GeV). If either $\sin^2(2\theta)=0$ or $\Delta m^2=0$, the phenomenon of neutrino oscillations does not exist.

As a result of equation (2.17) the neutrino "oscillates" with a strength $\sin^2(2\theta)$ and an "oscillation length"

$$\lambda_{osc} = \frac{\pi E_\nu}{1.27\Delta m^2} = 2.48\frac{E_\nu}{\Delta m^2}. \tag{2.18}$$

Therefore, the oscillation probability varies as

$$\sin^2\left(\frac{\pi L}{\lambda_{osc}}\right) \tag{2.19}$$

and depends on the parameter L/E. Figure 2.1 shows the oscillation probability, as a function of L/E for the case of $\Delta m^2 = 0.001$ eV^2. From equation (2.17), one can conclude that three important issues confront a neutrino oscillation experiment. First, if searching for oscillations in very small Δm^2 regions L/E must be large in order to enhance the $\sin^2(1.27\Delta m^2 L/E)$ term. On the other hand L/E should not be too large in comparison to Δm^2 because then oscillation would occur rapidly. The minimum Δm^2 to which the experiment is sensitive (for full mixing, i.e., $\sin^2(2\theta)=1$) is

$$\Delta m^2(\mathrm{eV}^2) = \frac{\sqrt{P}\,E(\mathrm{GeV})}{1.27\,L(\mathrm{km})}. \tag{2.20}$$

Second, if Δm^2 is very large the oscillation probability will no longer depend on L and the transition probability will average to ½ $\sin^2(2\theta)$. Finally, in the case that the mixing angle is too small, high statistics would be required in order to get an oscillation signal.

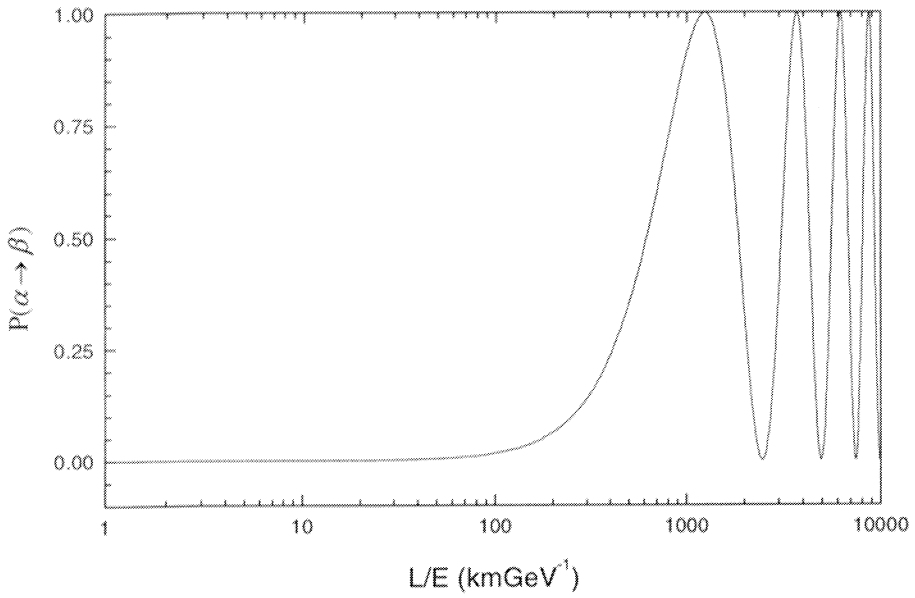

Figure 2.1: *Oscillation probability for the case of a LBL experiment.*

Therefore, each oscillation experiment is characterized by the following parameters:

- the neutrino energy E,
- the mean distance L between the source of the neutrino and the detector,
- the width of the L/E distribution,
- the minimal transition probability P_{min} between two different weak eigenstates.

Based on equation (2.20) and on a typical accelerator neutrino energy of 10 GeV, a short-base line (SBL) experiment can be defined as followed: the distance between the target and the detector (L) is about 1km which implies a Δm^2 sensitivity of approximately 1 to 10 eV^2 whereas for a long-baseline (LBL) experiment the distance is about 1000 km with a Δm^2 sensitivity of 10^{-2} to 10^{-3}.

Results of neutrino oscillation experiments are normally presented in a two-parameter space of $\sin^2(2\theta)$ and Δm^2, see Figure 2.2. In the case that no neutrino oscillation signal is observed the parameter region on the right hand side of the curve would be excluded. Observation of no oscillation signals would instead result in a preferred parameter region within a band along this curve.

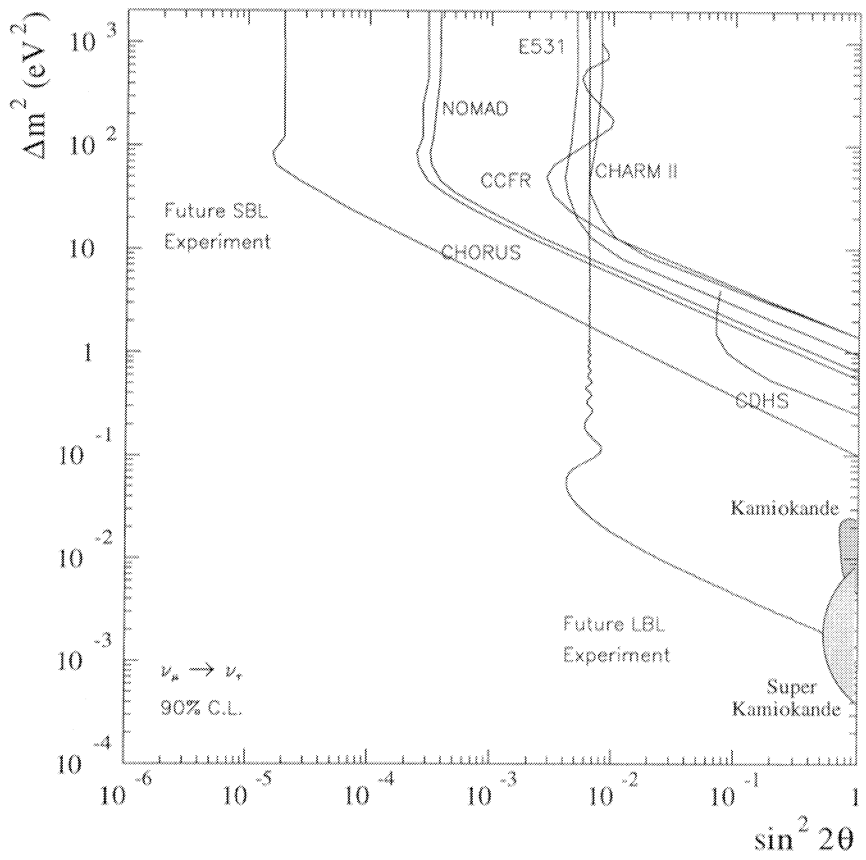

Figure 2.2: *Oscillation parameter range to be covered by future SBL and LBL $\nu_\mu - \nu_\tau$ experiments.* [NGS98]

Neutrino oscillation experiments can be subdivided into disappearance and appearance searches. In an experiment of the first type the main requirement is to have a beam with a very well known intensity. The flux of the main beam component (ν_μ in the case of the NGS) is measured at a given distance L from the source. The occurrence of neutrino oscillation is given, when the number of detected neutrino events is less than the expected number with no oscillation.

The sensitivity of disappearance experiments is limited by systematic uncertainties on the knowledge of the neutrino beam intensity. For this reason, the measurement of the flux can profit from another detector placed at a position which is closer to the target. This detector is normally called the 'near detector'.

On the contrary, in an appearance experiment the neutrino beam should consist of one neutrino flavour and should search for the 'appearance' of another flavour, which in principle is absent in the beam. The sensitivity of these experiments is obviously limited by the uncertainty in the contamination of the other neutrino flavour in the beam. In the case of the NGS the most interesting appearance search is for $\nu_\mu - \nu_\tau$ oscillation. The ν_τ contamination of the beam is at a very low level, which allows high sensitivity explorations.

It is further important to note that since the appearance of a different neutrino flavour is detected through the interaction of this neutrino with the experimental target, the neutrino

must be energetic enough to produce its corresponding charged lepton. In particular, since the threshold to produce a τ lepton is ~ 3.5 GeV [NGS98], a high-energy beam is preferred for the experiment.

2.2 Evidence of Neutrino Oscillation

Presently, there are three experimental indications for neutrino oscillation:

- *Solar Neutrino Deficit:* Five different (Homestake [Cle98], Kamiokande [Hir96], GALLEX [Ham96], SAGE [Abd96] and Super-Kamiokande [Fuk98a]) experiments observed event rates which were significantly smaller than predicted from the Standard Solar Model (SSM) [Bah98].
- *Atmospheric Neutrino Deficit:* It refers to neutrinos produced by decays of mesons from cosmic ray interactions in the atmosphere. Impressive evidence in favour of oscillation of atmospheric neutrinos was recently obtained in the Super-Kamiokande experiment [Fuk98b]. Indications of neutrino oscillations were reported from the Kamiokande [Fuk98c], IMB [Bec95], Soudan 2 [All97] and Macro [Amb98] atmospheric experiments.
- *LSND experiment:* In this experiment, neutrinos were produced in decays of π^+ and μ^+ at rest and, thus, there were no $\overline{\nu}_e$'s from the source. But a significant number of $\overline{\nu}_e$ was found at a distance of about 30 m away from the source [Ath96].

2.3 Long Baseline Neutrino Facilities

K2K in Japan:

The Japanese neutrino project KEK-to Kamiokande started operating in 1999. In this experiment a neutrino beam is sent from the Japanese laboratory of high-energy accelerator research (KEK) to the Super-Kamiokande detector 250 km away. In June 1999 the first neutrino event produced by the 12 GeV proton synchrotron in KEK was observed in the Super-Kamiokande detector. This was the first time that a particle, produced artificially, was detected after traversing 250 km of earth. The facility consists of the 12 GeV proton synchrotron which hits a beryllium target and produces a neutrino beam of an average energy of 1 GeV. A front detector about 300 m away from the target serves as reference and measures the neutrino spectrum. Then by comparing neutrinos observed in both detectors, one can try to examine neutrino oscillations. An upgrade of KEK to a 50 GeV proton beam is planned, which could start producing data around 2004 and would also allow ν_τ appearance searches. Note that at the moment only disappearance experiments can be performed.

The NUMI Project in the United States:

A big neutrino program, Neutrinos at the Main injector (NUMI), is associated with the new main injector at Fermilab. This facility, approved in 1998, will use protons of 120 GeV to produce a neutrino beam which will be sent to the Soudan mine about 735 km away from Fermilab. The long-baseline experiment MINOS will consist of two detectors, a near

detector situated about 1.3 km from the target and a far detector at 735 km. The neutrino beam will be a wide-band beam with an average ν_μ beam energy of 17.6 GeV. Several muon detectors will be placed in a number of pits constructed in the dolomite downstream of the hadron stopper.

The target chamber and the decay tunnel of the NUMI facility will be located in dolomite bedrock, which is a class one groundwater aquifer. This requires particular concern in the design of the shielding, which must be adequate to meet standards applicable to potential sources of potable water. Therefore, massive modular shielding, of steel, concrete and marble, is foreseen around the beam line.

During the first years of operation only disappearance searches are planned but due to the high energy of the neutrino beam also $\nu_\mu \rightarrow \nu_\tau$ appearance experiments will be possible in the future.

The CERN Neutrino Beam to Gran Sasso (NGS) Project:

This project, which is described in section 2.5.2, will produce a neutrino beam at CERN for neutrino oscillation searches at the Gran Sasso Laboratory in Italy. Several experiments were proposed, the first, is the ICARUS [Rub95] experiment and the SUPER-I(carus) [ICA98] proposal whereas the first one will anyway be installed in Gran Sasso for the search of proton decay and solar neutrinos. A second proposal is a 27 kt water-RICH detector (AQUA-RICH) [Yps96] which could be installed either inside or outside the Gran Sasso tunnel. The NOE [Amb95] experiment plans to build a giant lead-scintillating fibre detector with a total mass of 4kts which will consist of 4 modules followed by a module for muon identification. Finally, there exists a proposal for an iron emulsion sandwich detector (OPERA) [OPE98] and the NICE proposal [NIC98].

2.4 Beam Requirements

The Super-Kamiokande Collaboration reported evidence of observing muon neutrino oscillations at full mixing with a mass difference squared between 10^{-3} and 10^{-2} eV^2 [Fuk98b]. Many scenarios with three neutrino oscillations are possible, as long as there is little electron neutrino mixing in the appropriate range of L/E. Simple two neutrino oscillations fit the data, with the oscillating partner being either the tau neutrino, ν_τ, or a new sterile neutrino $\nu_{sterile}$.

In general, the rate of ν_τ-charged current (CC) events from a ν_μ beam is given by

$$R_\tau = A \int \Phi_{\nu_\mu}(E) \times P_{osc}(E) \times \sigma_\tau(E) \times \epsilon(E) \times dE, \qquad (2.21)$$

where A is the number of nucleons in the effective detector mass, $\Phi_{\nu_\mu}(E)$ is the ν_μ fluence at Gran Sasso, $\epsilon(E)$ represents the (detector dependent) detection efficiency of the ν_τ-events, $\sigma_\tau(E)$ is the ν_τ CC cross-section and P_{osc} is the oscillation probability. For two flavour mixing, see equation (2.17) and neglecting the detection efficiency, the neutrino spectrum $\Phi_{\nu_\mu}(E)$ should match the product $P_{osc} \times \sigma_\tau(E)$. For the NGS project, optimizing the

probability for ν_τ appearance at Gran Sasso implies maximizing the ν_μ fluence in the range of 10 to 30 GeV and, therefore, two magnetic lenses, see the following section, are designed to focus 35 GeV and 50 GeV secondary particles, respectively.

2.5 The CERN Neutrino Programs

Neutrino physics started at CERN in 1963 using particles from the proton synchrotron (PS). This PS neutrino program continued until 1977 and the highlight was the discovery of the weak neutral current in 1973. Plans for a new neutrino program were proposed in 1971 during the planning of the Super-Proton-Synchrotron (SPS) project. It was decided to build a new facility on the west area of CERN.

2.5.1 The West Area Neutrino Facility

The West Area Neutrino Facility (WANF) continued operation with only minor interruptions concerning changes in beam configurations from 1976 to the end of 1998. For many years, the facility provided the worldwide most powerful beam of high-energy muon neutrinos ν_μ to the particle physics community.

Initial physics centered on studies of neutral currents, on the quark structure of matter, and on quantum chromodynamics (QCD), the field theory of quarks and gluons. The results obtained were, and still are, important input for tests of the Standard Model.

A schematic layout of the present WANF is shown in Figure 2.3. Protons extracted from the SPS at 450 GeV are directed towards the West Experimental Area and are focused onto a beryllium target (T9).

Pions and kaons produced in the target are focused towards the detectors in an approximately parallel beam by two co-axial magnetic lenses, more familiarly known as horn and reflector. These pions and kaons decay in flight to produce muons and muon neutrinos. The muons and remaining hadrons are stopped in a long iron and earth shield at the end of the decay path leaving only the neutrinos to continue to the detectors 800 m from T9. In the WANF, the distance from the target to the beginning of the iron shield was about 420 m. To minimize the number of 'parent' particles which interact in the air before their decay, the spaces between the focusing devices in the 120 m long cavern have large diameter tubes filled with helium at atmospheric pressure. The final 300 m long decay tunnel is evacuated to 0.5 Torr.

Measuring the muon flux distributions at a number of monitoring gaps in the iron shielding provided an invaluable diagnostic tool to understand the neutrino flux and to align the beam.

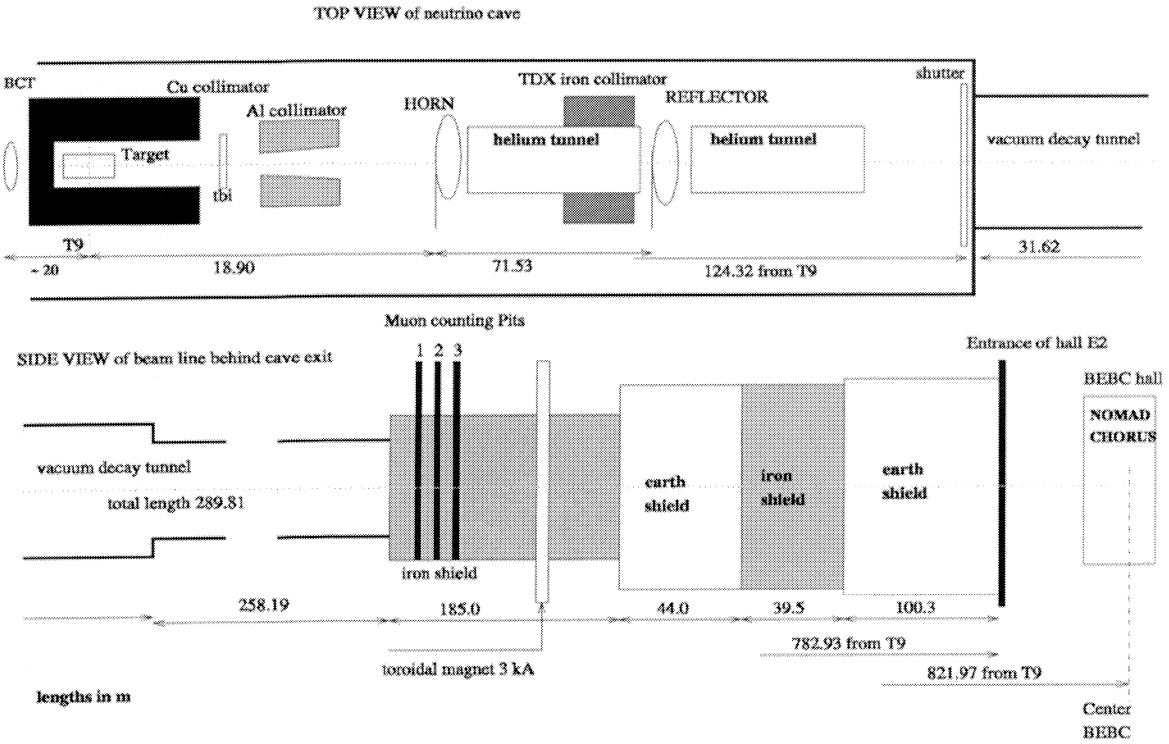

Figure 2.3: *Schematic layout of the CERN West Area Neutrino facility (WANF).*

The last major upgrade of the WANF took place in 1992/1993 in preparation for the CHORUS and NOMAD experiments which approached the end of their data taking in September 1998. These experiments aimed at detecting evidence of non-zero neutrino mass, searching for neutrino oscillation, from ν_μ to ν_τ. The nearly pure wide-band ν_μ neutrino beam with an average energy of 27 GeV had a contamination of muon antineutrinos of a few percent and about 1% contamination of electron neutrinos.

2.5.2 The NGS-Facility

For the detection of neutrino oscillations, the CERN Super Proton Synchrotron (SPS) accelerator facility in combination with the detectors at the Gran Sasso National Laboratory (LNGS - Laboratori Nazionali del Gran Sasso) in Italy, 732 km away from CERN (Figure 2.4) would provide an opportunity for a long-baseline experiment, either by appearance or disappearance measurements.

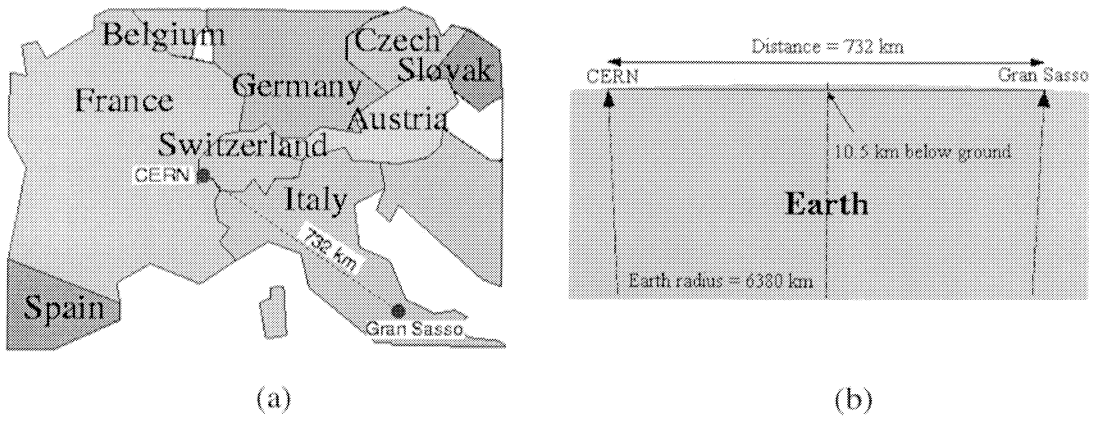

(a) (b)

Figure 2.4: *(a) Geographic configuration of the planned neutrino beam from CERN to Gran Sasso and (b) cross-sectional view of the earth showing the path of the neutrino beam.*

The Gran Sasso National Laboratory was founded by Instituto Nazionale di Fisica Nucleare (INFN) in 1987 as an institution for cosmic ray and rare decay studies. It is located alongside the Gran Sasso tunnel about 6 km away from the west entrance. The laboratory is situated 963 m over the sea level and the maximum thickness of the rock overburden is 1400 m, corresponding to 3800 m water equivalent. Furthermore, the LNGS is a perfect place for highly sensitive experiments which will allow both, neutrino appearance and disappearance measurements because only neutrinos and high-energy muons, among the known particles, can penetrate such a layer of rock.

The following paragraphs, in particular, give a short account on the different constituents of the facility. The proton beam with an energy up to 450 GeV (400 GeV nominal) can be extracted from the CERN SPS and can be brought onto an axis towards Gran Sasso through a 800 m long transfer line with a final downwards slope of 5.6%. The layout of the NGS at CERN in a plan view is given in Figure 2.5 and a cross sectional view in Figure 2.6.

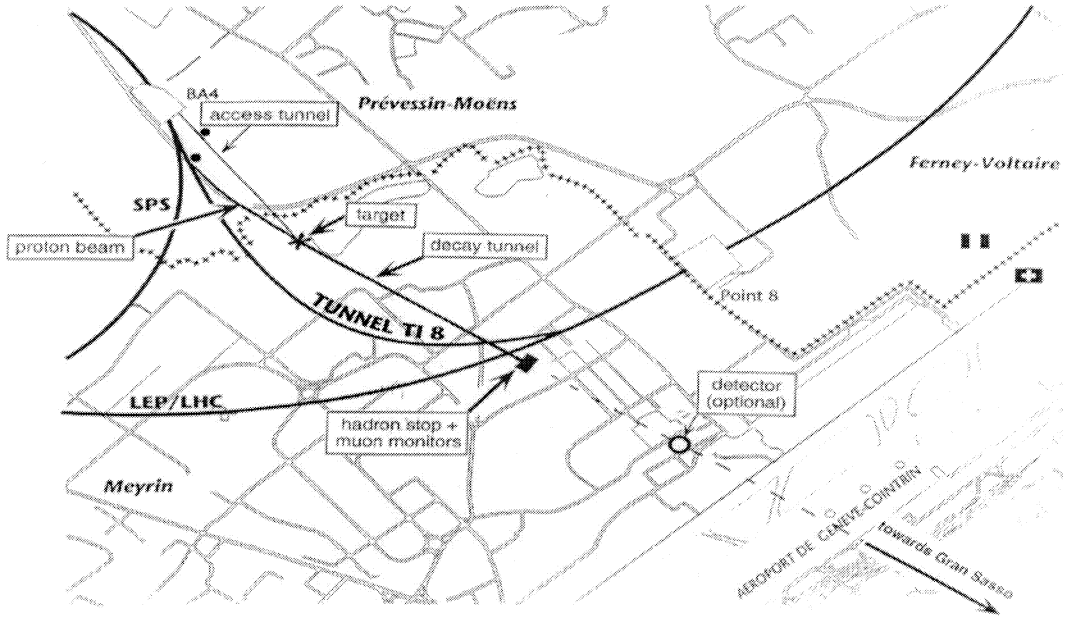

Figure 2.5: *Layout of the NGS at and around CERN.*

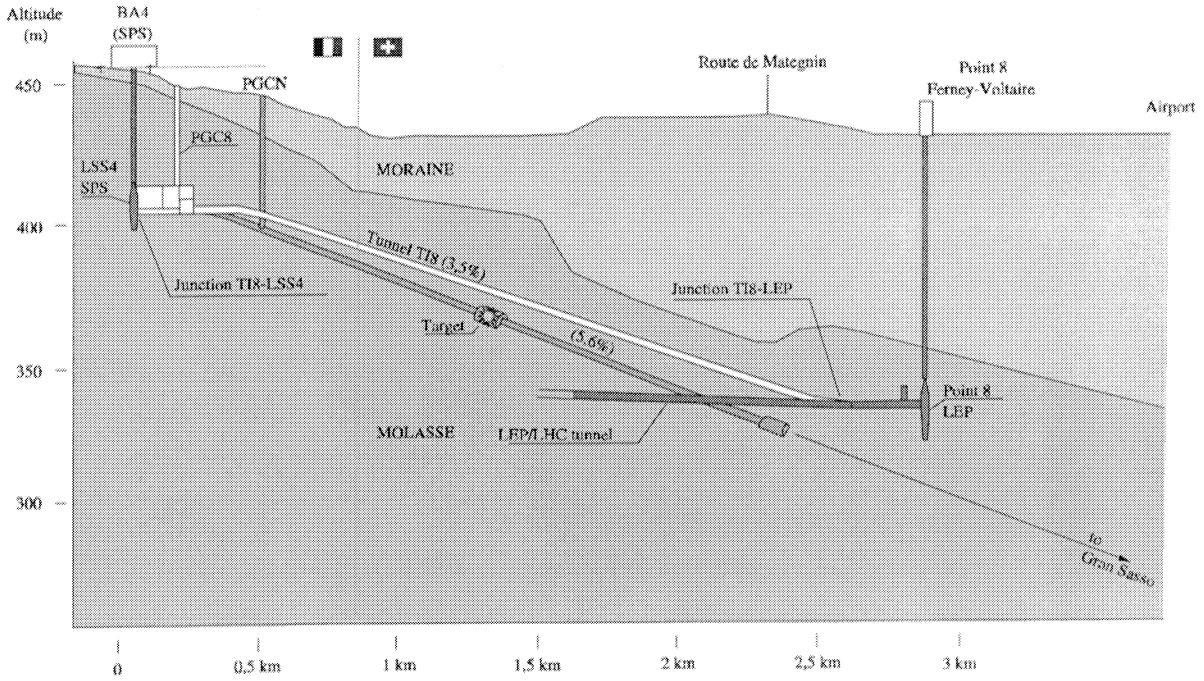

Figure 2.6: *Cross-sectional view of the SPS and the main components of the NGS.*

After focusing the proton beam to a 2mm beam spot, the protons hit a segmented helium cooled graphite target which is located in a cavern approximately 60 m below the surface. The pions and kaons produced from the target in a desired energy range will then be focused into a parallel beam pointing towards Gran Sasso by two coaxial magnetic lenses. In order to reduce the interaction of pions and kaons with air particles two helium tubes will be installed

in the cavern as the nuclear interaction length is 3300 m for helium and only 700 m for air. One tube will be located between the horn and the reflector the other one between the reflector and the end of the target cavern.

The neutrino beam is generated from the decay of these mesons in the following way

$$\pi^+ \rightarrow \mu^+ + \nu_\mu \qquad \pi^- \rightarrow \mu^- + \bar{\nu}_\mu$$

$$K^+ \rightarrow \mu^+ + \nu_\mu \qquad K^- \rightarrow \mu^- + \bar{\nu}_\mu .$$

It is mentioned in [NGS98] that the ratio of π to K produced in the target is roughly 10:1 and that the maximum energy of ν_μ from π decay is approximately 43 % of the parent π energy. Furthermore, the two-body decay of K gives ν_μ up to 96% of the parent energy. This leads to two superimposed parts of the overall neutrino spectrum dominated by a π-generated component at lower energies and a smaller K component at higher energies. In order to obtain a neutrino beam towards Gran Sasso, the parent hadrons have to decay in flight while travelling in that direction. The mean free path of π before decay is 56 m/GeV and for K it is 7.5 m/GeV. To avoid an interaction before they can decay, an evacuated decay path is essential. The typical π decay length at 40 GeV is 2.2 km, which implies that a long decay pipe is desirable. For the NGS, a pipe of 2.45 m diameter and 1000 m length was chosen. All muons and remaining hadrons are absorbed by a massive array of graphite (length 3 m) followed by iron blocks (length 15 m) at the end of the decay tunnel. This hadron stopper is water cooled in order to remove the energy deposited by the beam. The planned target chamber and the surrounding facilities are shown in Figure 2.7.

The target cavern itself has a diameter of 6.5 m which is widened on the side near the target to a diameter of 8.5 m over a length of 15 m. This enlargement will allow the installation of a crane with a capacity of 10 t over its entire length. Upstream of the tunnel junction alongside the proton beam tunnel is a storage chamber, 20 m long and 3.1 m in diameter and a ventilation cavern which is 15 m long and 9 m in diameter. The ventilation chamber is used for the installation of the ventilation and the cooling equipment, which is installed on a 2.7 m high platform providing a passage beneath it. Parallel to the target chamber is a service gallery with a total length of 148 m and 3.4 m in diameter. This gallery will allow protection for personnel access and house delicate equipment. Furthermore, the target chamber and the gallery are interconnected by transverse tunnels providing access for people and supply connections. The draining water from the structures, as well as, water from the cooling circuit is taken by a sump of 30 m^3 which is located at the end of the service gallery.

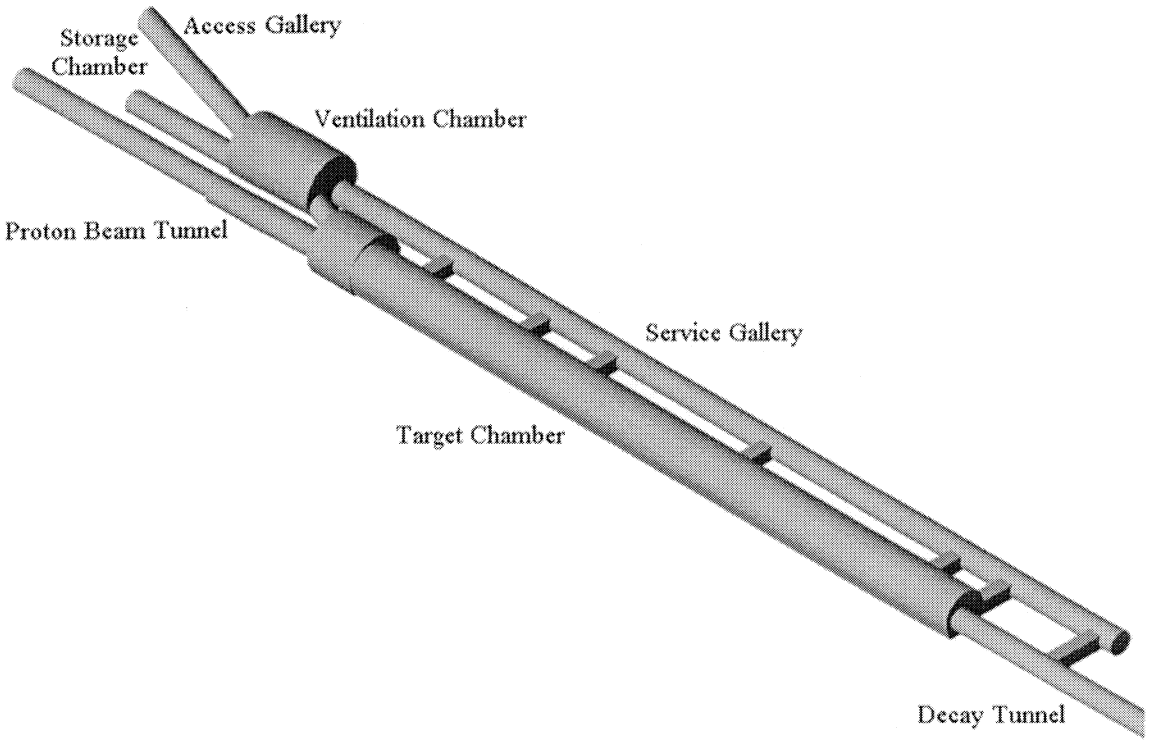

Figure 2.7: *Target chamber and surrounding facilities of the NGS.*

It turned out to be reasonable to consider an optional short base-line neutrino oscillation experiment which could be built at a distance of about 1850 m away from the NGS target, and 150 m underground just north of the Geneva airport, see Figure 2.5. More information about this possible, new experimental area can be found in [Aya97].

Taking the SPS limitations, the NGS target constraints, the impact from the Large Hadron Collider (LHC), as well as, the requests for slow-extracted (SE) beam for the fixed-target physics community and test beam users into account, the expected number of protons on the NGS target (pot) is 4.5×10^{19} pot/year, assuming 200 days of operation per year. In order to provide an idea of the reduction in performance by sharing protons with LHC and with other fixed-target users, the previous number is compared to the performance in dedicated operation, which would provide 7.6×10^{19} pot/year. This indicates a significant but unavoidable loss of 40 % due to sharing. Rate-dependent radiological parameters will be based on an intensity at 400 GeV of 5.0×10^{12} protons on target per second over a period of 200 days of operation per year, and that for the accumulated radioactivity 5.0×10^{19} protons on target per year should be assumed. The lifetime of the facility is taken to be 10 years.

The following paragraphs give a description of the NGS-98 layout which was employed in the FLUKA calculations. A general layout of the target chamber with the beam and shielding elements is given in Figure 2.8. Note that for all elements the z-origin is the nominal focal point of the proton beam, which is 50 cm downstream from the start of the first target rod.

Target Station:

A sectional view of the design of the target station is shown in Figure 2.9. The target area is particularly denoted by a rather high radioactivity due to very high intensity beams. The lateral shielding of the target is 60 cm of cast iron surrounded by 40 cm of marble. The target consists of 11 cylindrical graphite rods (density 1.81 g/cm^3) of 10 cm length. Segmenting the target avoids the development of thermal shock waves which could cause fracture and, furthermore, enhances target cooling. Using material with a low density improves the low energy secondary production by reducing absorption and scattering in the target material. In order to minimize the interaction of secondaries produced at large angles the diameter of the target is required not to exceed the proton beam size. Therefore, a target diameter of 3 mm is chosen which further allows small beam instabilities and possible scattering in the target material. The individual rods are separated longitudinally by gaps of 9 cm, giving an overall target length of 2 m. The space inside the target box surrounding the target is filled with gaseous helium which provides an effective cooling and in addition an excellent protection of the graphite rods from oxidation.

The first downstream collimator, COLL.1, made of copper, is foreseen to shield the walls of the target cavern. The second collimator, COLL.2, made of aluminum, should form part of the definition of the pion beam to produce the neutrinos. The iron and the marble shielding around COLL.2 are an option which turned out to be very effective in protecting the walls from radiation. Note that these shieldings were not part of the Reference Design of NGS-98, see Appendix A. The dimensions of the collimators are listed in Table 2.2.

Table 2.2: *Details of collimators close to target.*

COLL.1 - at target exit	
Material	Copper
Start co-ordinate w.r.t. proton focus	+1.70 m
End co-ordinate w.r.t. proton focus	+2.90 m
Outer cross-section	square 1 *times* 1 m^2
Opening	Cylindrical
Radius of opening such that limitation at exit is	± 20 mrad
COLL.2 – before the horn	
Material	Aluminum
Start co-ordinate w.r.t. proton focus	+4.30 m
End co-ordinate w.r.t. proton focus	+7.00 m
Outer cross-section	Cylindrical
Outer diameter	0.5 m
Opening	Conical
Opening angle see from focus is	± 15 mrad

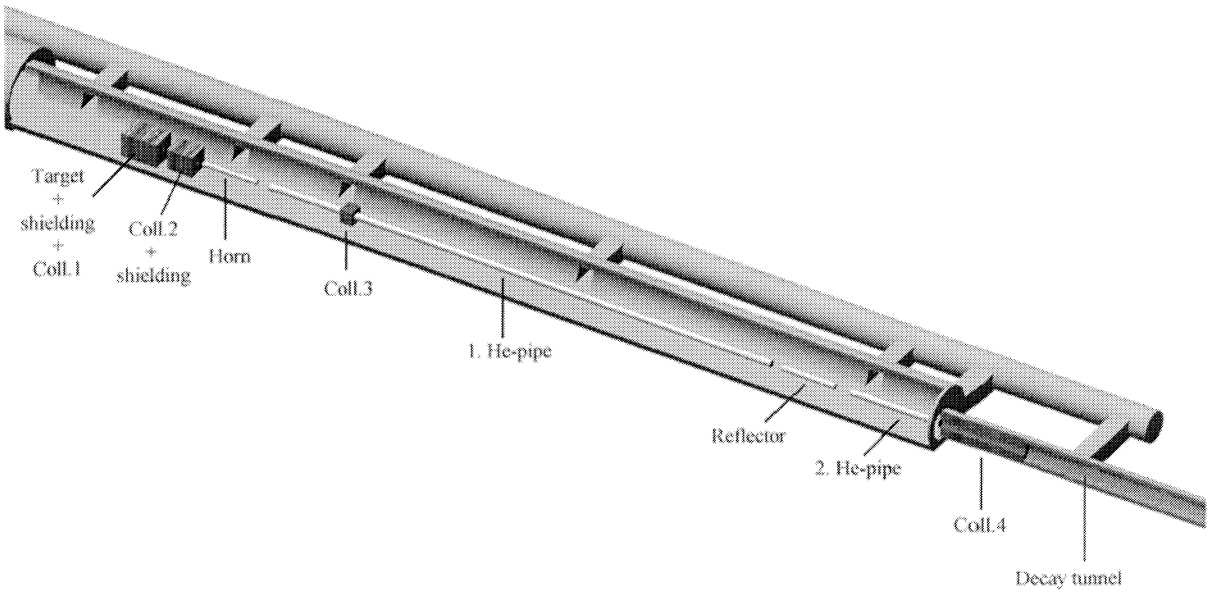

Figure 2.8: *Layout of NGS-98.*

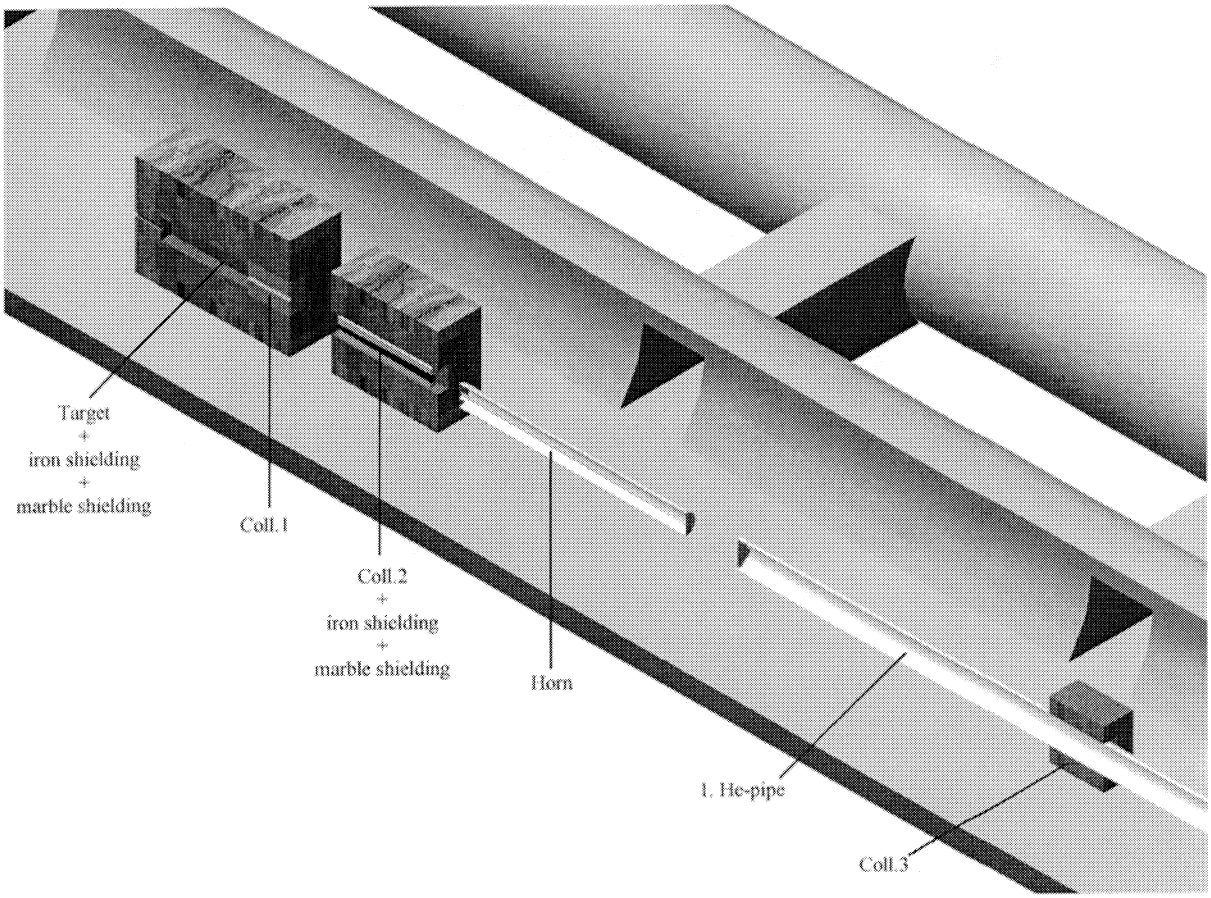

Figure 2.9: *Details of the target and the horn region of NGS-98.*

Focussing Devices:

In order to focus the divergent beam of secondary pions and kaons from the target into a parallel beam, coaxial magnetic lenses are applied as they provide higher angular and momentum acceptance than other focussing systems. In addition, they are sign selective which enable both neutrino and anti-neutrino beams to be produced, and, finally, they are known to be radiation resistant. Moreover, by rearranging the focussing system the neutrino mean energy can vary to a certain extent depending on the position and the shape of the focussing devices. For the NGS a system of two magnetic devices, namely the horn and the reflector is used. Both elements are made of aluminum and their design consists of two symmetric cylinder current sheets, *viz*, the inner and the outer conductor. A sectional view of the horn and the reflector is given in Figure 2.10 and Figure 2.11. Furthermore, both elements have an overall length of 6.65 m. For the horn the thickness of the inner conductor varies from 2 mm at the most open part to 9 mm where the diameter is smallest. In general, the inner conductor is made as thin as possible to minimize absorption of pions and kaons but, nevertheless, must withstand the high current density needed, as well as, the radial forces induced by the strong magnetic field. The thickness of the outer conductor is 12 mm. The horn starts at 7.85 m from the focal point of the proton beam and has an outer diameter of 60 cm. For the reflector the thickness of the inner conductor is 2 mm uniform over its length whereas the thickness of the outer conductor is again 12 mm. Its large central aperture allows to focus particles of different energies which were underfocussed or overfocussed in the horn. Additionally, particles which are well focussed can pass the non magnetic inner part of the reflector without any deflection. The reflector starts at 83.75 m.

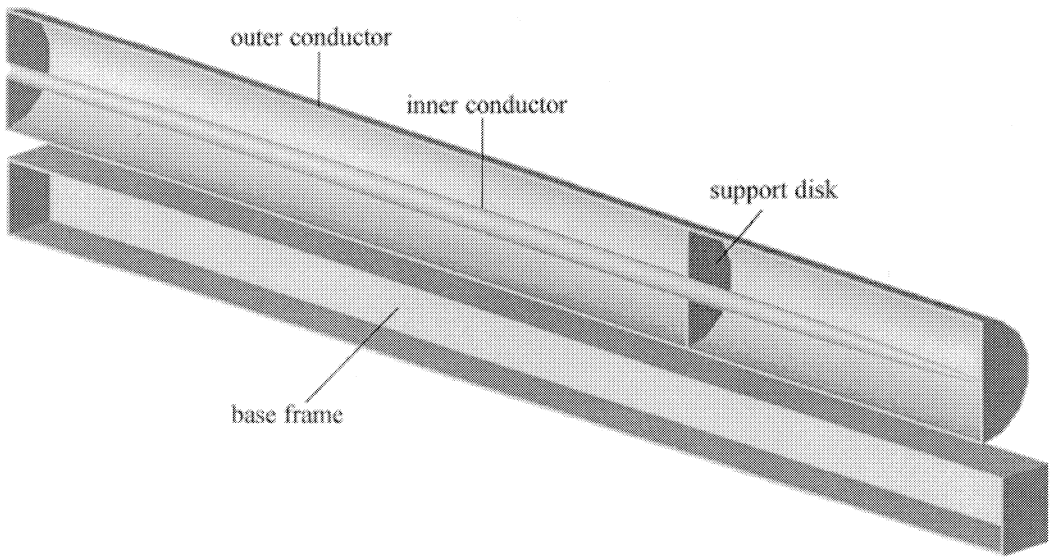

Figure 2.10: *Cross-sectional view of the horn.*

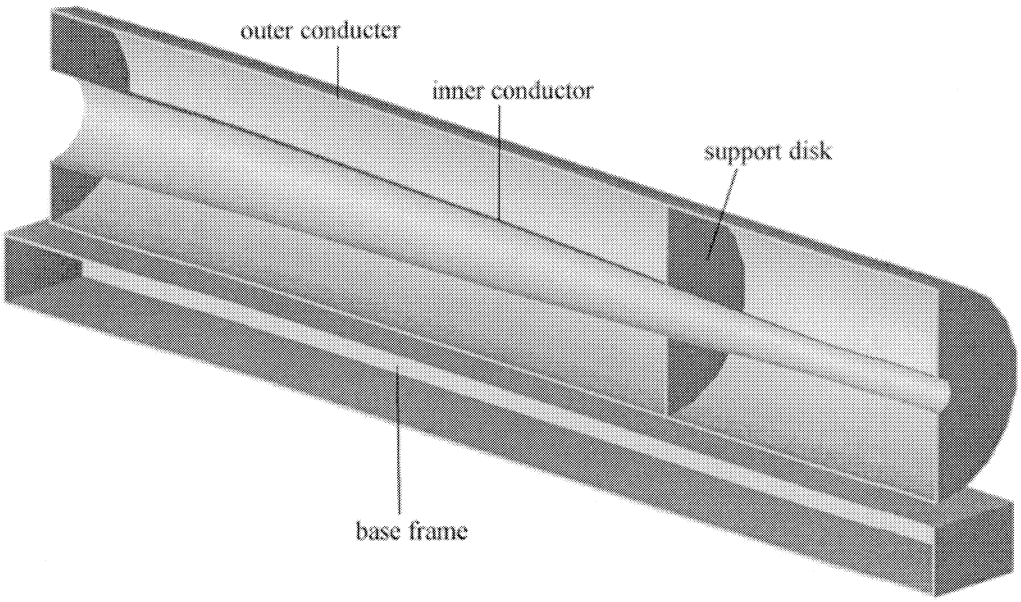

Figure 2.11: *Cross-sectional view of the reflector.*

The magnetic fields of the horn, as well as, of the reflector are produced when high current flows along the inner conductor and back through the outer. The current, 120 kA for both the horn and the reflector, generates a toroidal magnetic field inside the conductors whose strength varies with radius of axis [NGS98] like

$$B[\mathrm{T}] = \frac{0.2 \times I[\mathrm{kA}]}{r[\mathrm{mm}]}. \qquad (2.22)$$

It should be noted that there is no magnetic field either inside the inner conductor or outside the outer conductor. The shape of the horn and the reflector are adjusted to optimally focus π and K of 50 GeV nominal energy for the horn and 85 GeV for the reflector.

In order to avoid unwanted attenuation of the pion flux and production of radioactivity in air, it is desirable to reduce the number of inelastic interactions in air caused by the secondaries and the protons which do not interact in the target. The spaces between the horn and the reflector and between the reflector and the end of the target cave will contain aluminum tubes, 5mm thick, filled with gaseous helium. Both ends of the tanks are closed by a titanium window of 0.3 mm thickness. In the present calculations the bags are considered to be cylindrical with a radius of 40 cm.

In order to avoid high energy pions which are not focused by the horn hitting the walls of the target cavern, and so creating radioactivity in the concrete and molasse rock surrounding the cavern, a steel collimator (COLL.3) is placed around the first helium pipe. Collimator 3 is assumed to be 1.6 m long and of square cross-section with overall dimensions of 170×170 cm^2 and an opening of 80×80 cm^2.

Decay Tunnel:

The decay tunnel basically consists of a steel cylinder 2.45 m (96 inch) in diameter and 992 m in length. The minimum thickness of the walls is limited to 18 mm because of transporting. Inside the tube the pressure will be maintained between 1 and 2 torr. Around the tube, the space between the tube and the shotcrete walls will be filled with concrete to reduce muon background and to avoid the need for ventilation. At the front of the tunnel the diameter will be reduced over the first 10 m of its length by an iron collimator COLL.4 whose inner diameter is 1 m, see Figure 2.8. This will impede access via the entrance-window to the decay tube (thickness 2 mm of titanium). The outer diameter of the collimator is the same as the inner diameter of the shotcrete, namely, 3.1 m. Therefore, a way into the decay tunnel will be given via a side gallery just behind the collimator.

Hadron Stopper:

The hadron stopper is placed after the decay tunnel and is 26 m long and 6 m in diameter. The length of the actual stopper is 18 m and its cross-section is 4×4 m^2. The space between the iron stopper and the walls is filled with concrete. A cross-sectional view of the hadron stopper zone is given in Figure 2.12. In the present design, the proton beam and hadron secondaries which did not decay traverse a steel window (5 cm thick) at the front of the stopper before entering an air chamber (20 cm thick) to provide thermal insulation of the stopper. To reduce the energy density in the first part of the stopper, it is intended to insert a cylinder of graphite, 3 m long and 2.6 m in diameter. A second air chamber is behind the stopper, 2 m long, again for thermal insulation of the dump. This chamber is separated from the muon detector area at the back of the tunnel by a concrete wall.

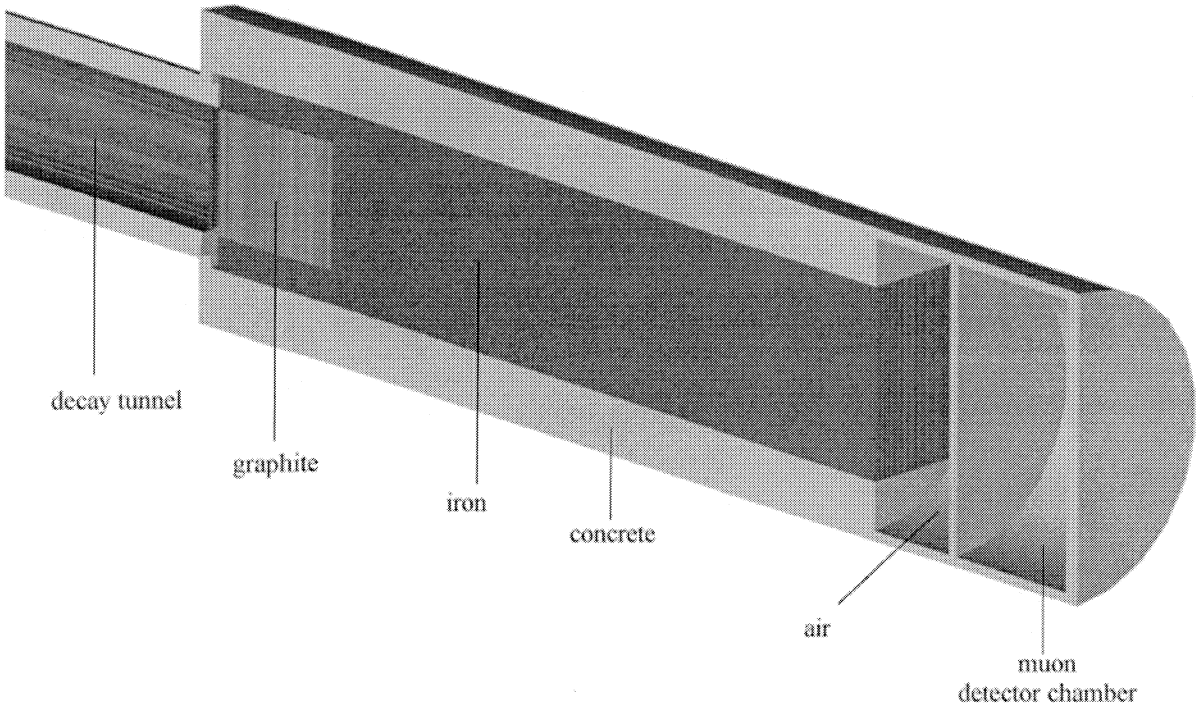

Figure 2.12: Cross-sectional view of the hadron stopper.

2.6 The Monte Carlo Code FLUKA

The development of the particle interaction and transport Monte Carlo (MC) code FLUKA began in the early seventies and was motivated by radiation shielding studies for the design of the Super Proton Synchrotron (SPS) at CERN [Ran70, Ran66]. The first versions of FLUKA were based on data from shielding experiments as well as on phenomenological parameterizations and the Thermodynamic Model [Hag66] for hadron production in high energy hadron-hadron collisions [Ran66]. "FLUKA" stands for *FLUktuierende KAskade* which reflects the necessity to describe fluctuations in energy deposition in calorimeters with purely analog MC methods.

Since that time FLUKA has been continuously improved and extended by an international collaboration of physicists and appears now as a multi-purpose MC code which is capable of simulating all components of particle cascades in matter from TeV-energies down to that of thermal neutrons. Its predictive power is based on a large number of studies benchmarking FLUKA results against experimental data (see [Fer95] and references therein).

This chapter gives a brief overview of the main physical concepts and models implemented in the present version of FLUKA. For more detailed information see [Flu98] and references therein.

2.6.1 Non-elastic Nuclear Interactions

A non-elastic nuclear interaction is described in FLUKA as a multi-step process involving various models each of which is acting in a different energy range.

The production of high-energy secondary particles from interactions of GeV-hadrons with nuclei is treated by the Dual Parton Model. These secondary particles propagate through nuclear matter and may interact with nucleons of the spectator nucleus. This is described in the framework of a Generalized Intranuclear Cascade Model which includes a description of the pre-equilibrium state of the spectator nucleus. Finally the excited spectator nucleus may evaporate nucleons and light fragments and dissipate energy through photon emission. In FLUKA these processes are treated by models for evaporation, fragmentation and γ-de-excitation.

2.6.1.1 The Dual Parton Model

Most particles produced in high-energy hadronic interactions have small transverse momenta with respect to the collision axis. The underlying interaction mechanisms are frequently called *soft processes*. In principle one would like to derive all features of these soft interactions from Quantum Chromodynamics (QCD) and perturbation theory since it appears as the accepted theory of strong interactions.

Soft hadron dynamics, however, involves interaction length scales of about 1 fm corresponding to strong coupling constants of the order of unity. This large value of the coupling constant prevents the application of perturbative QCD to soft processes. In contrast, phenomenological models proved to give rather accurate descriptions of soft interactions.

One of the most successful models in this field is the Dual Parton Model (DPM). A comprehensive review is given in [Cap94]. The DPM is based on the Dual Topological Unitarization (DTU) scheme [Cha75, Che76, Che78] and on perturbative Reggeon Field Theory (RFT) [Gri68, Bak76]. In this framework high-energy interactions are described by the exchange of *Reggeons* and *Pomerons*. In addition, the DPM incorporates the partonic structure of hadrons. A baryon is, therefore, assumed to consist of a valence quark, a valence diquark and a certain number of so-called *sea*-quark-antiquark pairs. Correspondingly, a meson is assumed to consist of a valence quark, a valence antiquark and also a certain number of sea-quark-antiquark pairs.

An inelastic hadron-hadron interaction is treated in two steps: (i) each colliding hadron splits into colored systems (valence and sea quarks) and (ii) each colored system of one of the colliding hadron combines with the system of complementary color of the other colliding hadron which, finally, fragments into color neutral *chains* of hadrons.

In order to describe inelastic interactions involving nuclei the DPM uses the Gribov-Glauber approximation [Gla55, Gri70, Ber72] which relates the inelastic hadron-nucleus interaction to inelastic scattering processes of the incoming hadron off individual nucleons.

The MC realization of the DPM which is implemented in FLUKA [Fer95] describes each hadron-nucleon interaction by the exchange of only one Pomeron or Reggeon and is, therefore, limited to laboratory energies below 20 TeV. Furthermore, this realization does not provide a description of nucleus-nucleus interactions.

In FLUKA the DPM is applied to hadronic interactions with laboratory energies down to 4 GeV. Scattering processes in the energy range between 2.5 GeV and 4 GeV are treated by a resonance production and decay model [Hän86].

2.6.1.2 Generalized Intranuclear Cascade Model

Particles produced in the interaction of the projectile hadron with target nucleons may propagate and reinteract in the part of the target nucleus which was not involved in the primary interaction (*spectator nucleus*). These processes are called *intranuclear cascade* (INC). The realization of the INC model implemented in FLUKA contains the following assumptions and features [Fer95]

- A nucleus is treated as a Fermi-gas of nucleons which are assumed to move independently from each other in a common single-particle potential. The single particle potential can be thought as the mean field resulting from all the two-body interactions among nucleons.
- Hadrons propagate in the nuclear medium between subsequent interactions like free particles on trajectories determined by refraction and reflection processes in the nuclear potential.
- Primary and secondary hadrons may interact with nucleons in elastic and inelastic scattering processes according to the local nuclear density. Mean free paths of hadrons are based on hadron-nucleon cross sections modified by various effects like Fermi motion of nucleons, Pauli's principle and the formation zone concept [Sto75, Ran89].
- Multibody absorption of pions, like the absorption on a deuteron, is considered. The transition between the intranuclear cascade and the final thermalization of the spectator

nucleus is described in FLUKA by a pre-equilibrium model [Sal94]. It is based on an exciton formalism called Geometry Dependent Hybrid Model (GDH).

At the end of the pre-equilibrium stage a compound nucleus in an equilibrium state is left. This nucleus is characterized by its charge, mass number and momentum and carries a certain excitation energy shared by the nucleons.

2.6.1.3 Evaporation, Fragmentation and Nuclear De-excitation

The excitation energy of the compound nucleus (*prefragment*) can be higher than the separation energy, thus, nucleons and light fragments can be still emitted. In FLUKA the emission process is described as an evaporation of nucleons, deuterium, tritium, ^{3}He and of α-particles from a hot system [Fer96] using excitation energy dependent level densities.

In case of heavy nuclei a fraction of the excitation energy might also be spent to induce collective deformations, *i.e.* to cause fission processes. In FLUKA the calculation of the fission probability is based on a statistical method [Fer96, Wei37, Boh39]. The masses of the two fragments obey charge and excitation energy dependent distributions [Fer95]. After the fission process both fragments are treated independently, being possibly able to emit further particles themselves.

For light prefragments the statistical assumptions and the sequential emission scheme which underlie classical evaporation models may become invalid. This can be due to the fact that a moderate excitation energy can already represent a substantial fraction of the total binding energy or that the mass of the "emitted" fragment is comparable to the mass of the prefragment. Therefore, in FLUKA the so-called Fermi Break-up model [Fer96, Fer70, Eph67] is applied to prefragments with mass numbers below 18. It is assumed that the excited prefragment disassembles in one step into two or more fragments. All combinations formed by up to six fragments are considered.

A similar process of nuclear fragmentation, frequently called *multi-fragmentation*, may occur in medium and heavy nuclei and is characterized by the "emission" of low energy complex fragments. It is not implemented in FLUKA.

Evaporation processes become energetically impossible when the nuclear excitation energy of a prefragment is lower than any energy necessary for nucleon or fragment emission. The residual excitation energy is then dissipated through the emission of photons.

In FLUKA the prefragment proceeds through consecutive photon emissions until the ground state of an isotope (*residual nucleus*) corresponding to the mass and charge of the prefragment is reached [Fer96].

2.6.2 Isotope Production

As discussed in [Fer96b] general features of the production of residual nuclei are well reproduced by FLUKA. Examples are the production cross section for a residual nucleus of a certain charge or mass number or the fission cross section.

Predictions on cross sections for the production of individual isotopes can, however, be wrong by large factors [Fer96b]. Reasons for these uncertainties include the fact that slight inaccuracies in excitation energy spectra reaching the evaporation stage can result in substantial shifts among close isotope yields and that multi-fragmentation is not considered.

In addition, production cross sections of some specific isotopes which might be important because of their long lifetime or activity represent often only a very small fraction of the total cross section.

Although comparisons of individual isotope yields with data have already shown promising results [Fer96b, Fer97] care has to be taken in the prediction of isotope yields with FLUKA where no data exist.

2.6.3 Elastic Nuclear Interaction

The elastic scattering of the hadrons from the nuclei can be very important if the target is small compared to the direction perpendicular to the hadron beam. The scattering is described in terms of the optical model [Wet81]. The optical potential is chosen as a sum of a central and a spin-orbit part, with a Woods-Saxon radial dependence for the real part, and a more periphery-peaked shaped imaginary part. The total elastic cross-section is typically half of the total inelastic cross-section and is parameterized by fitting to experimental data, after corrections for the Coulomb effect on proton scattering.

2.6.4 Particle Transport in Matter

One of the big advantages of FLUKA compared to other Monte-Carlo transport codes is the ability to transport, hadrons, muons, electrons, photons and low-energy neutrons in a single run, without any interface between the components. FLUKA is not an assembly of different codes. All the secondaries issued from the same primary particle are transported before a new particle history is started.

Transported particles

The following table shows all the particles which can be transported with FLUKA.

Common name	*FLUKA name*
Alpha	4-HELIUM
^{3}He	3-HELIUM
^{3}H	TRITON
Deuteron	DEUTERON
(Generic heavy ion: not implemented) (*)	HEAVYION
Optical photon	OPTIPHOT
Pseudoparticle	RAY (**)
Proton	PROTON
Antiproton	APROTON
Electron	ELECTRON
Positron	POSITRON
Electron Neutrino	NEUTRIE
Electron Antineutrino	ANEUTRIE
Photon	PHOTON
Neutron	NEUTRON
Antineutron	ANEUTRON
Positive Muon	MUON+
Negative Muon	MUON-
Kaon zero long	KAONLONG
Positive Pion	PION+
Negative Pion	PION-
Positive Kaon	KAON+
Negative Kaon	KAON-
Lambda	LAMBDA
Antilambda	ALAMBDA
Kaon zero short	KAONSHRT
Negative Sigma	SIGMA-
Positive Sigma	SIGMA+
Sigma zero	SIGMAZER
Pion zero	PIZERO
Kaon zero	KAONZERO
Antikaon zero	AKAONZER
Muon neutrino	NEUTRIM
Muon antineutrino	ANEUTRIM
(Heavy ion: obsolete)	HEAVYION
Antisigma minus	ASIGMA-
Antisigma zero	ASIGMAZE
Antisigma plus	ASIGMA+
Xi zero	XSIZERO
Antixi zero	AXSIZERO
Negative Xi	XSI-
Positive Xi	AXSI+
Omega minus	OMEGA-
Antiomega	AOMEGA+
Positive Tau (****)	TAU+
Negative Tau (****)	TAU-
Tau neutrino	NEUTRIT
Tau antineutrino	ANEUTRIT

For scoring also some generalized particles can be used

Common name	*FLUKA name*
All transportable particles	ALL-PART
All charged particles	ALL-CHAR
All neutral particles	ALL-NEUT
All negative particles	ALL-NEGA
All positive particles	ALL-POSI
Protons and neutrons	NUCLEONS
Protons, neutrons and charged pions	NUC&PI+-
For dose scoring: Deposited energy	ENERGY
For energy fluence scoring: Kinetic energy	ENERGY
Charged pions	PIONS+-
Primary (source or beam) particles	BEAMPART
Electromagnetic energy (of electrons, positrons or photons)	EM-ENRGY
Muons	MUONS
Electrons and positrons	E+&E-
Antiprotons and antineutrons	AP&AN
All Kaons	KAONS
All kaons and all hyperons and anti-hyperons (→ all strange particles)	STRANGE
Charged kaons	KAONS+-
Charged hadrons	HAD-CHAR
Fissions	FISSIONS
High energy fissions	HE-FISS
Low energy fissions	LE-FISS
Neutron balance (sum of outgoing neutrons minus incoming neutrons for all interactions)	NEU-BALA
Neutral hadrons	HAD-NEUT
Neutral kaons	KAONS0
Unbiased deposited energy (***)	UNB-ENER
Unbiased electromagnetic energy (of electrons, positrons or photons) (***)	UNB-EMEN

(*) Transport capabilities (dE/dx, with account of effective charge and effective charge straggling, multiple Coulomb scattering, no interaction yet) are now available for d, t, ^{3}He and ^{4}He. A limited transport capability (only dE/dx, scaled by mass and charge with account of effective charge) is available for heavier ions.

(**) A "RAY" is not a real particle, but a straight line trajectory through the FLUKA geometry. When a primary particle is found to be a RAY, the program tracks through the geometry in the given direction calculating a number of quantities (distance traversed in each material, number of radiation lengths, number of interaction lengths etc.).

(***) "Unbiased energy" means that the energy deposited (or the energy fluence) is scored with weight 1, independent of the actual weight of the particle. Of course, the result will have no physical meaning, but in some circumstances it will provide useful information about the run itself (for instance in order to optimize biasing).

(****) Only leptonic decays of Tau's are implemented for the time being.

Energy limits

	Secondary particles	**Primary particles**
charged hadrons	1 keV-20 TeV	100 keV-20 TeV
neutrons	thermal-20 TeV	thermal-20 TeV
antineutrons	50 MeV-20 TeV	100 MeV-20 TeV
muons	1 keV-1000 TeV	100 keV-1000 TeV
electrons	1 keV-1000 TeV	70 keV-1000 TeV (low-Z materials)
		150 keV-1000 TeV (high-Z materials)
photons	1 keV-1000 TeV	7 keV-1000 TeV

Transport of charged hadrons and muons

In transporting charged hadrons and muons from 1000TeV down to 10keV, FLUKA takes into account the following effects:

Energy loss: The energy loss (dE/dx) is calculated by using

- Bethe-Bloch theory [Bet30, Bet32, Bet34, Blo33, Blo33a], optional delta-ray production and transport with account for spin effects or Landau fluctuations [Lan44],
- Shell and other low-energy corrections derived from Ziegler [Zie77],
- density effect according to Sternheimer [Ste84].

Multiple Coulomb scattering: Special transport algorithm, based on Moliere's theory of multiple Coulomb scattering and further advanced by Bethe [Mol48, Mol55, Bet53] is used including several correlations, as, i.e., correlation between lateral and longitudinal displacement and the deflection angle, between projected angles, and between projected step length and total deflection.

Delta rays, pair production and Bremsstrahlung: In FLUKA they can be simulated in great detail relating to energy, angle and explicit transport of secondaries or they may be treated as continuous energy losses depending on user's choice.

Low-energy neutrons

Neutron collisions are followed and transported down to user-defined region-dependent energy cut-offs which can be as low as thermal energies. The model used here resembles the transport part of the neutron and γ-ray transport program MORSE [Emm75], incorporating many improvements concerning the code.

In cooperation with the Italian ENEA laboratory it was made possible to arrange cross-section data sets which contain data for some 130 elements, materials and isotopes which are frequently used in accelerator and detector technologies. Besides, they contain 72 neutron energy groups (or 37 wider groups), gamma production data and kerma factors for energy deposition calculations provided that they were available. For materials with appropriate data sets at a temperature of 87 Kelvin and approximately 0 Kelvin a Doppler reduced broadening was taken into account.

The transport is depicted by standard multigroup transport (P5) with photon and fission neutron production incorporating detailed kinematics of elastic scattering on hydrogen nuclei and transport of proton recoils and protons from N(n,p) reaction. Note that, photons which were emitted after a neutron capture are not transported in accordance with the multigroup treatment, but with the more accurate ElectroMagnetic Fluka (EMF) package which performs continuous transport in energy and additionally admits secondary electron production.

In general, for nuclei with the exception of hydrogen, kerma factors are employed to calculate energy deposition whereas in the case of hydrogen the recoiling protons are explicitly generated and transported.

Electrons

In FLUKA a fast-parameterized description of EM-cascades can be used, if only the gross energy deposition mechanisms are of concern. A detailed transport module for electrons and photons is also available which actually originates from the EGS4 code [Nel85] but it had to be altered and ameliorated. Completely new treatments were applied concerning multiple Coulomb scattering (including higher order Born approximations, spin effects and nuclear form factors), the photoelectric effect (simulated in greater detail with account of proper electron angular distribution, fluorescence and Auger electron emission), the Compton effect (new coding taking atomic binding into account, as well), Møller and Bhabha scattering and bremsstrahlung.

High energy photonuclear interactions were introduced, fully above 30 MeV (quasideuteron interactions, Vector Meson Dominance model) and for heavy nuclei in the Giant Resonance energy range.

Detailed delta-ray emission, shell corrections and updated density effect can be used to improve the stopping power calculations whereby special treatment is available for porous materials, where the average density differs from the local density.

Besides, high-energy effects regarding heavy charged particle transport were applied, as, i.e., electron pair production, bremsstrahlung and nuclear interaction via virtual photons.

In general, they affect all charged hadrons, but are particularly essential to the treatment of muons.

Photons

The following enumeration is essential concerning photon transport in FLUKA

- Pair production with actual angular distribution of electrons and positrons,
- Compton effect with respect to atomic bonds through the use of inelastic Hartree-Fock form factors,
- Photoelectric effect with actual photoelectron angular distribution [Sau31], detailed interaction on six K and L single sub-shells, optional emission of fluorescence photons and approximate treatment of Auger electrons,
- Rayleigh effect as in EGS4 [Nel85],
- Photon polarization is taken into account for Compton, Rayleigh and Photoelectric,
- Photohadron production: Vector Meson Dominance Model [Ran87b], modified and improved (Ferrari-Sala) using PEANUT below 770 MeV [Fas95].

Neutrinos

Electron, muon and tau (anti)neutrinos are generated and tracked at one's option, without interactions whereas neutrino interactions are implemented independently from tracking.

2.6.5 Geometry

FLUKA uses a combinatorial geometry package developed at ORNL (Oak Ridge National Laboratory) for the neutron and γ-ray transport program MORSE [Emm75] including additional bodies (infinite circular and elliptical cylinder parallel to X, Y, Z axis, generic plane, planes perpendicular to the axes). Complex objects can be defined by using the Boolean operations union, difference and intersection on pairs of objects.

A limited repetition capability (lattice capability) is now available which prevents describing repetitive structures in all details. Thus, only one single module has to be defined and can then be reiterated as frequently as needed. In essence, this allows to define geometries containing up to ten thousand different regions, as, i.e., spaghetti calorimeters by only using a small number of region and body definitions.

A geometry debugger detects double- or non-defined regions of the geometry and provides an ability to plot selected sections of the geometry (derived from the ISPRA PLOTGEOM program). The debugger also detects double- or non-defined regions of the geometry.

Note that a FLUKA input file can now be transformed into an Autocad script file by a Fortran program written by Helmut Vincke (CERN Division EP/ATI). This script file can then be used to generate a 3-dimensional drawing of the FLUKA geometry in Autocad including all features of Autocad like rendering, dimensioning etc. In addition, double- and non-defined regions can be found and plotted.

2.6.6 Biasing

Biased particle transport can be used in FLUKA to accelerate the calculations and to speed up the convergence of the results. A short summary is given below:

- Russian Roulette (RR) / Splitting for hadronic interactions,
- Importance Biasing at Boundaries,
- Weight Windows,
- Leading Particle Biasing,
- Decay length biasing,
- Decay direction biasing,
- Interaction Length Biasing,
- Neutron Non Analog Absorption,
- Neutron Biased Downscattering.

2.6.7 Tracking

An improved model for multiple scattering, derived from Moliere's theory [Mol47, Mol48, Mol55] and similar to the algorithm used in EGS4 [Nel85], is used and can now be applied for all charged particles [Fer91a]. This newly developed model is more productive and also pays attention to special high-energy effects, very grazing angles, correlations between angular, lateral and longitudinal displacements, backscattering near a boundary etc.

Furthermore, this model is completed by a sophisticated algorithm which assures a smooth approach of charged particles to boundaries by gradually shortening the length of the step as the particle gets closer to a boundary. This accurate tracking algorithm always calculates the distance to the nearest boundary which allows an exact transport to region boundaries and, thus, material discontinuities can be properly treated. Boundary crossing points are identified precisely even in the presence of very thin layers. Besides, the combined effect of multiple scattering and magnetic fields is included. On user's request, a predefined number of single scatterings can be performed when crossing a boundary, thus, avoiding artifacts due to step truncation. In materials of low density (gases) single scattering can either be requested or "switched off" in case of simulating interactions with residual gas in accelerator vacuum chambers.

2.6.8 Scoring

The original dose and star density scored in all defined regions of FLUKA86-87, is printed at the end of each standard output. Scoring as a function of angle was applied, both referring to the normal to a surface at the point of crossing and to a fixed direction. For the fixed direction one can calculate new quantities, as, i.e., rapidity, various kinematical quantities in the lab and in the center-of-mass frame, Feynman-x etc. Furthermore, it is possible to score residual nuclei in selected regions, and new facilities are available to simulate coincidences and anticoincidences in radiation detectors.

Dose and star density binning has always been a unique feature of FLUKA (only now similar scoring techniques managed to be implemented in some other codes). In the present version the power of this facility was increased with the result that instead of one binning structure of fixed mesh size, the user can now define as many structures as requested, even totally or partially overlapping, and the choice of each mesh is completely unrestricted.

On user's request R-Z binnings can be parallel with any of the three coordinate axes but do not necessarily have to coincide. Different kinds of symmetric binning around the origin can be specified. The mesh size does not affect the quality of dose binning even when the bins are much smaller than the particle step, because of a special algorithm which apportions the energy deposited with respect to the segment traveled by the particle in each bin.

In addition to traditional energy and star density, tracklength density (fluence) can now also be binned, providing detailed spatial fluence distributions.

2.6.9 Applications

In essence, FLUKA has always been a specialized program in order to calculate a multitude of applications in accelerator environment. Besides, traditional shielding, FLUKA is now used in many domains like target design taking into account target heating and optimized production of secondaries, calorimetry, prediction of activation, radiation damage, isotope transmutation, dosimetry and accelerator component design like scrapers, dumps etc.

The capability to deal with the low-energy neutron component of the cascade extended the field of interest to detailed radiation shielding, electronics and other sensitive detector parts. Moreover, radiation damage calculations and shielding designs are not restricted to proton accelerators any longer, but incorporate electron accelerators of any energy range, photon and muon factories, and any kind of radiation source, be it artificial or natural.

FLUKA is successfully employed in many domains as background studies for underground detectors, cosmic ray physics, detector design for radiation protection, shielding of synchrotron radiation hutches, evaluation of organ dose in a phantom due to external radiation, calculation of dose received by aircraft crews, as well as, for high energy physics, neutrino physics, electron and proton radiotherapy, nuclear transmutation, calculation of tritium production at electron accelerators, energy amplifiers, maze design for medical accelerators, testing of physical models etc.

Chapter 3

Production of Radioactive Isotopes in Molasse

The present cross-sections for the production of radionuclides in molasse are based on old data taken from rock close to the CERN Proton Synchrotron (PS). The CERN site is located in the Geneva Basin, which is filled by sedimentary deposits, collectively called molasse. For the NGS project, the CERN Neutrino Beam to Gran Sasso, as well as, for the LHC, the amount of radioactivity, which will be produced in the molasse rock, is of major importance. Therefore, several samples of molasse were taken from two different locations and were irradiated in the TCC2 area near the T4 target station. The radioisotopes produced were measured with a Ge-Detector. This experiment was also simulated with the Monte-Carlo cascade program FLUKA, in order to get the number of stars. A star is a hadronic inelastic interaction (spallation reaction) with an energy higher than a special threshold which, in general, is 50 MeV. The term "stars" originally comes from historic cosmic ray work in which high energy interaction events, with their large multiplicities, appeared as tracks originating from a point. Furthermore, this simulation permitted an estimation of the hadron fluence distribution in energy and the production of residual-nuclei in the molasse samples. The present simulations were carried out using FLUKA97.5, see references [Fas97, Fer97] and the references they contain. The FLUKA code was extensively benchmarked against experimental data over a wide energy range for both hadronic and electromagnetic showers [Aar94, Bir94, Bir96, Fas97a, Fer92, Fer97b].

3.1 Molasse Samples

Molasse samples used for the irradiation were taken from two drillings (see Figure 3.1), namely SLHC 43 and SLHC 44. These two positions were chosen because they are located close to the planned neutrino target cavern and close to the hadron stopper area of the newly planned neutrino facility (NGS). The samples were taken from the deepest point of the two drillings (60 m for SLHC 43 and 110 m for SLHC 44). Samples from SLHC 9 and SLHC 10, both located closer to the target station and the stopper area, were not available. For the calculations of the induced radioactivity it is necessary to know the chemical composition of the molasse rock. Therefore, four samples were sent for the chemical analysis to the EMPA laboratory in Dübendorf [EMPA].

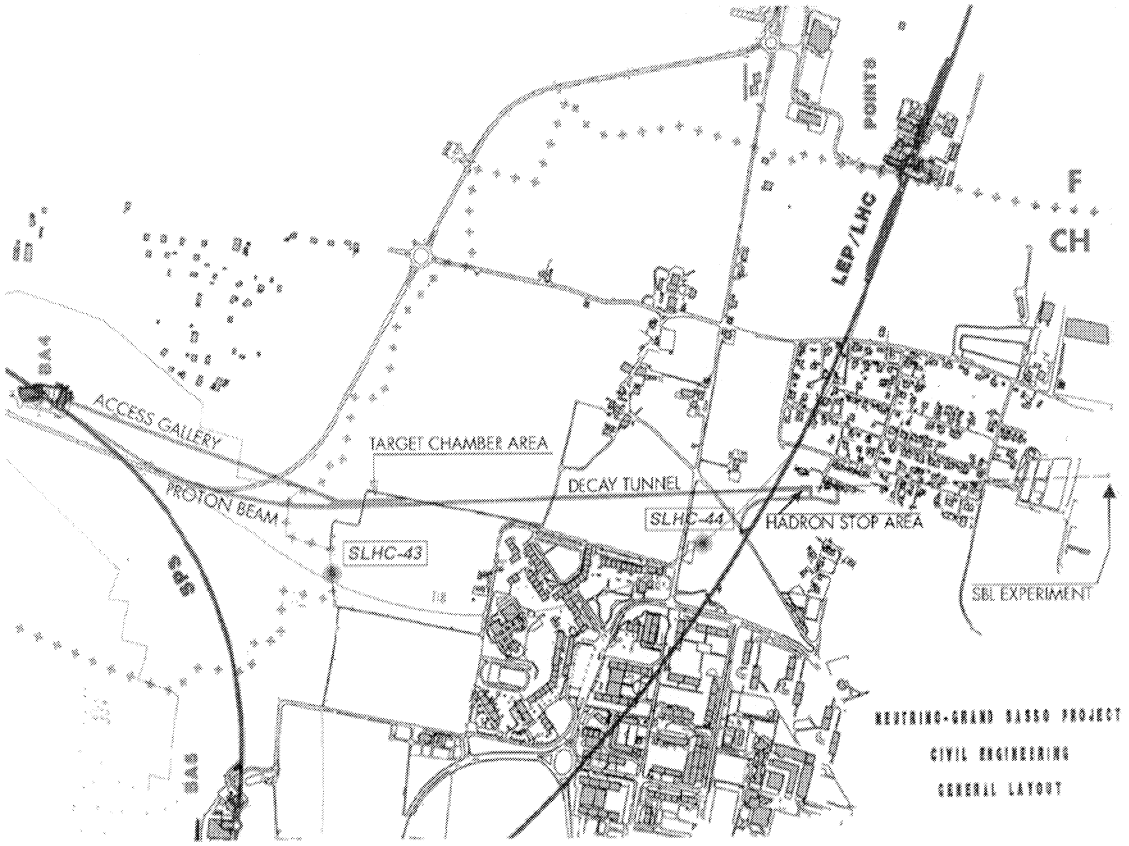

Figure 3.1: *Layout of the NGS at and around CERN including the 2 positions of the drillings SLHC-43 and SLHC-44.*

3.2 Irradiation

The irradiation of 5 molasse rock samples took place in the TCC2 area from end of July 98 until beginning of September 98. The powdered molasse was filled into cylindrical plastic receptacles (6 cm in diameter and 2 cm in height), weighing about 60 g, and were then exposed downstream on the first magnet after the T4 target, namely MTN 040003. This location was chosen because of the high intensity which was needed for this experiment. During the irradiation of the molasse samples, NA48 was running from T10 downstream of T4. Details of the proton intensities on the target T4 are given in Figure 3.2. The number of 450 GeV protons on the 200 x 160 x 2 mm^3 Beryllium target in T4 was typically 4-5 $\times$ 10^{12} per pulse. In order to simulate the rock behind the concrete structure of a target cavern some concrete blocks were put between the magnet and the rock samples. The following paragraph particularly describes the geometry, the origin and the position of the molasse samples, see Figure 3.3 and Table 3.2. The irradiation time of the five molasse samples, and the number of protons hitting target T4 during the exposure are given in Table 3.1.

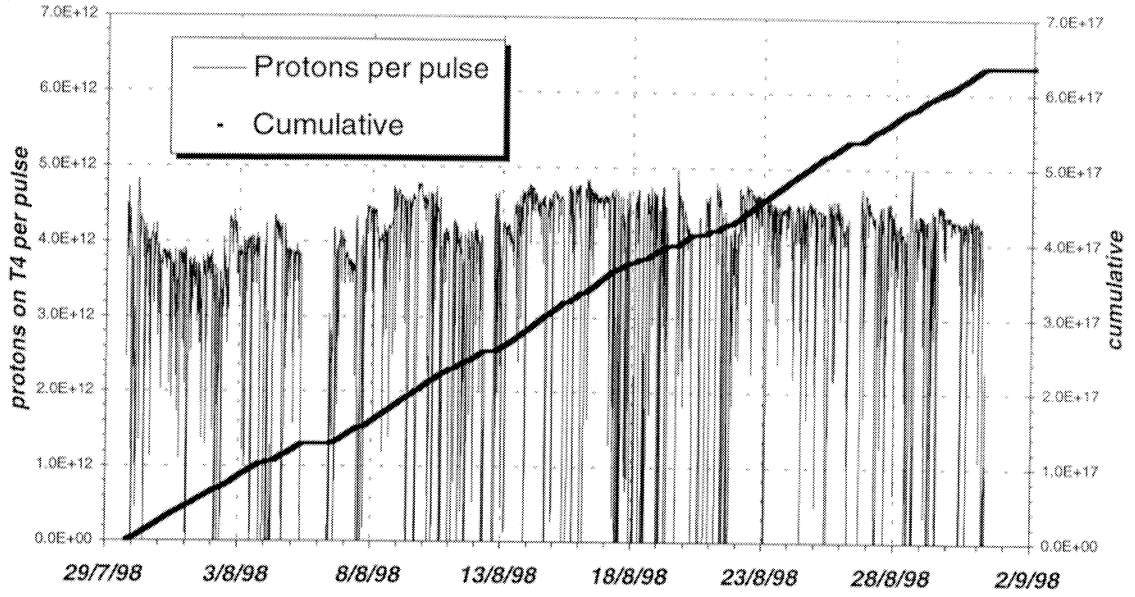

Figure 3.2: *Number of protons hitting target T4 during the irradtiation of the molasse samples.*

Table 3.1: *Irradiation time and number of protons on T4 during the irradiation.*

Sample number	Irradiation period	Protons on T4
1	22/7/97 16:00 - 29/7/97 8:00	1.413×10^{17}
2	22/7/97 16:00 - 29/7/97 8:00	1.413×10^{17}
3	22/7/97 16:00 - 29/7/97 8:00	1.413×10^{17}
4	22/7/97 16:00 - 31/8/97 6:00	7.773×10^{17}
5	29/7/97 18:00 - 31/8/97 6:00	6.360×10^{17}

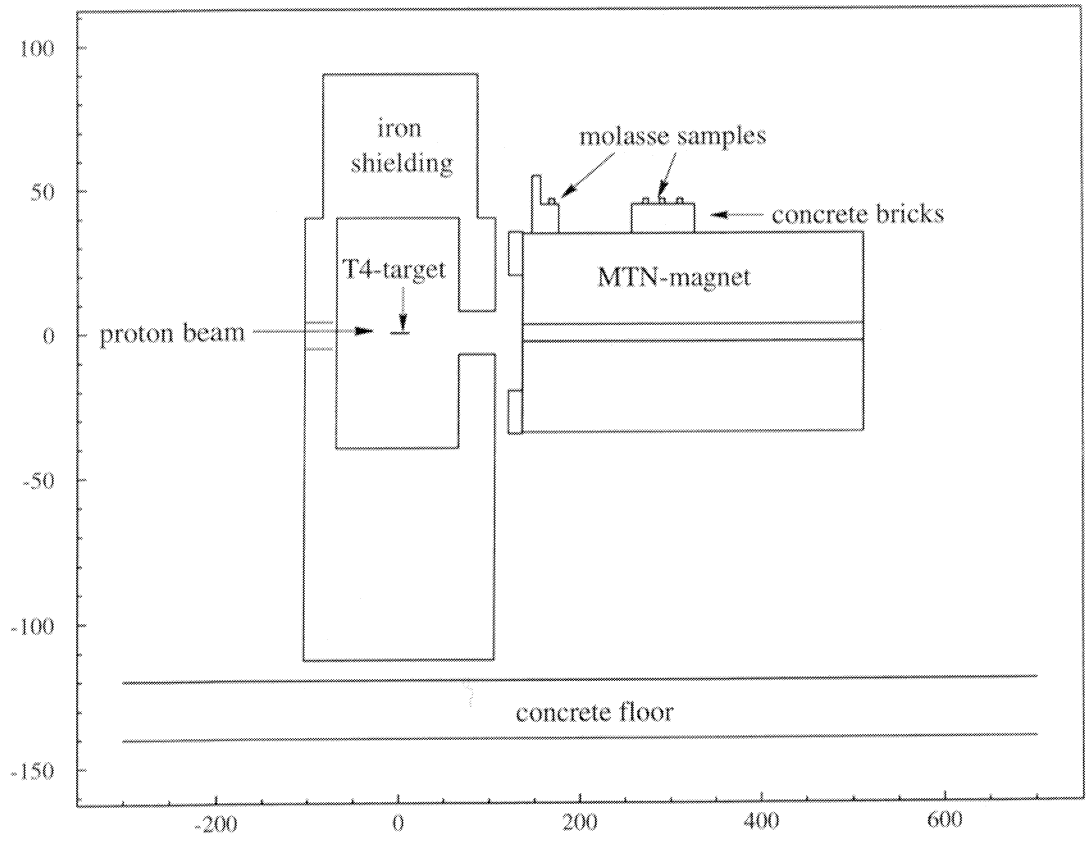

Figure 3.3: *Longitudinal section through the T4 target station. Dimensions are in cm.*

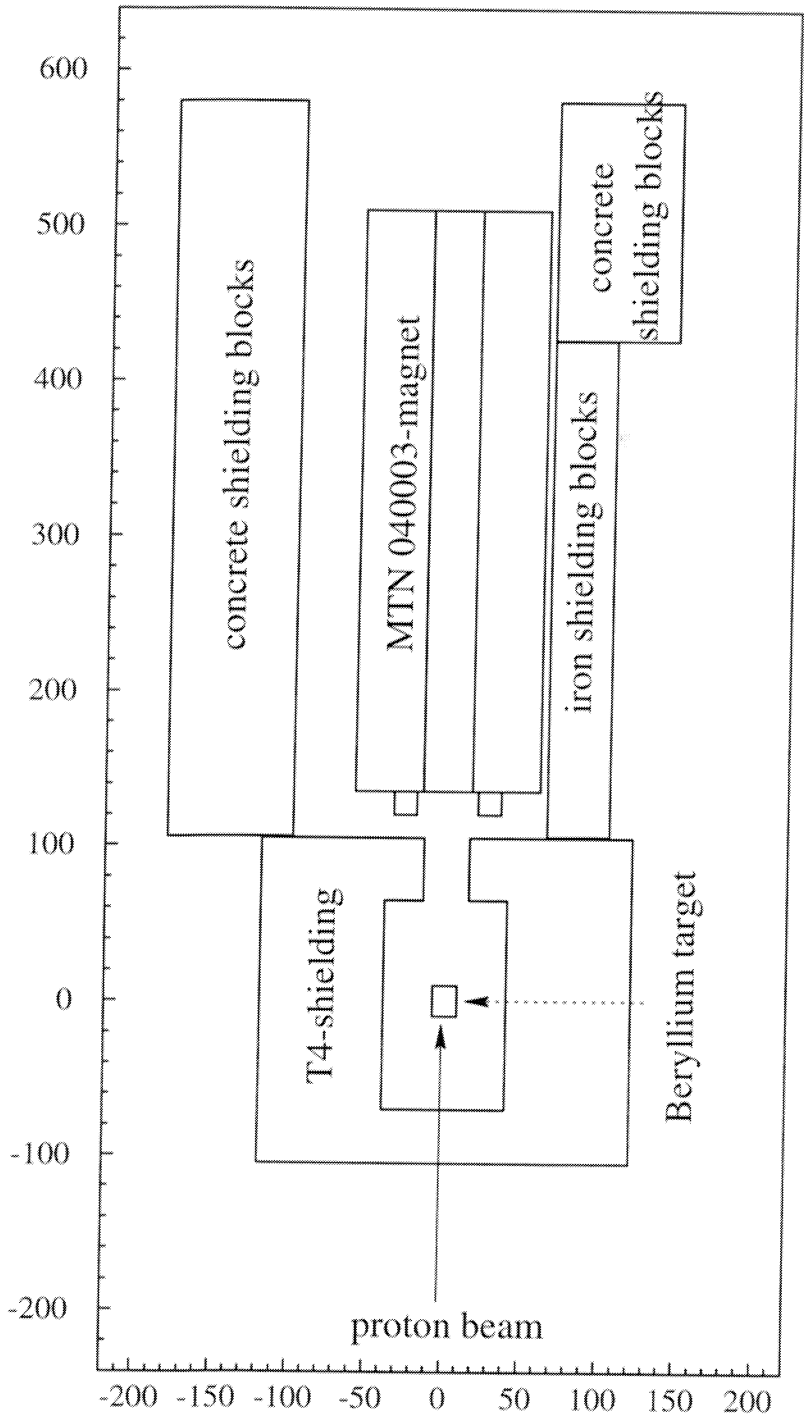

Figure 3.4: *Horizontal section at beam height through the T4 target station. Dimensions are in cm.*

3.3 Details of the Simulations

A simulation of the irradiation experiment was carried out by using FLUKA97.5. In the present study FLUKA was used to simulate all components of the cascades from 450 GeV to the energy of thermal neutrons. The following section defines main parameters for the FLUKA calculations which were essential.

Coordinate System:

The geometry was described in a right-handed orthogonal system with x as the vertical axis, y as the axis pointing to the right of the receding proton beam and z as the direction of the proton beam. The beam axis is centered on the origin of the xy-plane. The z origin is at the focal plane of the proton beam within the target.

Source Particles:

The point of entry of the 450 GeV protons into the system was taken to be 1 cm in front of the upstream face of the target. The horizontal spot size and the divergence of the proton beam at T4 were experimentally observed to be: ±0.6 mm, ±0.15 mrad. (r.m.s.), and the vertical: ±0.1 mm, ±0.3 mrad. (r.m.s.), respectively.

Geometry:

A longitudinal section through the target assembly, the collimator which is immediately downstream of the target, the MTN-magnet, the concrete bricks and the molasse samples is given in Figure 3.3. A horizontal section at beam height through the target station is depicted in Figure 3.4. The lateral shielding along the right hand side of the magnet (seen from the beam direction) is made of iron blocks followed by concrete blocks whereas the shielding along the left hand side only consists of concrete blocks. The target is composed of a Beryllium plate $200 \times 160 \times 2$ mm^3 in size.

Table 3.2: *Positions of the molasse samples (see Figure 3.3).*

Sample number	z-coordinate in cm	Origin
1	271	SLHC-43
2	289	SLHC-43
3	309	SLHC-43
4	289	SLHC-44
5	170	SLHC-43

Material Assignments:

The chemical composition of the molasse from SHLC-43 and SLHC-44 is described in Table 3.3. The composition was taken from the chemical analysis report of molasse. Corresponding to this analysis, the density of the powdered molasse sample is 1.26 g/cm^3.

Table 3.3: *Chemical composition of molasse from SLHC-43 and SLHC-44.*

Element	SLHC -43 in g/100g	SLHC -44 in g/100g
O	49.2	49.3
Si	19.8	19.6
Ca	9.3	10.0
Al	6.35	6.35
C	4.9	5.0
Fe	4.1	3.7
Mg	3.5	2.9
K	1.9	1.6
Na	0.57	0.37
Mn	0.135	0.06
Ti	0.07	0.07
P	0.04	0.02
Sr	0.04	0.08
Cr	0.016	0.018
Zn	0.01	0.009
Ni	0.009	0.01
V	0.007	0.009
Ba	0.006	0.006
Cu	0.004	0.004
Co	0.003	0.002
Ce	0.002	0.003
Eu	0.00007	0.00008

The concrete shielding blocks were assumed to have a density of 2.35 g/cm^3 and the following chemical composition (the values in brackets give the corresponding mass fractions): oxygen (51.1%), silicon (35.8%), calcium (8.6%), aluminum (2.0%), iron (1.2%), hydrogen (0.6%), carbon (0.4%) and sodium (0.3%).

The shielding around the T4 target and alongside the magnet was taken to be cast iron, with a density of 7.2 g/cm^3, and to contain 5% of carbon. The MTN-magnet was assumed to be pure iron, with a density of 7.88 g/cm^3. The coil of the magnet was made of copper with a density of 8.96 g/cm^3. All other regions were filled with air at S.T.P.

Particle Energy Thresholds:

The simulations were aimed at determining star densities in the different samples, therefore, the lower thresholds for particle transport were set to 50 MeV for all hadrons. Neutral pions, electrons, photons, and neutrinos were not transported in the simulations, as they do not significantly contribute to the production of radioactive nuclei.

In the calculations of the track-length in the molasse samples, the lower thresholds for particle transport were set to 10 MeV for all hadrons except neutrons which were followed down to thermal energies.

Biasing:

In order to enhance the statistical accuracy of the results, significant use of region-importance biasing was made. The survival probability of thermal neutrons was set to be 0.9 in order to avoid undue time being wasted on tracking them.

Scoring:

The number of stars (inelastic interactions of hadrons having kinetic energies greater than 50 MeV) was recorded as the total number of stars occurring in the molasse samples. Separate accounts were kept for neutrons, protons, and charged pions; other hadrons were included in an "all-hadron" star counter.

The track-lengths of neutrons below 19.6 MeV were scored by summing particle track-lengths of two of the molasse samples according to the FLUKA multi-group energy structure below this energy. Dividing the total track-lengths by the volume in which they were calculated gives the particle fluence.

Furthermore, the production of the residual nuclei was calculated directly in a FLUKA simulation, eliminating the relevant partial cross-sections. The results depend on the quality of the physics models. The following is of central importance: the modeling of nuclear evaporation, the intranuclear cascade, nuclear fission, and nuclear fragmentation. The first three of them are considered to be well modeled but fragmentation, important for medium mass and heavy mass target nuclei, is not included in the code. Residual nuclei data should, therefore, give reasonable results for lighter target materials but could also lead to an underestimation of the yield of some medium mass or heavy mass isotopes.

All the quantities scored were normalized to one incident beam proton.

3.4 Gamma Spectroscopy

The gamma-rays from radioisotopes in the molasse samples were measured with a Ge-detector. The gamma spectroscopy was carried out by using Canberra's Genie-2000 spectroscopy software and the PROcount-2000 counting procedure software. This software package is a comprehensive environment for data acquisition, display and analysis. The Genie-2000 Gamma Analysis Software which is part of the whole package, includes a set of advanced spectrum analysis algorithms. These algorithms provide a complete analysis of gamma ray spectra, for example, nuclide identification, interference correction, weighted mean activity, background subtraction and efficiency correction.

After the molasse samples had been irradiated, their activity was first measured after 3 days then after 1 week and, finally, after 30 days. The peaks in the spectra, coupled with a precise energy calibration, could be used to determine the nuclides in the sample. The software provides nuclide identification through peak searches of spectra and scans of standard and user-generated nuclide libraries. In this study, a user generated library was used which was based on the chemical composition of the rock samples and all the possible isotopes which could be created by the irradiation. It should be mentioned that the software provides an additional capability of resolving overlapping peaks into individual components. The final step in nuclide analysis was to determine the intensity of the radioactivity corresponding to each isotope related to the end of the irradiation time.

3.5 Activities in the Molasse Samples

3.5.1 Natural Radioactivity

Four molasse rock samples were used to determine the natural radioactivity in molasse. The powdered samples were contained in small cylindrical plastic receptacles. Afterwards they were measured in a Ge-Detector for 2 days. Results are summarized in Table 3.4. The main contribution to the radioactivity is coming from K-40 with small contributions from thorium and uranium decays. It should further be noted that the results from sample SLHC-43 and SLHC-44 do not differ very much, which leads to the assumption of equal quantities of natural radioactivity around the target cavern and the hadron stopper area of the planned NGS-facility. The results are in fairly good agreement with the activity concentrations given in [UN88] and in [HealthPhysics]. Another paper, see [Pir96], also contains measurements of the natural radioactivity in molasse. In that report the amount of radioactivity due to K-40 is nearly the same, whereas the natural activity from the uranium and the thorium decay series is much higher than measured in this study.

Table 3.4: *Natural radioactivity in molasse samples from drilling SLHC-43 and SLHC-44.*

Radionuclide or Decay series	SLHC-43/1 Bq/g	SLHC-44/1 Bq/g	SLHC-43/2 Bq/g	SLHC-44/2 Bq/g
K-40	0.49 ± 9%	0.44 ± 8%	0.45 ± 14%	0.44 ± 13%
Th-232	0.029 ± 6%	0.028 ± 5%	0.025 ± 13%	0.027 ± 13%
U-238	0.024 ± 7%	0.017 ± 9%	0.023 ± 14%	0.026 ± 12%

3.5.2 Induced Radioactivity

The radioactivity in the molasse samples is produced either by spallation reactions or by radiative neutron capture. The (γ, n) reactions usually have only small cross-sections and are only of little importance to proton accelerators. The activity of γ-emitting radioisotopes induced in the molasse samples, after different irradiation times (see Table 3.1) and without cooling time, are represented in Table 3.5. Note that radioisotopes with half-lives shorter than 5 days are not taken into account. From this table it can be concluded that the radioactivity coming from radioisotopes which have a half live greater than 50 days, is dominated by ^{7}Be, ^{46}Sc and ^{59}Fe ^{7}Be is produced by spallation whereas ^{46}Sc is formed by spallation, as well as, by low energy neutron capture. Like many other isotopes, ^{59}Fe is mainly produced by the capture of thermal neutrons. Worthy of remark is the detection of ^{233}Pa in the molasse samples. This isotope is produced by thermal neutron capture followed by a β^- decay

$$^{232}\mathrm{Th}(n, \gamma)\ ^{233}\mathrm{Th} \rightarrow\ ^{233}\mathrm{Pa}.$$

A summary of the production channels and decay properties of each isotope is given in Appendix A. Further should be emphasized that pure β–emitting isotopes are not included in the table because these isotopes can not be detected with the Ge-detector. For the calculation of the production of these isotopes the residual nuclei option in FLUKA was used. A bar-plot of the produced radionuclides in sample 1 is shown in Figure 3.5.

Table 3.5: *Induced radioactivity of γ emitting isotopes in molasse at the end of the irradiation.*

Radio-Nuclide	Half-life	Sample 1 Bq/g	Sample 2 Bq/g	Sample 3 Bq/g	Sample 4 Bq/g	Sample 5 Bq/g
^{7}Be	53.3 d	199.7 ± 5%	178.0 ± 4%	150.9 ± 5%	933 ± 5%	2162.0±5%
^{22}Na	2.60 y	8.76 ± 4%	7.90 ± 4%	6.73 ± 4%	37.8 ± 4%	87.9 ± 4%
^{46}Sc	83.8 d	38.5 ± 3%	53.9 ± 3%	33.7 ± 3%	217.2 ± 4%	178.0 ± 3%
^{48}V	24.0 d	22.9 ± 2%	20.6 ± 3%	17.6 ± 3%	91.5 ± 2%	253.1 ± 3%
^{51}Cr	27.7 d	100.5 ± 4%	110.3 ± 3%	84.8 ± 3%	425.1 ± 4%	829.4 ± 3%
^{52}Mn	5.59 d	102.3 ± 2%	93.5 ± 2%	78.2 ± 2%	350.0 ± 3%	1034.9±2%
^{54}Mn	313 d	14.4 ± 3%	13.4 ± 3%	11.4 ± 3%	59.8 ± 3%	143.4 ± 3%
^{59}Fe	2.70 y	24.1 ± 3%	35.3 ± 3%	21.6 ± 2%	110.4 ± 3%	92.0 ± 3%
^{56}Co	78.8 d	0.78 ± 3%	0.77 ± 3%	0.54 ± 3%	2.6 ± 3%	6.2 ± 3%
^{57}Co	271 d	0.20 ± 2%	0.20 ± 2%	0.15 ± 3%	0.82 ± 2%	2.2 ± 2%
^{58}Co	70.8 d	0.71 ± 6%	0.62 ± 5%	0.54 ± 6%	2.92 ± 6%	6.20 ± 5%
^{60}Co	5.27 y	4.5 ± 3%	18.0 ± 3%	6.3 ± 4%	4.2 ± 3%	17.9 ± 3%
^{65}Zn	244 d	1.3 ± 4%	2.1 ± 5%	1.2 ± 4%	7.5 ± 4%	5.5 ± 4%
^{86}Rb	18.7 d	61.1 ± 4%	72.4 ± 4%	50.3 ± 4%	267.2 ± 5%	288.8 ± 4%
^{134}Cs	2.06 y	4.0 ± 2%	4.9 ± 3%	3.2 ± 2%	21.0 ± 3%	16.5 ± 3%
^{131}Ba	11.8 d	4.6 ± 7%	5.3 ± 6%	3.8 ± 7%	13.4 ± 7%	26.7 ± 8%
^{141}Ce	32.5 d	2.5 ± 6%	3.6 ± 5%	2.4 ± 6%	9.7 ± 5%	10.5 ± 6%
^{152}Eu	13.3 y	1.4 ± 4%	1.8 ± 4%	1.2 ± 4%	9.3 ± 4%	5.0 ± 4%
^{154}Eu	8.8 y	0.10 ± 4%	0.14 ± 5%	-	1.41 ± 4%	-
^{160}Tb	72.3 d	2.4 ± 5%	3.0 ± 5%	2.2 ± 6%	16.1 ± 5%	11.6 ± 5%
^{181}Hf	42.0 d	0.9 ± 6%	1.2 ± 5%	0.7 ± 5%	5.3 ±6 %	3.7 ± 5%
^{182}Ta	115 d	3.0 ± 3%	3.8 ± 4%	2.4 ± 4%	17.0 ± 4%	13.1 ± 4%
^{233}Pa	27.0 d	16.4 ± 3%	21.1 ± 3%	9.7 ± 3%	80.0 ± 3%	70.5 ± 3%

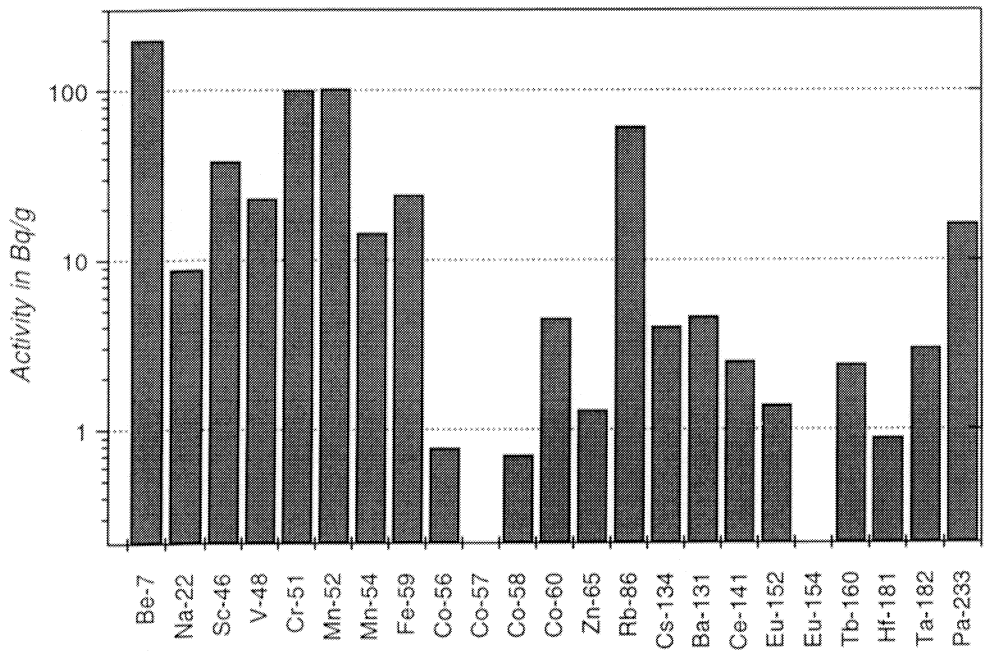

Figure 3.5: *Induced radioactivity in molasse sample 1.*

3.6 Results of the Monte-Carlo Calculations

3.6.1 Star Density

The principle method used in practice to determine rock activities in a Monte-Carlo simulation requires knowledge of the star production. Table 3.6 contains the numbers of stars scored per incident proton and per g molasse in the different samples. Separate counts were kept for neutrons, protons, and charged pions; all other hadrons were included in an "all hadron" star counter. The values for the total number of stars (all hadrons) were used to calculate the production of radionuclides per star. Statistical uncertainties of the values for the hadron data are equal or below 4 percent. Furthermore, it can be seen that more than 80% of all stars are due to neutrons.

Table 3.6: *Number of stars (E > 50 MeV) per proton and per g molasse in different molasse samples.*

Sample number	All hadrons	Protons	Neutrons	Charged pions
1	9.22×10^{-7}	7.58×10^{-8}	7.71×10^{-7}	7.00×10^{-8}
2	7.28×10^{-7}	4.33×10^{-8}	6.53×10^{-7}	1.74×10^{-8}
3	6.60×10^{-7}	1.56×10^{-8}	6.06×10^{-7}	2.56×10^{-8}
4	7.28×10^{-7}	4.33×10^{-8}	6.53×10^{-7}	1.74×10^{-8}
5	1.95×10^{-6}	1.43×10^{-7}	1.67×10^{-6}	1.21×10^{-7}

3.6.2 Residual Nuclei

The production rate of isotopes in the molasse samples was calculated with FLUKA97 by scoring the residual-nuclei production. The hadron-nucleus interactions, in an energy range between 0.02 and 2.5 GeV, are described by a pre-equilibrium model. This model includes an accurate model of the nuclear potentials and, therefore, it should give fairly good results. It must be noted that multi-fragmentation is not implemented in FLUKA97, which is negligible for light target isotopes but can lead to an underestimation of the yield of light isotopes which will be produced by interactions on medium- and high-mass targets. Nevertheless, for radionuclides close to the parent, FLUKA97 results are very accurate. Furthermore, it should be mentioned that in FLUKA97 it is now possible to score some isotopes which were produced by low energy neutrons. In Table 3.7 the yields of radioisotopes per star produced in the molasse with half-lives greater than a few days are summarized.

3.6.3 Track-lengths

In most cases, a fast neutron entering into matter will scatter back and forth on the nuclei, both elastically and inelastically, losing energy until it comes into thermal equilibrium with the surrounding atoms. At this point, it will diffuse through matter until it is finally captured by a nucleus or enters in some other type of nuclear reaction, i.e. fission. The neutron, of course, might undergo a nuclear reaction, might be captured or escapes from the system before attaining thermal energies, especially if resonances are present.

Many of the produced isotopes in molasse come from neutron activation. Some of them are pure β-emitters and, therefore, they can not be detected with the Ge-detector. In order to study in more detail the production of ^{45}Ca and ^{55}Fe, which were of major interest, it was essential to calculate the tracklength of neutrons in the samples down to thermal energies.

Table 3.7: *Residual nuclei production (only isotopes with half-lives greater 5 days).*

Radionuclide	Half-life	Atoms per Star
^{3}H	12.4 y	0.03 ± 3.6%
^{7}Be	53.3 d	0.011 ± 4.1%
^{10}Be	1.60×10^{6} y	0.006 ± 5.3%
^{14}C	5730 y	0.016 ± 1.2%
^{22}Na	2.60 y	0.009 ± 2.7%
^{26}Al	7.12×10^{5} y	0.015 ± 3.5%
^{32}P	14.3 d	0.0019 ± 6.5%
^{33}P	25.4 d	0.0023 ± 6.1%
^{35}S	87.4 d	0.00066 ± 3.1%
^{36}Cl	3.0×10^{5} y	0.015 ± 3.5%
^{37}Ar	35.0 d	0.027 ± 2.5%
^{39}Ar	269 d	0.013 ± 2.8%
^{41}Ca	1.03×10^{5} y	0.19 ± 1.8%
^{45}Ca	163 d	0.007 ± 1.9%
^{46}Sc	83.8 d	0.00015 ± 9.2%
^{44}Ti	47.3 y	0.00002 ± 16.8%
^{48}V	24.0 d	0.00057 ± 9.4%
^{49}V	330 d	0.0012 ± 5.5%
^{51}Cr	27.7 d	0.003 ± 8.5%
^{52}Mn	5.59 d	0.00065 ± 7.1%
^{54}Mn	313 d	0.007 ± 8.4%
^{55}Fe	2.70 y	0.023 ± 8.0%
^{59}Fe	44.5 d	0.0007 ± 9.0%
^{56}Co	78.8 d	0.00007 ± 9.3%
^{57}Co	271 d	0.00002 ± 12.1%
^{58}Co	70.8 d	0.00003 ± 10.4%
^{60}Co	5.27 y	0.0025 ± 10.8%
^{63}Ni	100 y	0.00017 ± 19.0%

The spectra were scored in sample 1 and sample 5 and are given in Figure 3.6. These two samples were chosen because the calculated low energy neutron flux (E < 19.6 MeV) differed at these positions. The production of radioactivity per proton can be calculated from

$$A = \lambda \int \{1 - \exp[-n\sigma(\mathrm{E})\Lambda(\mathrm{E})]\}\,\mathrm{d}E \quad \mathrm{Bq}, \qquad (3.23)$$

where λ is the decay constant of the radionuclide, n is the atomic concentration of the isotope in molasse per cm^3, $\sigma(E)$ is the energy dependent neutron capture cross-section for the production of the radionuclide and Λ is the tracklength per proton of the neutron with energy E. In order to verify the results some calculations were carried out concerning the production of ^{46}Sc, ^{59}Fe, ^{60}Co and ^{152}Eu. These results were compared with the experiment and can be found in Table 3.8. Although FLUKA is only using a 72 group structure for the low-energy (E < 19.6 MeV) neutron transport the results show a very reasonable agreement. It should be further emphasized that ^{46}Sc is produced by spallation, as well as, by neutron capture. The discrepancy between the experiment and the FLUKA calculation can be explained because the latter does not contain the direct production of ^{46}Sc from spallation. The neutron capture cross-section plots, which were used for the calculation, are given in Appendix B. They are based on ENDF/B-VI cross-section data sets, except the ^{44}Ca(n, γ) ^{45}Ca cross-sections, which were extracted from the JENDL-3.1 data. All data was obtained from the IAEA's Nuclear Data Centre, see [IAE].

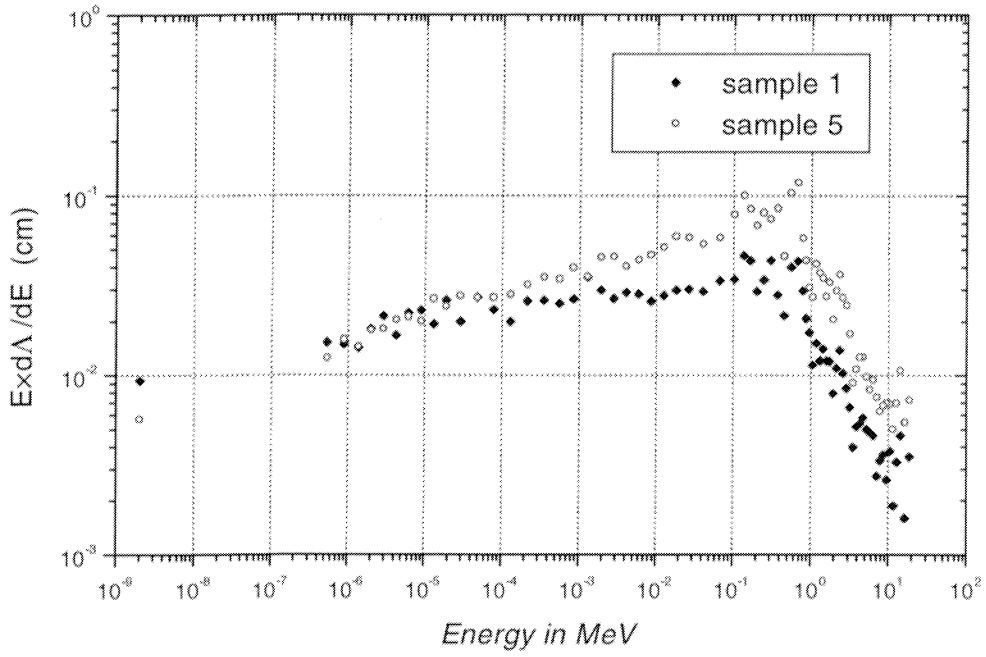

Figure 3.6: *Energy spectra of neutrons (E < 19.6 MeV) in sample 1 and sample 5 per primary proton.*

Table 3.8: *Comparison of the production of selected radionuclides between the experiment and the FLUKA calculation. All units are in Bq/g.*

Nuclide	Sample 1		Sample 5	
	experiment	FLUKA	Experiment	FLUKA
^{45}Ca	-	62.4	-	181.6
^{46}Sc	38.5	25.2 [1]	178.0	75.9 [1]
^{55}Fe	-	23.0	-	74.7
^{59}Fe	22.0	24.1	92.0	81.8
^{60}Co	4.5	4.0	17.9	15.7
^{152}Eu	1.4	1.4	5.0	4.3

3.7 Production of Radioactive Isotopes in Molasse per Star

The measured or calculated activity in the different molasse samples provided a successful possibility to determine the number of isotopes produced per star. The star-densities in the molasse samples are given in section 3.6.1. The production rate of isotope j, X_j, can be defined by

$$X_j = p\, K_j\, n_{star}, \tag{3.24}$$

where p is the proton intensity on the target per second, K_j is the production of the isotope j per star and n_{star} is the number of stars per proton. The number of atoms N_j of the radionuclide j, will be governed by the following differential equation during the period of irradiation

$$\frac{\mathrm{d}N_j(t)}{\mathrm{d}t} = -\lambda_j N_j(t) + X_j, \tag{3.25}$$

where λ_j is the decay constant of the isotope j and X_j is the production rate of radioactive isotope. On the right hand side of equation (3.25), the first term represents the loss of the radionuclides through decay during irradiation while the second term represents the gain of radionuclides through the production reaction. Thus, the activity of isotope j induced in the molasse rock as a function of irradiation time t_{irr} is given by $A_j = \lambda_j N_j$, hence

[1] See text in chapter 3.6.3

$$A_j(t) = X_j\,[1 - \exp(-\lambda_j\, t_{irr})]\,. \qquad (3.26)$$

Table 3.9 contains the numbers of radioactive isotopes produced in molasse per inelastic interaction above 50 MeV (star) and with half-lives greater than a few days. The column 'Experiment' contains all values, which were measured in the experiment. 'Spectrum' are the values determined by folding the low-energy (E_n<19.6 MeV) neutron flux in each FLUKA group by the appropriate (n, γ) cross-section and 'Resnuc' are the atoms per star factors from the 'Residual Nuclei' output of FLUKA. The activity of the molasse samples was measured with a Ge-Detector and, therefore, only γ emitting isotopes are contained in the 'Experiment' column. The 'Spectrum' calculations were only carried out for those isotopes which were of particular interest. It should be mentioned that the residual nuclei information is not available for all elements. Consequently, most of the isotopes produced by thermal neutron activation could not be calculated. The column 'old value' shows the numbers which were used in previous calculations for molasse and which are based on irradiated samples close to the CERN-PS. The irradiation of these samples was carried out in 1987 near the AA target, therefore, see reference [Sul87]. From this study the atoms per star factors were calculated. It should be noted that an exact chemical composition of the molasse was not available at that time and, hence, the 'known' composition of glacial till was used for molasse. Taking this fact into account, the difference between the 'old' and the 'new' values can easily be resolved. Nevertheless, there is still a good agreement between the production rates for ^{45}Ca, ^{54}Mn, ^{152}Eu and ^{154}Eu, whereas the production rate is nearly 9 times higher for ^{46}Sc and 4 times higher for ^{7}Be. The rate for ^{22}Na production dropped from 0.011 to 0.0084 atoms per star and, in addition, the ^{3}H production probability from 0.05 to 0.03. The yield of the ^{49}V production per star was calculated by using the ratio of the residual nuclide production of ^{49}V and ^{48}V from FLUKA and multiplying this ratio with the 'measured' value of ^{48}V. Moreover, the same nuclide per star factor was used for ^{131}Ba and ^{133}Ba because both elements have nearly the same abundance and the low-energy neutron capture cross-sections of ^{130}Ba and ^{132}Ba are quite similar.

The values of isotopes produced predominantly by spallation are within statistical uncertainties, independent of position. This was to be expected as the production of these isotopes is proportional to the star density rate. Those radionuclides produced from low energy neutrons and thermal neutrons, however, vary somewhat because the low energy neutron fluences will not be directly proportional to the star density rate.

Table 3.9: *Data for radionuclides produced per star in molasse with half-lives greater than 5 days.*

Radionuclide	Half-life	Experiment	Spectrum	Resnuc	old value	new value
^{3}H	12.4 y	-	-	0.03 ± 4%	0.05	0.03
^{7}Be	53.3 d	0.0118 ± 5%	-	0.011 ± 4%	0.003	0.012
^{10}Be	1.60×10^{6} y	-	-	0.006 ± 5%	-	0.006
^{14}C	5730 y	-	-	0.016 ± 1%	-	0.016
^{22}Na	2.60 y	0.0084 ± 2.5%	-	0.009 ± 3%	0.011	0.0084
^{26}Al	7.16×10^{5} y	-	-	0.015 ± 4%	-	0.015
^{32}P	14.3 d	-	-	0.0019 ± 7%	-	0.0019
^{33}P	25.4 d	-	-	0.0023 ± 6%	-	0.0023
^{35}S	87.44 d	-	-	0.00066 ± 3%	-	0.00066
^{36}Cl	3.01×10^{5} y	-	-	0.015 ± 4%	-	0.015
^{37}Ar	35.02 d	-	-	0.027 ± 3%	-	0.027
^{39}Ar	269 y	-	-	0.013 ± 3%	-	0.013
^{41}Ca	1.03×10^{5} y	-	-	0.19 ± 2%	-	0.19
^{45}Ca	163 d	-	0.0065 ± 54%	0.007 ± 2%	0.006	0.007
^{46}Sc	83.8 d	0.0044 ± 9%	-	0.00015 ± 7%	0.0005	0.0044
^{44}Ti	47.3 y	-	-	0.00002 ± 17%	-	0.00002
^{48}V	24.0 d	0.00053 ± 12%	-	0.00057 ± 9%	-	0.00053
^{49}V	330 d	-	-	0.0012 ± 6%	-	0.0011[2]
^{51}Cr	27.7 d	0.0036 ± 6%	-	0.003 ± 9%	-	0.0036
^{52}Mn	5.59 d	0.00086 ± 4%	-	0.00065 ± 7%	-	0.00086
^{54}Mn	313 d	0.0045 ± 3%	-	0.007 ± 8%	0.004	0.0045
^{55}Fe	2.70 y	-	0.0146 ± 48%	0.023 ± 8%	-	0.023
^{59}Fe	44.5 d	0.0013 ± 19%	0.0008 ± 53%	0.0007 ± 9%	-	0.0013
^{55}Co	78.8 d	0.00006 ± 7%	-	0.00007 ± 9%	-	0.00006
^{57}Co	271 d	0.000057 ± 5%	-	0.00002 ± 12%	-	0.00006
^{58}Co	70.8 d	0.000052 ± 2%	-	0.00003 ± 10%	-	0.00005
^{60}Co	5.27 y	0.0088 ± 20%	0.0034 ± 58%	0.0025 ± 11%	0.003	0.009
^{63}Ni	96 y	-	-	0.00017 ± 19%	-	0.00017
^{65}Zn	244 d	0.00037 ± 20%	-	-	-	0.0004
^{86}Rb	19 d	0.0015 ± 14%	-	-	-	0.0015
^{134}Cs	2.06 y	0.0031 ± 18%	-	-	-	0.003
^{131}Ba	11.8 d	0.000075 ± 7%	-	-	-	0.00008
^{133}Ba	10.7 y	-	-	-	-	0.00008[2]
^{141}Ce	32.5 d	0.000098 ± 18%	-	-	-	0.0001
^{152}Eu	13.3 y	0.00796 ± 15%	0.0045 ± 66%	-	0.008	0.008
^{154}Eu	8.8 y	0.00063 ± 32%	-	-	0.0006	0.0006
^{160}Tb	72.3 d	0.000214 ± 16%	-	-	-	0.0002
^{181}Hf	42.0 d	0.000046 ± 18%	-	-	-	0.00005
^{182}Ta	115 d	0.00038 ± 17%	-	-	-	0.0004
^{233}Pa	27.0 d	0.00053 ± 19%	-	-	-	0.0005

[2] See text in chapter 3.7

Chapter 4

Simulations

4.1 NGS-Simulations

The following paragraphs summarize a few aspects of the calculations which were of particular importance to the study discussed in this work. The simulation of all components of the particle cascade from 400 GeV to the energy of thermal neutrons was based on the most recent version of the FLUKA Monte-Carlo particle shower code, see references [Fas97, Fer97] and references therein.

Co-ordinate System:

The geometry is described, as for the molasse calculation, in a right-handed orthogonal system with x as the vertical axis, y as the axis pointing to the right of the receding proton beam and z as the direction of the proton beam. The beam axis is centered on the origin of the xy-plane. The z origin is at the focal plane of the proton beam within the target.

Source Particles:

The point of entry of the 400 GeV protons into the system was taken to be 5 cm in front of the upstream face of the target where the beam was assumed to have a divergence of 0.236 mradians (FWHM) and a spot size of 0.59 mm (FWHM) in both the horizontal and vertical planes.

Material Assignments:

The chemical composition of the molasse was taken from a chemical analysis report, see Table 3.3. Corresponding to this analysis, the density of the molasse is 2.4 g/cm^3.

The shotcrete and the concrete were assumed to have the same density, namely, 2.35 g/cm^3 and to have the following chemical composition (the values in brackets give the corresponding mass fractions): oxygen (50.0%), silicon (20.0%), calcium (20.0%), aluminum (3.0%), carbon (3.0%), iron (1.4%), potassium (1.0%), sodium (1.0%) and hydrogen (0.6%). These values are based on types of concrete previously used at CERN.

The iron shielding, except the iron tube in the decay tunnel, was taken to be cast iron with a density of 7.2 g/cm^3, and assumed to contain 5% of carbon. The decay tube was assumed to be of pure iron, with a density of 7.88 g/cm^3.

Pure marble is composed of 99% [Yam80] calcium carbonate $CaCO_3$ which, therefore, leads to the assumption that marble consists of 12% of carbon, 40% of calcium and 48% of oxygen (the values give the corresponding mass fractions) with a density of 2.7 g/cm^3.

All regions inside the excavations, except the target box, the helium tanks and the decay tunnel, were filled with air at S.T.P. The target box and the two helium tanks contained helium at S.T.P. and the decay tube air at 2 hPa.

Particle Energy Thresholds:

For the determination of the star densities in the different regions, the lower thresholds for particle transport were set to 50 MeV for all hadrons. Neutral pions, electrons, photons were not transported in the simulations as they do not significantly contribute to the production of radioactive nuclei.

For the track-length calculations in the air and helium volumes, the lower thresholds for particle transport were set to 10 MeV for all hadrons except neutrons which were followed down to thermal energies. The same particle thresholds were also used for the calculations of the residual nuclei distributions.

Biasing:

The calculations described in this thesis were based on FLUKA in its analogue mode except for thermal neutrons where the survival probability was adjusted to avoid undue time being wasted on tracking them. Significant use of decay biasing was only made for the calculation of the neutrino fluence at the Gran Sasso laboratory with the effect that the statistical accuracy of the results was dramatically enhanced.

Scoring:

The spatial distribution of the number of stars was recorded in the form of star density distributions in cylindrical and Cartesian binning in different parts of the geometry and as the total numbers of stars occurring in the different regions. Separate accounts were kept for neutrons, protons, and charged pions; other hadrons were included in an "all-hadron" star counter.

Hadron track-lengths as a function of particle type and energy were scored by summing particle track-lengths in various parts of the target cavern. Spectra were scored on a logarithmic basis in energy (ten energy intervals per decade in energy above 50 MeV and according to the FLUKA multi-group energy structure below this energy).

All the quantities scored were normalized to one incident beam proton.

4.2 From NGS-98 to NGS-99

The layout of NGS-98 and its alterations which were required for the new concept of NGS-99 in order not to exceed the NGS-98 radiation values will be studied in detail in the following section.

The original design of the NGS was established because it provided a wide range of possible beam variants within the established civil engineering constrains. Furthermore, the facility should produce a high-energy wide-band neutrino beam whereby most of the design was based on experience from previous beams at the WANF. Therefore, the conceptual design of the shielding around the target, the collimators and pulsed current of the focussing devices were applied in the same way. The short-baseline facility which might be built underground near the Geneva airport also had a significant influence on the design.

As the project developed, it turned out that significant improvements in the neutrino beam could be achieved, especially in the optimization of a long-baseline ν_τ appearance experiment, by a revised beam optics layout which maximizes the secondary beam acceptance in the desired momentum range.

Consequently, the best position of the horn is as close as possible to the target, therefore, the horn was positioned instead of 7.85 m, now only 1.7 m away from the target focal point. Hence, COLL.1 and COLL.2 had to be removed. Besides, the new location of the reflector is now 43.35 m instead of 80.35 m away from the target. As a result, the helium tubes had to be adapted.

The hadron fluence of protons, charged pions and neutrons with an energy greater than 50 MeV in the target cavern at beam height, is given for the NGS-98 in Figure 4.1 and for the layout with shielding only around the target in Figure 4.2. It can be seen that the shielding around COLL.2 significantly reduced the hadron fluence around the collimator. Furthermore, COLL.3, the iron shielding block around the first helium pipe prevents high-energy particles from hitting the back wall of the target cavern. Note that in Figure 4.2 (no shielding) the hadron fluence increases by about a factor of three. The horn and the reflector de-focus all negative charged particles, and therefore, it is obvious that a shielding around these devices would be advantageous. This fact can be seen in Figures 4.3 – 4.6 which show the hadron fluence as a radius dependent plot along the beam line for 4 different energy-thresholds.

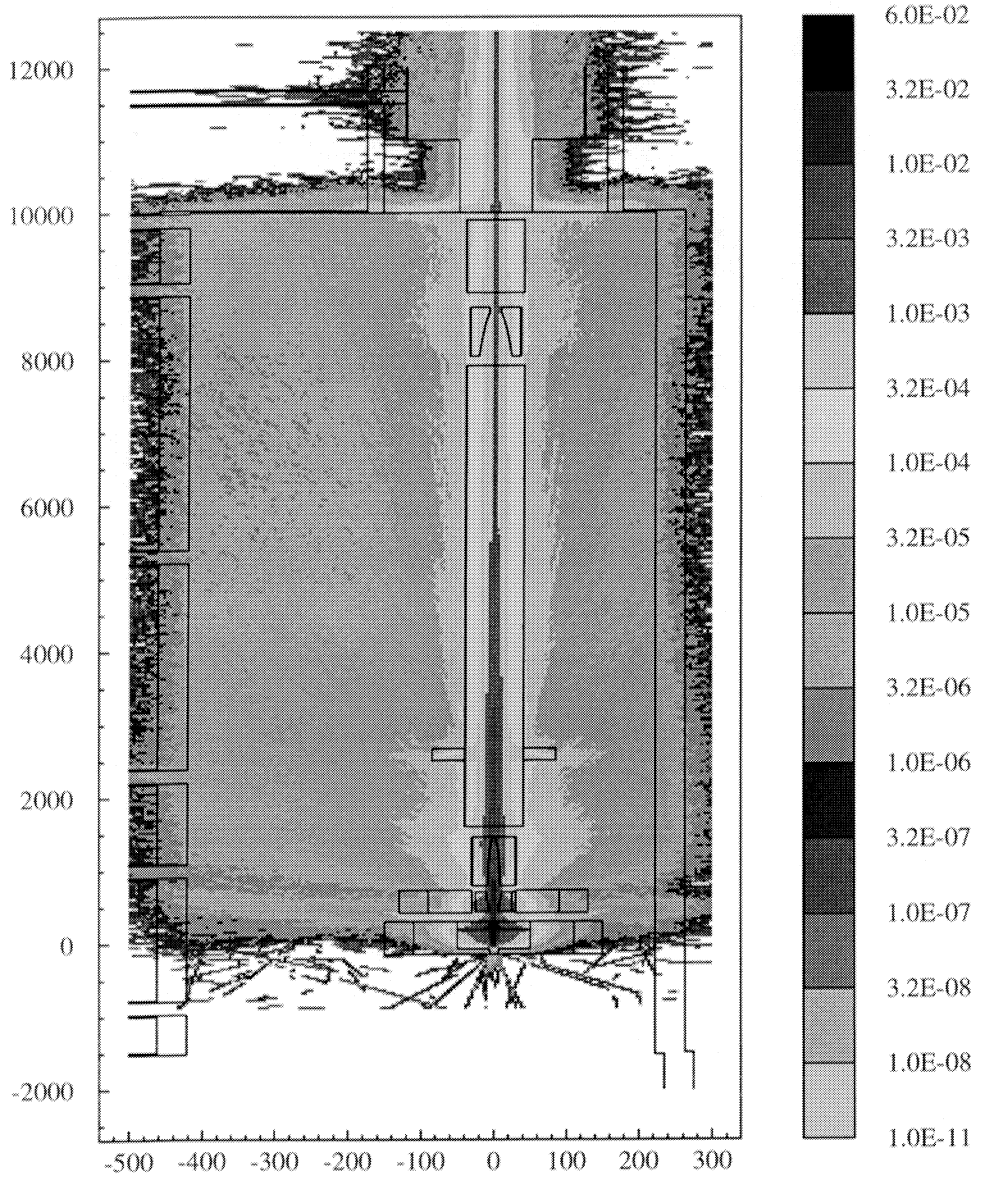

Figure 4.1: *Hadron fluence with energies above 50 MeV (per cm^2 and per primary proton) in the target cavern of NGS-98. All other units are in cm.*

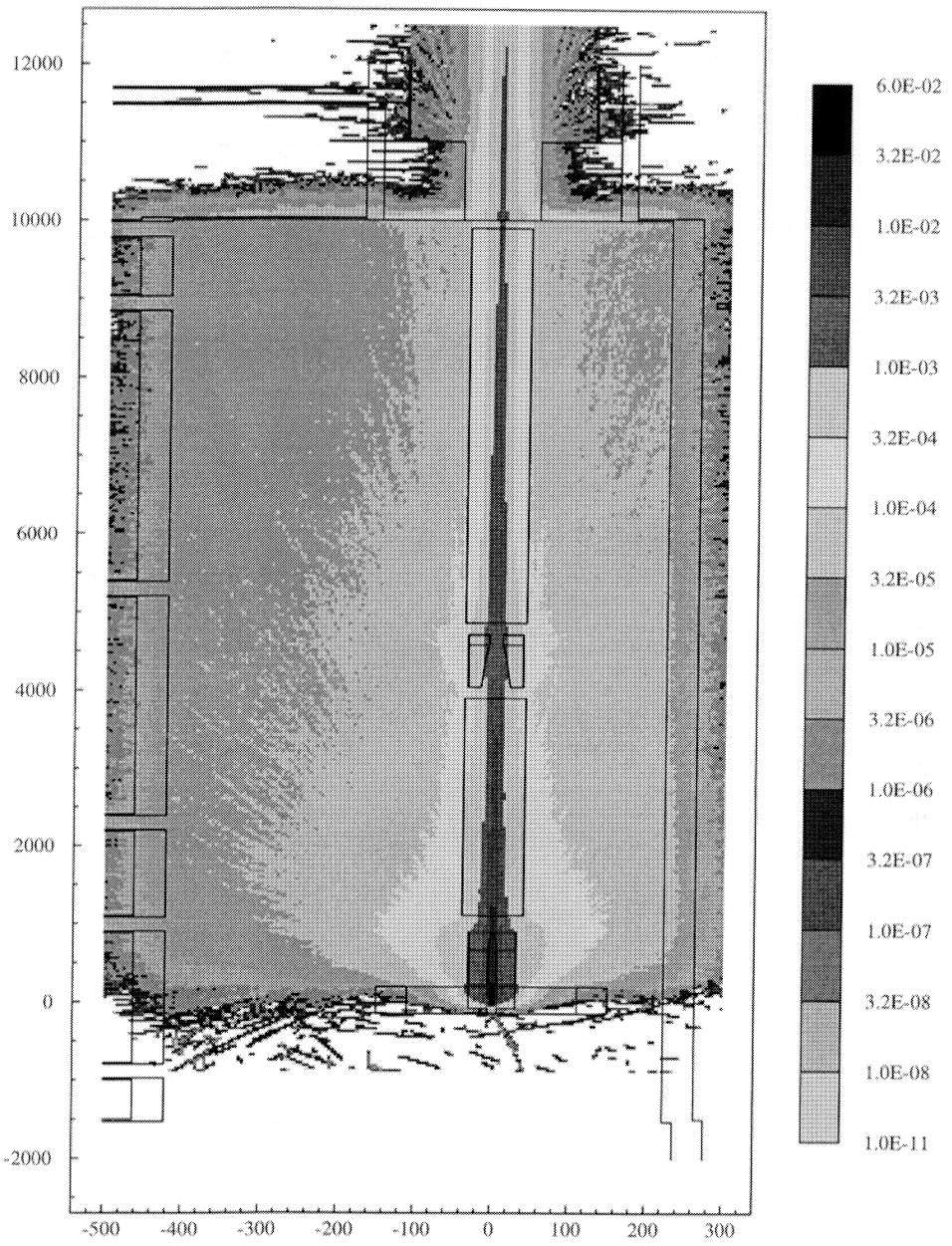

Figure 4.2: *Hadron fluence with energies above 50 MeV (per cm^2 and per primary proton) in the target cavern without shielding after the target. All other units are in cm.*

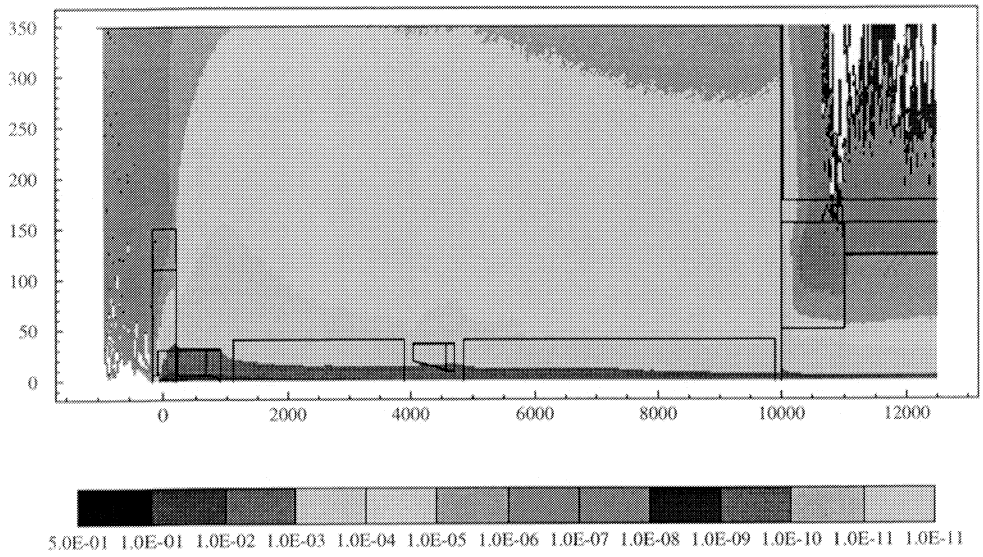

Figure 4.3: *Hadron fluence (E > 50 MeV) in the target cavern along the beam line (per cm^2 and per primary proton). All other units are in cm.*

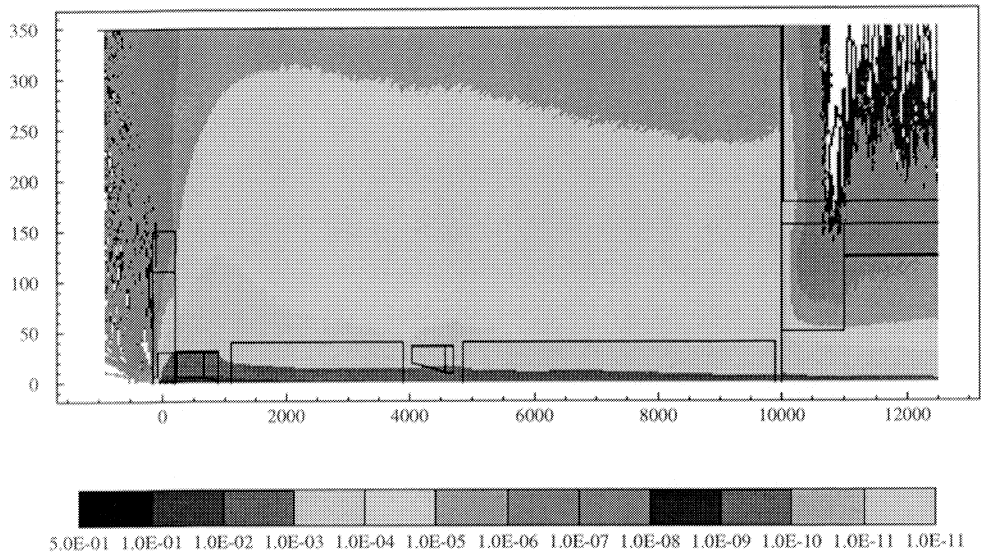

Figure 4.4: *Hadron fluence (E > 500 MeV) in the target cavern along the beam line (per cm^2 and per primary proton). All other units are in cm.*

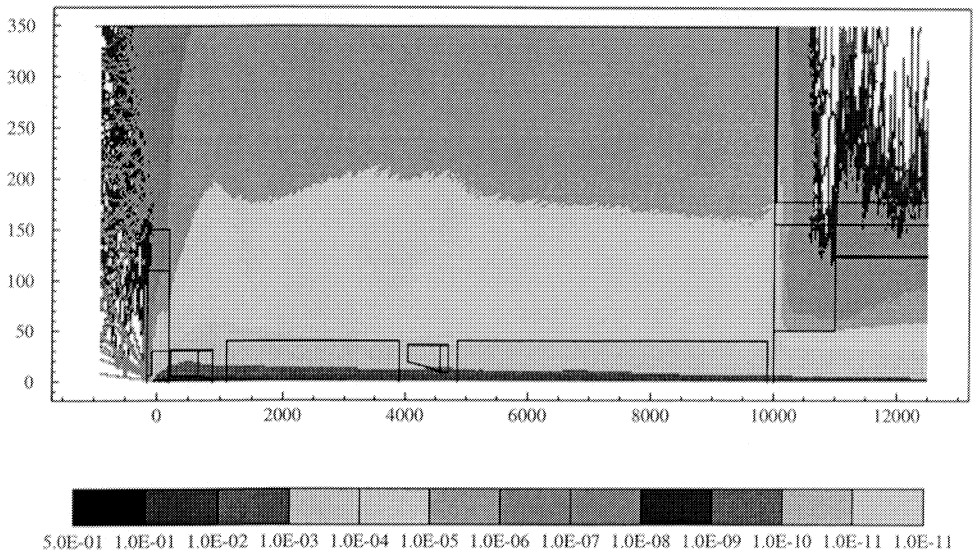

Figure 4.5: *Hadron fluence (E > 5 GeV) in the target cavern along the beam line (per cm^2 and per primary proton). All other units are in cm.*

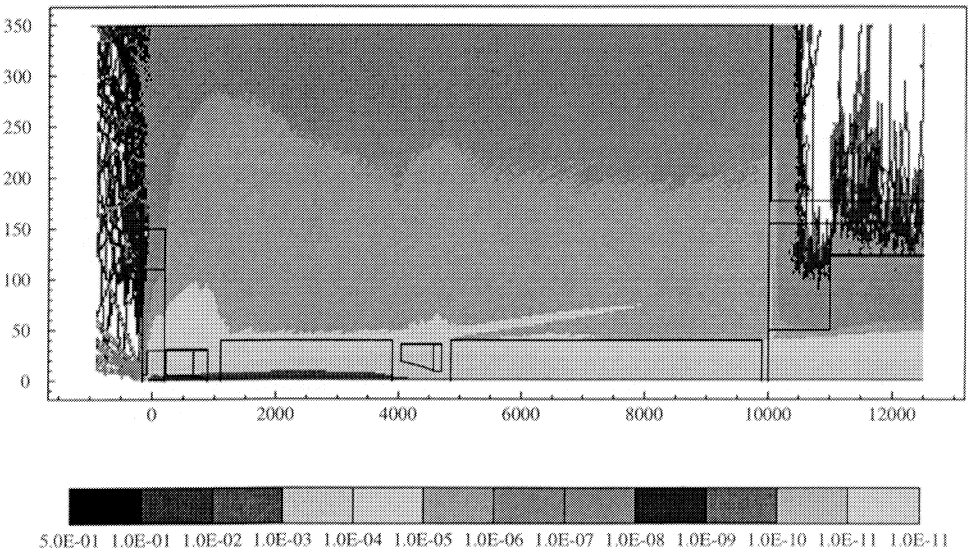

Figure 4.6: *Hadron fluence (E > 50 GeV) in the target cavern along the beam line (per cm^2 and per primary proton). All other units are in cm.*

The following paragraphs describe in greater detail results of various shielding configurations, summarizing the number of stars in the concrete and molasse around the target chamber. This data provides an impression of the expected activity induced in these locations. In addition to the absolute numbers of stars the relative value compared to the NGS-98 values are also listed. From Figure 4.7 to Figure 4.15 a horizontal cross-sectional view at beam height is shown. Note that the picture of the layout of NGS-98 is given in Figure 4.7. It is quite obvious that the removal of COLL.1, as well as, COLL.2, see Figure 4.8, would increase the number of stars.

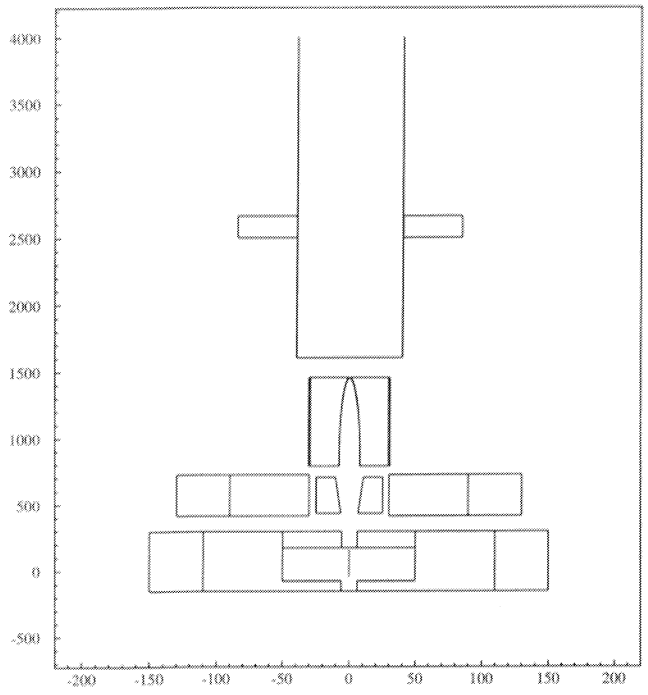

Stars in	
Concrete	Molasse
70	17
100%	100%

Figure 4.7: *Sectional view of the NGS-98.*

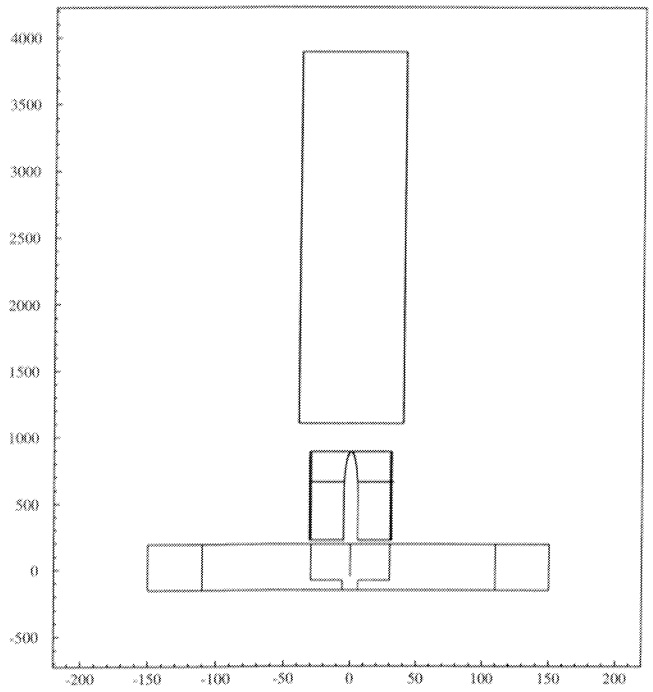

Stars in	
Concrete	Molasse
244	54
349%	318%

Figure 4.8: *No Shielding.*

The first attempt to establish a new NGS-99 layout was simply achieved by putting a large iron collimator with a dimension of 120 × 120 cm^2, an opening of 40 × 40 cm^2, and a total length of 10 m, around the first He^- pipe. It starts 16 m away from the focus point. A sectional view is represented in Figure 4.9. This large shielding block already reduces the number of stars by about 40% but this is still two times higher than in the NGS-98 design.

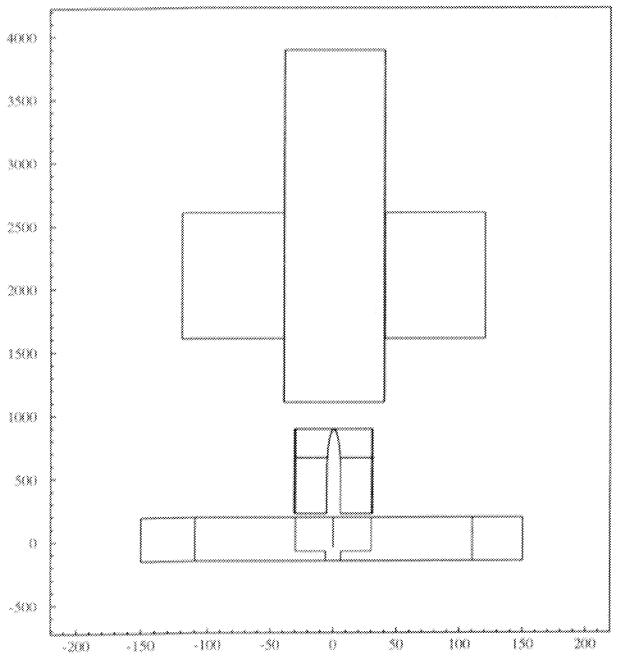

Stars in	
Concrete	Molasse
150	37
214%	217%

Figure 4.9: *Shielding 1.*

From Figure 4.3 to Figure 4.6 it can easily be seen that an additional shielding around the He pipe would also reduce the star production. Therefore, such an additional iron shielding with a thickness of 30 cm and a length of 14 m around the first He pipe was applied. The initial iron collimator of the He pipe was preserved in its dimensions; only its length was reduced by 6 m. This combination provided an additional star reduction of 12%, see Figure 4.10.

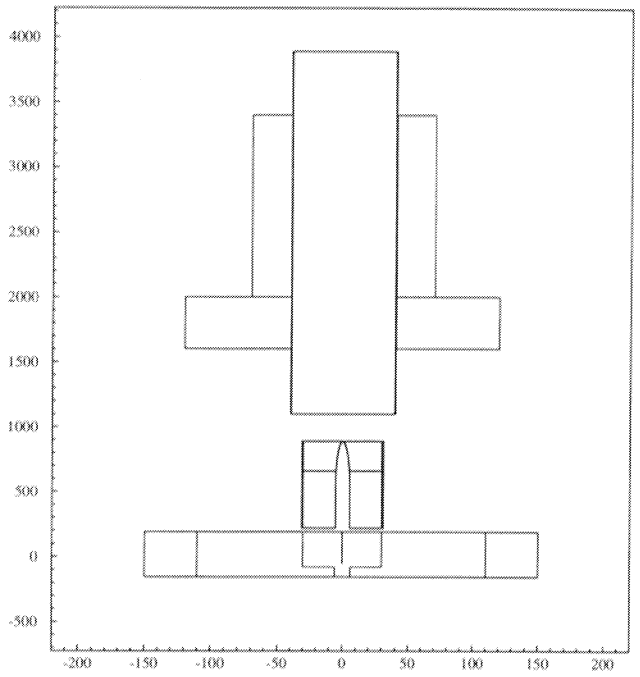

Stars in	
Concrete	Molasse
132	31
189%	189%

Figure 4.10: *Shielding 2.*

Another important issue concerning the new layout are provisions for direct access to the focussing devices which is essential for maintenance work. Therefore, a closed shielding around the horn or the reflector should not be established. A third possibility, namely, an iron shielding which is around the first 12 m of the pipe with a thickness of 20 cm which starts exactly 50 cm after the beginning of the pipe and which gives free access to the horn was simulated. To further decrease the production of stars, an additional iron block, 4 m in length with a cross section of 85 × 85 cm^2, was established directly after the first iron shielding around the He pipe, see Figure 4.11.

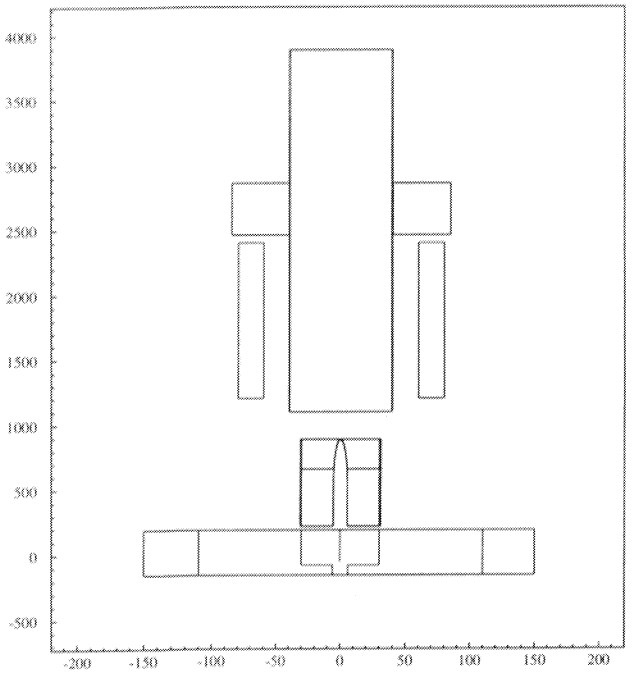

Stars in	
Concrete	Molasse
163	41
233%	241%

Figure 4.11: *Shielding 3.*

On the other hand, a complete shielding of 40 cm thickness and 7 m length around the horn in combination with the shielding of Figure 4.11 would bring the number of stars per primary proton down to 85 in the concrete and to 23 in the molasse, see Figure 4.12. This was still 20% higher than in the NGS-98 design but, however, it showed the lowest star production so far. The iron shielding around the horn reduces the star production in the concrete by nearly 100%. It is noteworthy that the gaps between the different shielding components are foreseen for the electrical strip lines to the horn.

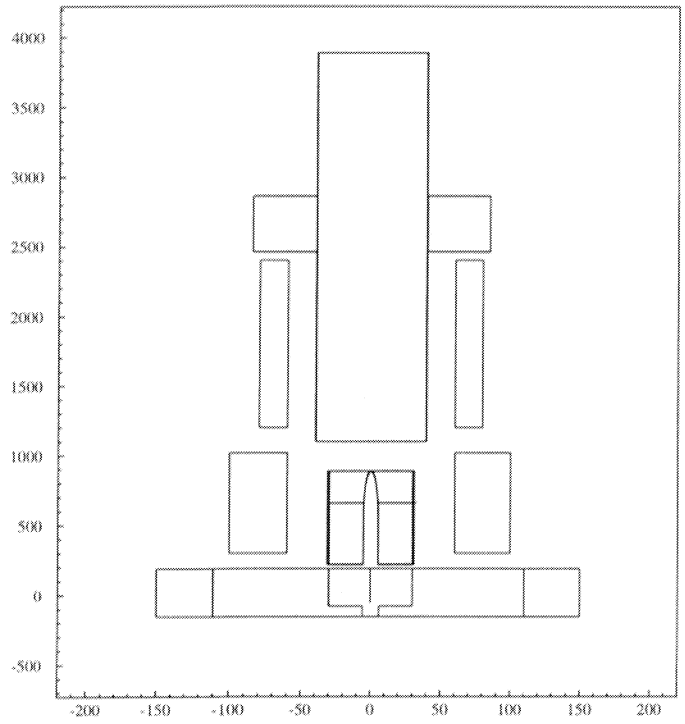

Stars in	
Concrete	Molasse
90	25
129%	147%

Figure 4.12: *Shielding 4.*

Alsmitter and Borish [Als73] pointed out that iron has a major deficiency as a shield for fast neutrons. Containing no light elements, as i.e., hydrogen, the primary attenuation mechanism for fast neutrinos is by inelastic scattering from the iron nuclei. At energies below the first excited state which is 847 keV for ^{56}Fe [Iso] inelastic scattering becomes impossible and elastic scattering becomes the only removal process. Thus, pure iron is rather ineffective in attenuation neutrons with an energy below 847 keV. Therefore, an additional concrete shielding of 30 cm thickness around the second iron shielding (based on Figure 4.10) of the first pipe was installed. As mentioned above the access to the focusing devices is essential and, hence, detailed FLUKA calculations had to be carried out in order to check the possibility of leaving the horn without shielding. In Figure 4.13 the design of the target cavern is given wherein the right hand side of the horn is shielded by a marble (20 cm thick) and a concrete wall (30 cm thick) with a height of 3.2 m and a length of 10.3 m. It can easily be seen that the number of stars in the concrete is still 27% higher than in NGS-98 but by shielding also the left hand side of the horn, see Figure 4.14, with a modular shielding concept of marble together with concrete the number of stars will almost reach the NGS-98 limits.

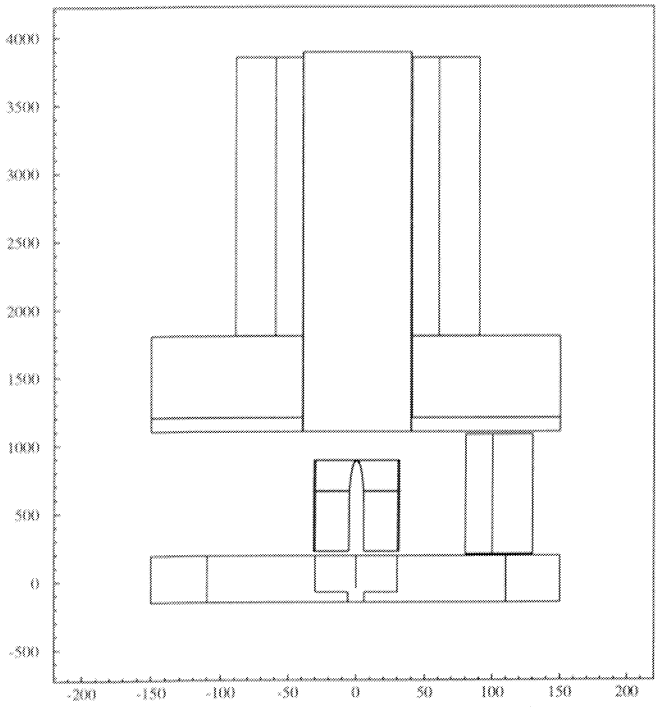

Stars in	
Concrete	Molasse
89	24
127%	141%

Figure 4.13: *Shielding 5.*

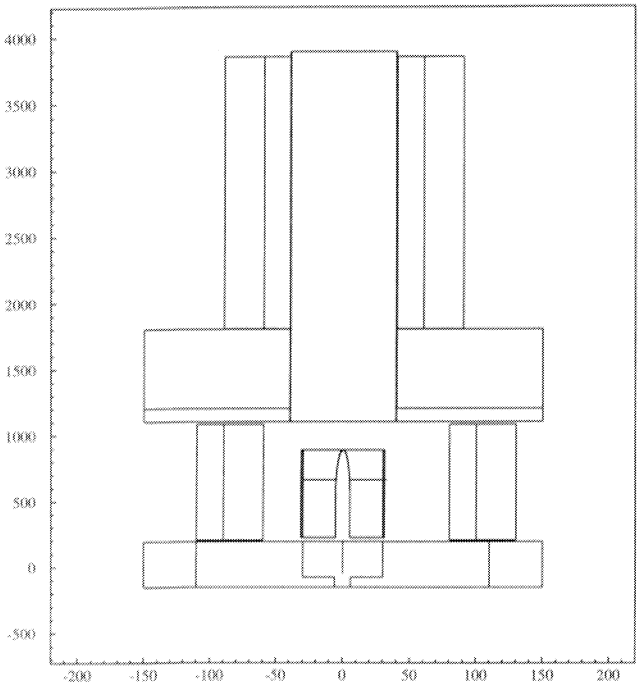

Stars in	
Concrete	Molasse
75	20
107%	118%

Figure 4.14: *Shielding 6.*

An additional shielding of 30 cm iron and 30 cm of concrete around the second He pipe would evoke values below those of NGS-98, see Figure 4.15. The shielding-wall at the left side of the horn will be movable and can, therefore, give easy access to the horn whenever it is required.

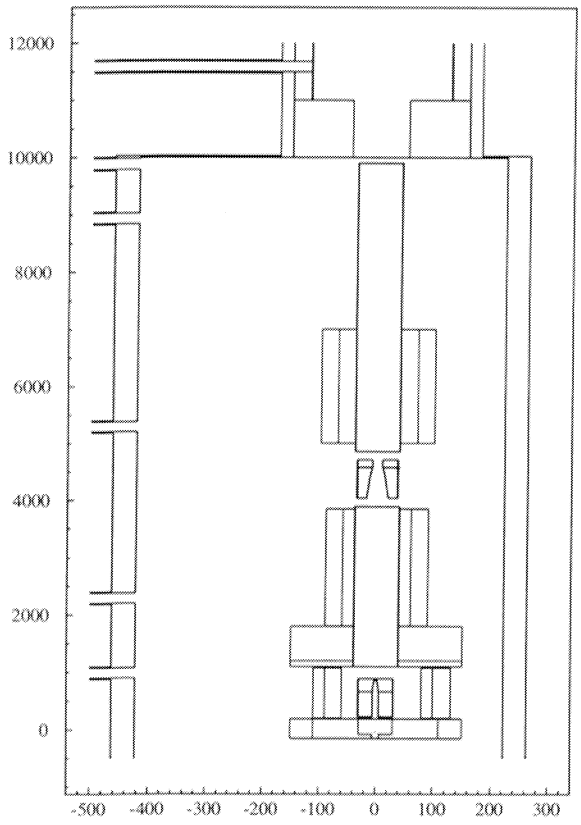

Stars in	
Concrete	Molasse
59	16
84%	94%

Figure 4.15: *Shielding 7.*

During these design studies it was decided to increase the current of the horn and the reflector from 120 kA to 150 kA. They are now designed to focus pions and kaons of 35 GeV and 50 GeV, respectively. Additionally, the radius of the reflector changed from 40 cm to 60 cm. The diameter of the rod increased from 3 mm to 4 mm which reduces spurious background from residual protons interacting later on in the beam line. Besides, the target consists of 13 rods of 100 mm length separated by gaps of 55 mm. The total length is similar to the old target with 11 rods and 100 mm gaps. The alterations of the horn and the reflector were re-examined by the CERN Beam optics groups, whereby the nominal acceptance for pions and kaons between 20 and 50 GeV was increased by 50% [NGS99]. Furthermore, COLL.4 of the 1998 reference beam, which was used to cover the first 10 m inside the decay pipe, was moved into the target cavern. The length of this collimator was shortened to 5 m and the cross-section had to be increased from 1 m to 1.2 m so that it has the same diameter as the reflector.

The latest layout of NGS-99 is presented in a three-dimensional Autocad drawing, as shown in Figure 4.16. This drawing is deducted from the information on geometry and material used in the FLUKA calculations. The shielding at the side of the horn was extended by an additional concrete shielding-wall with a total thickness of 30 cm. Marble has the advantage that radiation levels from induced radioactivity are much lower than those in other shielding materials [Hoe75] such as iron or normal concrete, therefore, it was used around the target station as the innermost part of the modular shielding of the sides of the horn and around the start of the first helium pipe. Details of the target/horn region are shown in Figure 4.17.

Finally, the hadron fluence of the NGS-99 design is illustrated in Figure 4.18 and in comparison with the NGS-98 it can be concluded that this fluence is lower.

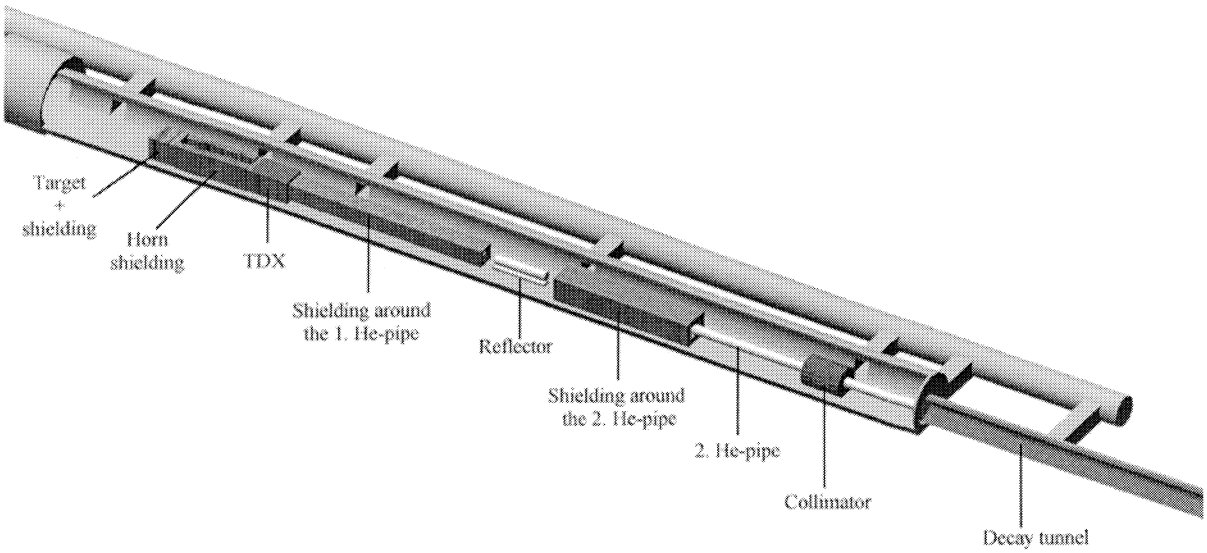

Figure 4.16: *View into the NGS-99 target chamber with beam components and shielding. The service gallery parallel to the target chamber and the various connecting alcoves are also shown.*

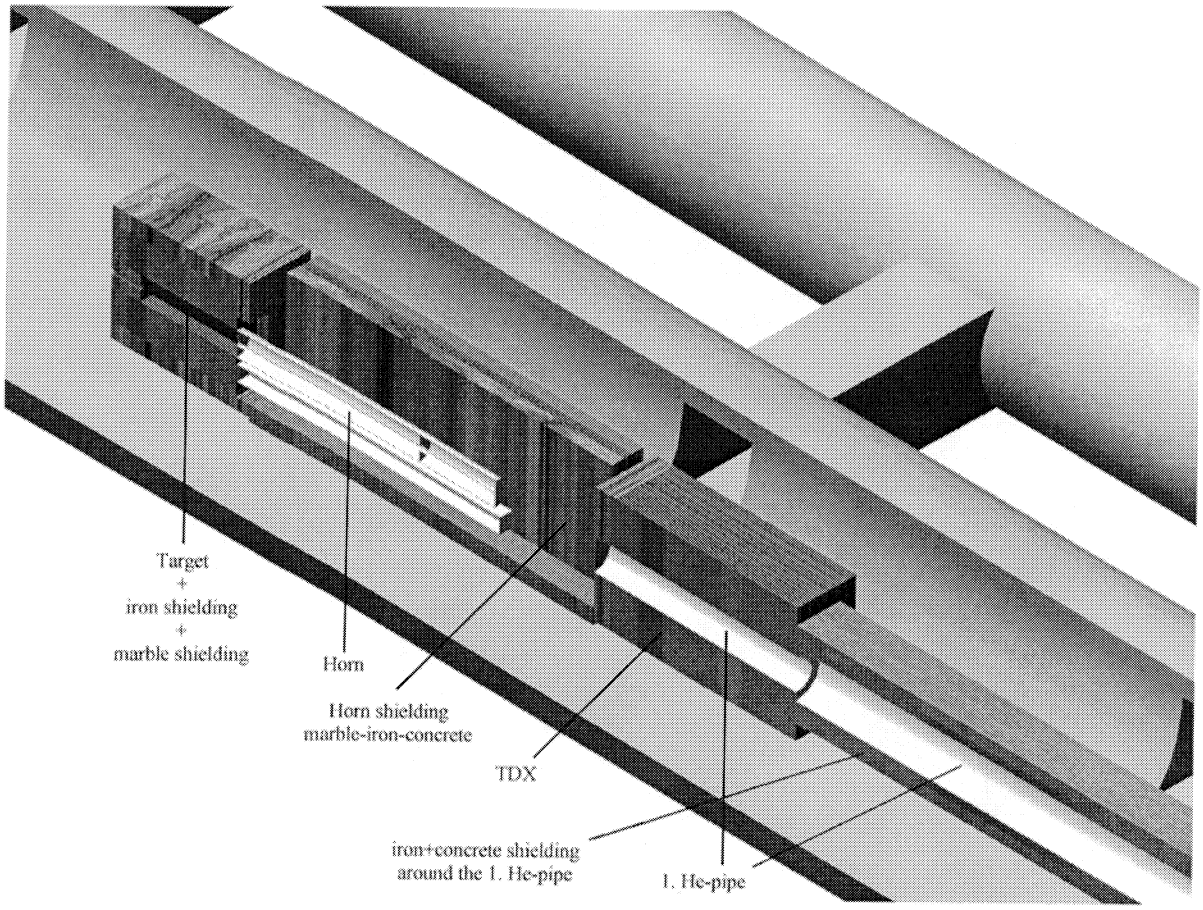

Figure 4.17: *Details of the target and horn region of NGS-99. One shielding wall on the side of the horn is removed for better insight.*

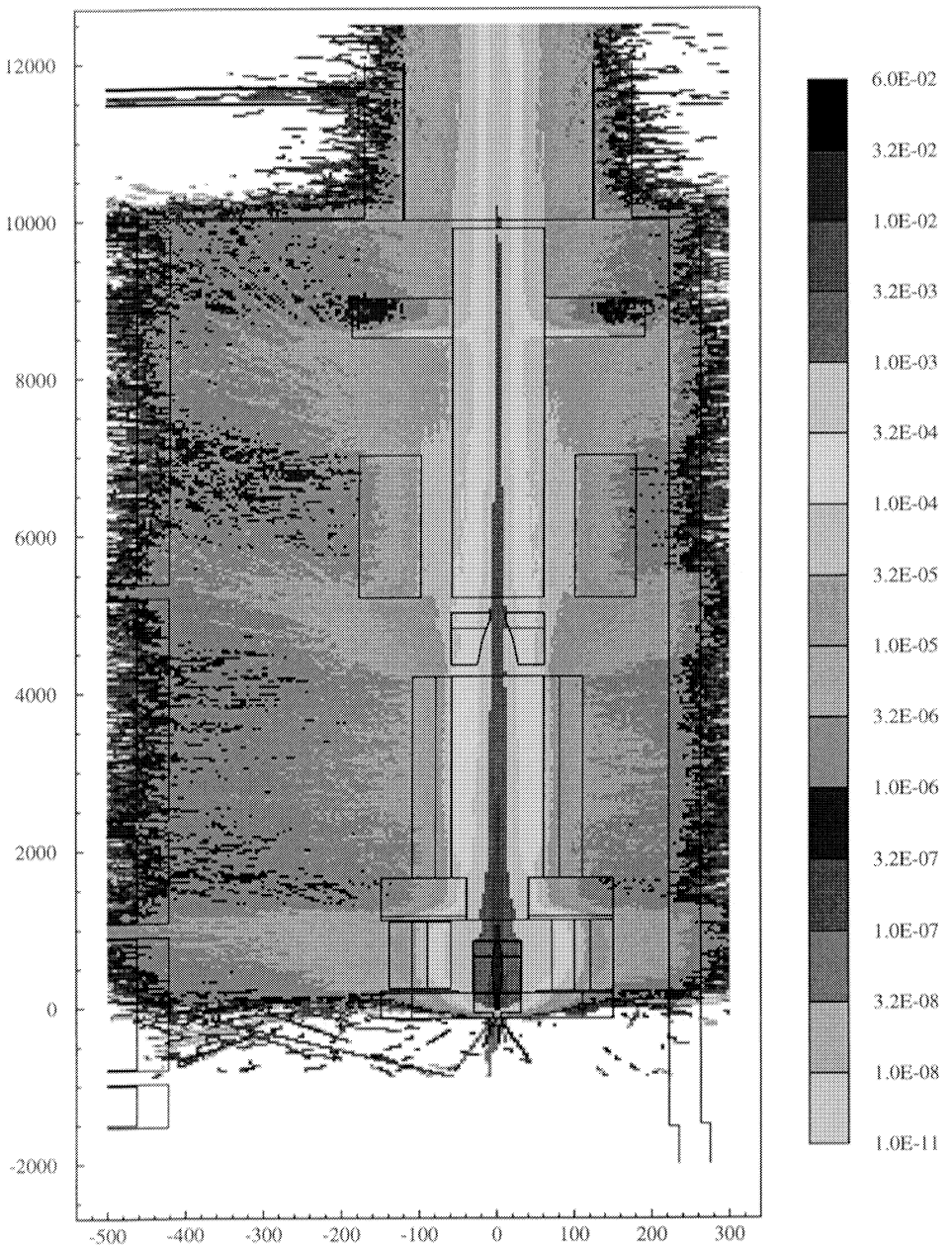

Figure 4.18: *Hadron fluence with energies above 50 MeV (per cm^2 and per primary proton) in the target cavern of NGS-99. All other units are in cm.*

Chapter 5

Radiological Parameters

The most important items of the present proposals for a neutrino beam to Gran Sasso from a radiological viewpoint are the target chamber, the decay tunnel and the hadron stopper. The following chapter presents estimates of the total radioactivity induced in the structure and its surroundings and the magnitude of any release to the environment via air or water pathways.

5.1 Radioactivity in the Molasse-Rock

The radioactivity induced in the molasse-rock outside the cavern, the decay tunnel, and the hadron stopper is calculated from the number of stars in these regions. Results concerning the star production are given in Table 5.1 for NGS-98 and in Table 5.2 for NGS-99 with respect to the different locations. The errors of these numbers are always less than 2% and it should be noted that more than 80% of all stars are due to neutrons. The contributions from regions upstream the target chamber and around the hadron stopper are unimportant.

Table 5.1: *Number of stars produced per proton in the molasse of NGS-98.*

NGS-98	**Stars Produced**			
Location	By protons	by neutrons	by charged pions	all hadrons
Upstream of target cavern	0	2.5×10^{-4}	0	2.5×10^{-4}
Around target cavern	1.0	14.5	1.5	16
Around the decay tunnel	2.1	22.1	4.8	29
Around the hadron stopper	2.5×10^{-4}	9.25×10^{-3}	0	0.01
Total	**3.1**	**36.6**	**6.3**	**45.0**

Table 5.2: *Number of stars produced per proton in the molasse of NGS-99.*

NGS-99	Stars Produced			
Location	By protons	by neutrons	by charged pions	all hadrons
Upstream of target cavern	0	0	0	0
Around target cavern	0.5	12.0	0.6	13.1
Around the decay tunnel	1.0	21.6	1.4	24.0
Around the hadron stopper	0	0.01	0	0.01
Total	**1.5**	**33.6**	**2.0**	**37.1**

For the calculation of radioactivity in the molasse-rock the conversion factors determined in Table 3.9 are applied. The production rate of isotope j, X_j, can be expressed in terms of

$$X_j = p\, K_j\, n_{star}, \tag{5.1}$$

where p is the proton intensity on the target per second, K_j is the production of the isotope j per star and n_{star} is the number of stars per proton. The activity of an isotope j, with a decay constant λ_j after an irradiation time t_{irr} and a decay time t_d is then given by

$$A_j(t) = X_j[1 - \exp(-\lambda_j\, t_{irr})]\exp(-\lambda\, t_d)\,. \tag{5.2}$$

The activity after 10 years of operation can be calculated by summing the activity produced in each operation period (200 days per year) and multiplying it by the appropriate decay factor. The results of NGS-98 and NGS-99 are listed in Table 5.3. A comparison of the activities in both cases shows that the production of radioactivity is reduced by nearly 20 % in the new configuration. This reduction is caused by an additional shielding in the target cavern.

Table 5.3: *Activity of radioactive isotopes in molasse after 10 years of operation assuming 5.0×10^{19} protons on target per year with an operating period of 200 days.*

Radionuclide	Half-life	*NGS-98*	*NGS-99*
^{3}H	12.4 y	9.31×10^{11}	7.68×10^{11}
^{7}Be	53.3 d	1.46×10^{12}	1.20×10^{12}
^{10}Be	1.60×10^{6} y	1.86×10^{6}	1.53×10^{6}
^{14}C	5730 y	1.38×10^{9}	1.14×10^{9}
^{22}Na	2.60 y	5.91×10^{11}	4.87×10^{11}
^{26}Al	7.16×10^{5} y	1.04×10^{7}	8.6×10^{6}
^{32}P	14.3 d	2.47×10^{11}	2.04×10^{11}
^{33}P	25.4 d	2.98×10^{11}	2.46×10^{11}
^{35}S	87.4 d	7.24×10^{10}	5.97×10^{10}
^{36}Cl	3.01×10^{5} y	2.47×10^{7}	2.03×10^{7}
^{37}Ar	35.0 d	3.45×10^{12}	2.85×10^{12}
^{39}Ar	269 y	2.36×10^{10}	1.95×10^{10}
^{41}Ca	1.03×10^{5} y	9.12×10^{8}	7.52×10^{8}
^{45}Ca	163 d	6.62×10^{11}	5.46×10^{11}
^{46}Sc	83.8 d	4.87×10^{11}	4.02×10^{11}
^{44}Ti	47.3 y	1.95×10^{8}	1.61×10^{8}
^{48}V	24.0 d	6.88×10^{10}	5.67×10^{10}
^{49}V	330 d	9.17×10^{10}	7.56×10^{10}
^{51}Cr	27.7 d	4.66×10^{11}	3.84×10^{11}
^{52}Mn	5.59 d	1.12×10^{11}	9.23×10^{10}
^{54}Mn	313 d	3.78×10^{11}	3.12×10^{11}
^{55}Fe	2.70 y	1.60×10^{12}	1.32×10^{12}
^{59}Fe	44.5 d	1.62×10^{11}	1.34×10^{11}
^{56}Co	78.8 d	6.74×10^{9}	5.56×10^{9}
^{57}Co	217 d	5.15×10^{9}	4.25×10^{9}
^{58}Co	70.8 d	5.75×10^{9}	4.74×10^{9}
^{60}Co	5.27 y	4.84×10^{11}	3.99×10^{11}
^{63}Ni	96 y	8.46×10^{8}	6.98×10^{8}
^{65}Zn	244 d	3.50×10^{10}	2.88×10^{10}
^{86}Rb	19 d	1.95×10^{11}	1.61×10^{11}
^{134}Cs	2.06 y	5.92×10^{9}	4.88×10^{9}
^{131}Ba	11.8 d	3.91×10^{11}	3.22×10^{11}
^{133}Ba	10.7 y	2.76×10^{9}	2.28×10^{9}
^{141}Ce	32.5 d	1.28×10^{10}	1.06×10^{10}
^{152}Eu	13.3 y	2.34×10^{11}	1.93×10^{11}
^{154}Eu	8.8 y	2.38×10^{10}	1.96×10^{10}
^{160}Tb	72.3 d	2.29×10^{10}	1.89×10^{10}
^{181}Hf	42.0 d	6.28×10^{9}	5.18×10^{9}
^{182}Ta	115 d	4.10×10^{10}	3.38×10^{10}
^{233}Pa	27.0 d	6.47×10^{10}	5.34×10^{10}
Total		**1.26×10^{13}**	**1.04×10^{13}**

The significance of these activities can be estimated by comparing them to the natural radioactivity occurring in the molasse. In the construction of the underground installations associated with the target cavern, the decay tunnel, and the hadron-stopper approximately 35000 m^3 will have to be excavated. There are 0.455 Bq/g of naturally occurring gamma-emitting radionuclides in this molasse, see chapter 3, or a total activity of more than 3.8×10^{10} Bq. At the end of the ten-year operational period the new induced activity in the rock will be some 300 times higher than this, but Figure 5.1 which depicts the decay of the activity in the molasse as a function of time after the end of operation of the NGS-99 facility, indicates that the new activity will be less than the original activity after 75 years. Concurrently, taking only the radioactivity from γ-emitting isotopes into account, the level of natural activity will be reached after 33 years.

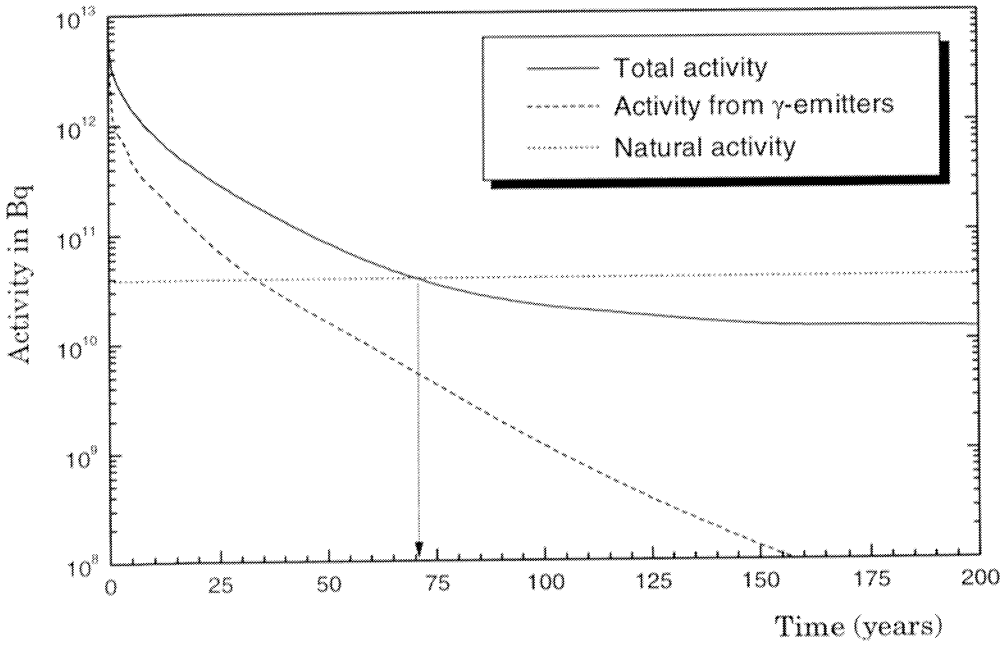

Figure 5.1: *Variation of total activity in the molasse for NGS-99 with time after shut-down of the neutrino facility.*

Among the different radionuclides produced in molasse there are only few which are dominant contributors. In Figure 5.2 the activity for three different time scales is shown. On the time scale up to 10 years, the most important radionuclides are ^{3}H, ^{55}Fe and ^{60}Co; on longer time scales (< 100 years), ^{3}H is still responsible for the major part of the molasse activity whereas in a times scale up to 1000 years ^{39}Ar and ^{14}C contribute mostly to the activity.

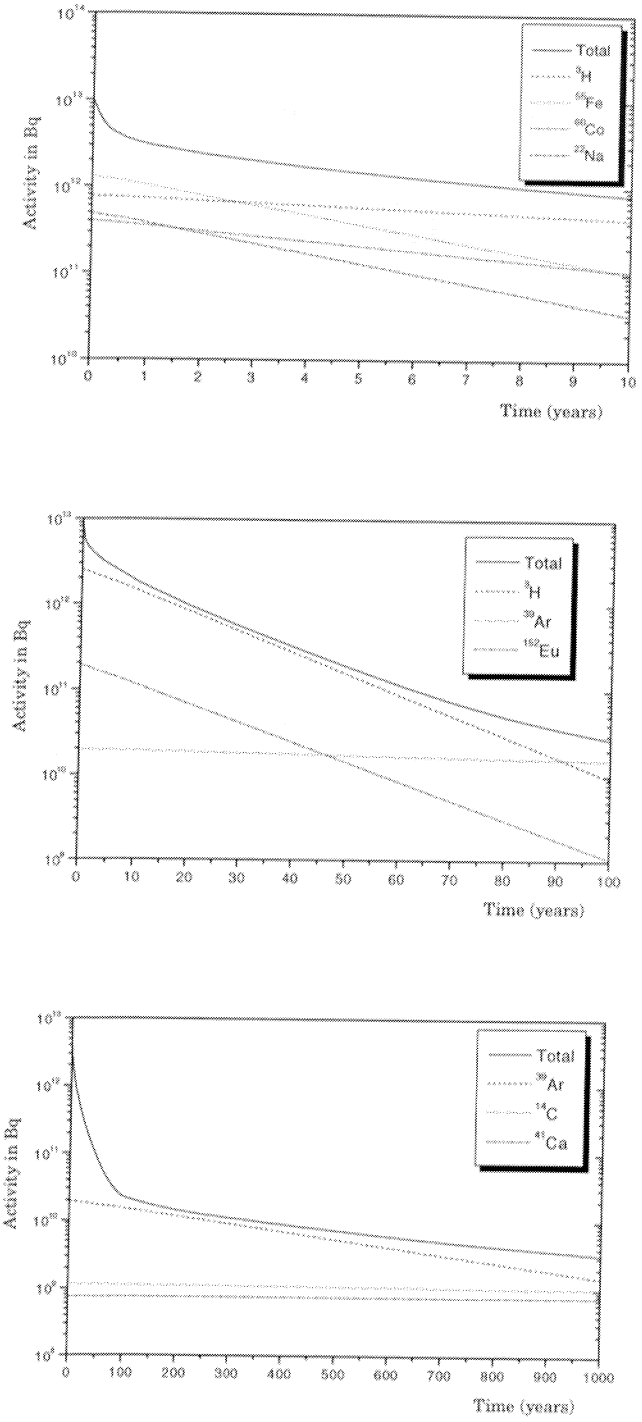

Figure 5.2: *The activity in molasse for NGS-99 as a function of time with the main contributors for 3 different time scales. The total activities include decays by γ, β and Electron capture.*

5.2 Radioactivity in the Concrete Walls

It is a well-known feature that the induced radioactivity in concrete, which accumulates with irradiation time, becomes a major source of radiation exposure to maintenance workers after accelerator operation for several years. Unfortunately, calculating radionuclide production in concrete is difficult because first, the exact composition of the concrete is rarely well known and second, the cross-sections of radionuclide production are not available for all of the elements contained in concrete. One way of determining the dominant radionuclides is to score isotope production in FLUKA simulations. The reliability of these results, assuming a particular concrete composition, depends on the quality and coverage of the physics models used in FLUKA. The number of stars in different concrete regions were calculated in order to determine a conversion factor between the number of inelastic nuclear interaction (stars) and the isotope production. Results are given in Table 5.4 for NGS-98 and in Table 5.5 for NGS-99.

Table 5.4: *Number of stars produced per proton in the concrete of NGS-98.*

NGS-98	**Stars Produced**			
Location	by protons	by neutrons	By charged pions	all hadrons
Upstream of target cavern	0	1.5×10^{-3}	0	1.5×10^{-3}
Around target cavern	7.4	40.4	18.8	66.7
Around the decay tunnel	5.7	37.8	14.6	58.1
Around the hadron stopper	3.0×10^{-3}	1.24×10^{-1}	1.0×10^{-3}	0.13
Total	**13.1**	**78.3**	**33.4**	**124.9**

Table 5.5: *Number of stars produced per proton in the concrete of NGS-99.*

NGS-99	**Stars Produced**			
Location	by protons	by neutrons	By charged pions	all hadrons
Upstream of target cavern	0	1.6×10^{-3}	0	1.6×10^{-3}
Around target cavern	3.2	27.6	7.2	38.3
Around the decay tunnel	9.0	56.1	21.8	88.3
Around the hadron stopper	2.0×10^{-2}	9.2×10^{-2}	2.0×10^{-2}	0.1
Total	**12.2**	**83.3**	**29.0**	**126.7**

Due to the additional shielding around the beam line in NGS-99 there are 43% less stars in the concrete of the target cavern. But, on the other hand, the number of stars around the decay tunnel increased by 52% because of the optimization of the horn and reflector and because of the two missing collimators after the target. Despite beam optimization, the number of stars around the hadron stopper are nearly unchanged because in the NGS-99 configuration 13 target rods are used instead of 11 and, consequently, the number of primary protons which hit the stopper without interacting with the target decreases. However, the total number of stars in the concrete is approximately the same in both cases.

In Table 5.6 the yields per star of the dominant radionuclides produced in the concrete walls are summarized referring to three values, namely, the production in the concrete of the target cavern, the production in the concrete of the decay tunnel, and the average value of the two locations.

The production of radioactivity in the concrete after 10 years of operation is given in Table 5.7. These results are based on the total number of stars produced in the concrete of NGS-98 and NGS-99 and, therefore, calculations of radioactivity in different regions can be carried out by using Table 5.4 (for NGS-98) and Table 5.5 (for NGS-99). It can easily be seen that the production of radioactivity in the concrete of the target cavern decreased by nearly 43% in NGS-99 whereas the activity in the decay tunnel rose by 52%.

Note that the activity produced in iron, foreseen as reinforcement of the tunnel structure, must be added to the calculated activity in the concrete of the target cavern, see section 5.6.

Table 5.6: *Production of radionuclides (half-live > 10h) per star in the concrete of the target cavern and the decay tunnel.*

Radionuclide	Half-life	*Target cavern*	*Decay tunnel*	*Average*
^{3}H	12.4 y	0.0292 ± 1.5%	0.0312 ± 0.4%	0.0302 ± 1.9%
^{7}Be	53.3 d	0.0087 ± 1.6%	0.0094 ± 0.3%	0.00905 ± 1.8%
^{10}Be	1.60×10^{6} y	0.0056 ± 1.0%	0.0059 ± 1.0%	0.00575 ± 2.0%
^{14}C	5730 y	0.0161 ± 0.9%	0.0157 ± 1.1%	0.0159 ± 2.0%
^{22}Na	2.60 y	0.0067 ± 1.2%	0.0072 ± 0.7%	0.00695 ± 1.9%
^{24}Na	15.0 h	0.0477 ± 0.7%	0.0254 ± 0.9%	0.0366 ± 1.5%
^{26}Al	7.16×10^{5} y	0.012 ± 1.4%	0.012 ± 0.7%	0.012 ± 2.1%
^{32}P	14.3 d	0.0029 ± 2.6%	0.0028 ± 0.9%	0.00285 ± 3.5%
^{33}P	25.4 d	0.0038 ± 3.5%	0.0040 ± 1.1%	0.0039 ± 4.5%
^{35}S	87.4 d	0.0011 ± 7.7%	0.0010 ± 2.9%	0.00105 ± 10.8%
^{36}Cl	3.01×10^{5} y	0.0195 ± 1.4%	0.0188 ± 1.1%	0.01915 ± 2.5%
^{37}Ar	35.0 d	0.0481 ± 0.5%	0.0485 ± 0.4%	0.0483 ± 0.9%
^{39}Ar	269 y	0.0109 ± 0.5%	0.0102 ± 0.6%	0.01055 ± 1.1%
^{42}Ar	33 y	0.00005 ± 14%	0.00005 ± 14%	0.00005 ± 28%
^{42}K	12.4 h	0.0112 ± 3.1%	0.0056 ± 2.4%	0.0084 ± 5.7%
^{43}K	22.3 h	0.0007 ± 4.6%	0.0007 ± 3.4%	0.0007 ± 8.0%
^{41}Ca	1.03×10^{5} y	0.7592 ± 0.6%	0.3825 ± 0.8%	0.5709 ± 1.3%
^{45}Ca	163 d	0.0357 ± 0.9%	0.0182 ± 1.2%	0.02695 ± 2.0%
^{47}Ca	4.54 d	0.0027 ± 2.7%	0.0015 ± 3.6%	0.0021 ± 6.0%
^{46}Sc	83.8 d	0.00003 ± 14.4%	0.00003 ± 22.0%	0.00003 ± 36.4%
^{47}Sc	3.35 d	0.00003 ± 34.8%	0.00004 ± 8.8%	0.000035 ± 39.9%
^{48}Sc	43.67 h	0.00002 ± 25.0%	0.00002 ± 25.0%	0.00002 ± 50.0%
^{44}Ti	47.3 y	0.00001 ± 25.0%	0.00001 ± 33.0%	0.00001 ± 58.0%
^{48}V	24.0 d	0.00024 ± 7.2%	0.00026 ± 6.1%	0.00025 ± 13.3%
^{49}V	330 d	0.00039 ± 1.0%	0.00042 ± 2.6%	0.000405 ± 3.7%
^{51}Cr	27.7 d	0.00080 ± 3.3%	0.00083 ± 4.2%	0.000815 ± 7.5%
^{52}Mn	5.59 d	0.00021 ± 2.7%	0.00023 ± 2.4%	0.00022 ± 5.1%
^{54}Mn	313 d	0.0018 ± 3.4%	0.0018 ± 1.9%	0.0018 ± 5.3%
^{55}Fe	2.70 y	0.0164 ± 1.4%	0.0097 ± 1.1%	0.01305 ± 2.6%
^{59}Fe	44.5 d	0.00038 ± 4.0%	0.00020 ± 9.6%	0.00029 ± 11.9%

Table 5.7: *Activity of radioactive isotopes in concrete after 10 years of operation assuming 5.0×10^{19} protons on target per year and an operational year of 200 days.*

Radionuclide	Half-life	*NGS-98*	*NGS-99*
^{3}H	12.4 y	2.60×10^{12}	2.64×10^{12}
^{7}Be	53.3 d	3.07×10^{12}	3.11×10^{12}
^{10}Be	1.60×10^{6} y	4.98×10^{6}	5.05×10^{6}
^{14}C	5730 y	3.81×10^{9}	3.86×10^{9}
^{22}Na	2.60 y	1.35×10^{12}	1.37×10^{12}
^{24}Na	15.0 h	1.32×10^{13}	1.34×10^{13}
^{26}Al	7.16×10^{5} y	2.31×10^{7}	2.34×10^{7}
^{32}P	14.3 d	1.04×10^{12}	1.06×10^{12}
^{33}P	25.4 d	1.40×10^{12}	1.42×10^{12}
^{35}S	87.4 d	3.34×10^{11}	3.39×10^{11}
^{36}Cl	3.01×10^{5} y	8.70×10^{7}	8.83×10^{7}
^{37}Ar	35.0 d	1.72×10^{13}	1.74×10^{13}
^{39}Ar	269 y	5.29×10^{10}	5.37×10^{10}
^{42}Ar	33 y	5.65×10^{8}	5.73×10^{8}
^{42}K	12.4 h	3.04×10^{12}	3.08×10^{12}
^{43}K	22.3 h	2.53×10^{11}	2.57×10^{11}
^{41}Ca	1.03×10^{5} y	7.61×10^{9}	7.72×10^{9}
^{45}Ca	163 d	7.06×10^{12}	7.16×10^{12}
^{47}Ca	4.54 d	7.59×10^{11}	7.70×10^{11}
^{46}Sc	83.8 d	9.22×10^{9}	9.35×10^{9}
^{47}Sc	3.35 d	1.45×10^{10}	1.47×10^{10}
^{48}Sc	43.67 h	7.23×10^{9}	7.33×10^{9}
^{44}Ti	47.3 y	2.71×10^{8}	2.75×10^{8}
^{48}V	24.0 d	9.03×10^{10}	9.16×10^{10}
^{49}V	330 d	9.25×10^{10}	9.38×10^{10}
^{51}Cr	27.7 d	2.95×10^{11}	2.99×10^{11}
^{52}Mn	5.59 d	7.95×10^{10}	8.06×10^{10}
^{54}Mn	313 d	4.20×10^{11}	4.26×10^{11}
^{55}Fe	2.70 y	2.53×10^{12}	2.57×10^{12}
^{59}Fe	44.5 d	1.01×10^{11}	1.02×10^{11}
Total		**5.50×10^{13}**	**5.57×10^{13}**

The total radioactivity from isotopes which emit gammas can be calculated from Table 5.7. In Table 5.8 the activity of these isotopes after different decay times is listed in comparison to the total activity of all isotopes produced in the concrete. This data, which is also illustrated in Figure 5.3, leads to the conclusion that the activity is dominated by β-emitters, especially after long decay times. It can be concluded from Table 5.7 that on time scales greater than 100 years the γ-activity is dominated by the decays of ^{42}K, ^{44}Sc, ^{44}Ti and ^{26}Al. The radioactive isotopes ^{42}K and ^{44}Sc, both with half-lives shorter than one day, are produced by the decays of ^{42}Ar (^{42}Ar $\rightarrow$ ^{42}K) and ^{44}Ti (^{44}Ti $\rightarrow$ ^{44}Sc) which both have half-lives of 33 y and 47.3 y respectively.

Table 5.8: *Radioactivity in the concrete of NGS-99 after shutdown and different decay times.*

Decay time in y	Total activity	Only γ-activity
0	5.58×10^{13}	2.30×10^{13}
1	7.40×10^{12}	1.26×10^{12}
2	5.19×10^{12}	8.86×10^{11}
5	3.14×10^{12}	3.68×10^{11}
10	1.86×10^{12}	9.60×10^{10}
20	9.42×10^{11}	7.41×10^{9}
50	2.18×10^{11}	4.90×10^{8}
100	6.28×10^{10}	2.21×10^{8}
200	4.37×10^{10}	6.16×10^{7}
500	2.62×10^{10}	2.41×10^{7}
1000	1.53×10^{10}	2.34×10^{7}

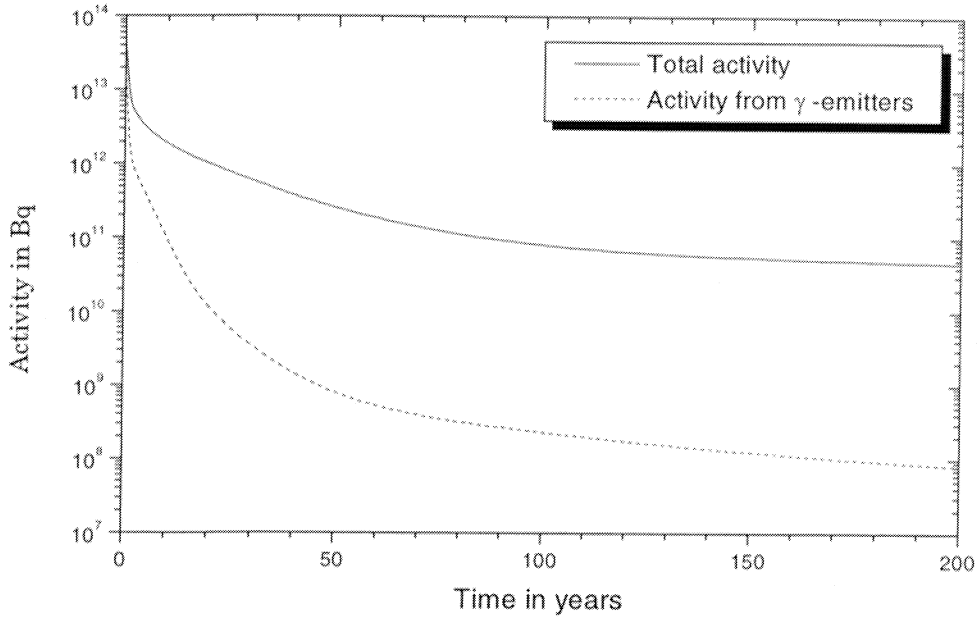

Figure 5.3: *Radioactivity in the concrete of NGS-99.*

5.3 Radioactivity in the Groundwater

Groundwater protection is a significant public concern which entails that the protection of groundwater resources from contamination with radionuclides is important in the highest degree. It should be stressed that, in principle, radioactivity can be produced in both the earth itself and in the water it contains. Hence, a precise knowledge of activation and leaching of the radionuclides into the geological material outside the installed structures is essential. The rock of the Geneva area consists of variable-quality strata ranging from relatively soft marls to extremely hard sandstone. The molasse is overlain by moraines from the glacial periods of Riss and Wurm (Figure 2.6). The moraine is known to be the water-bearing layer and as the NGS structures have to be excavated almost entirely from molasse-rock no direct contamination of the ground water resources is expected. Nevertheless, any seepage of ground-water from the rock will be towards the excavation. Consequently, the production of radionuclides which could find their way into a drinking-water supply has to be considered.

In the study of Borak *et al* [Bor72] first the radioactivity produced in soil was measured and then laboratory experiments were performed to determine which radionuclides and what fraction of them could be leached by water. The radionuclides ^{3}H, ^{7}Be, ^{22}Na, ^{45}Ca, ^{46}Sc, ^{48}V, ^{51}Cr, ^{54}Mn, ^{55}Fe, ^{59}Fe and ^{60}Co were identified but only ^{3}H, ^{22}Na, ^{45}Ca and ^{54}Mn were observed in leach water.

Among the different radionuclides which could find their way into a drinking-water supply, only ^{3}H and ^{22}Na are of any significance, since ^{7}Be is strongly re-absorbed by any

rock through which the ground-water may filter [Sta73] and the migration rate of the other nuclides is very slow in comparison with their half-lives [Aws71]. In general, 10-20% of ^{22}Na and all the tritium can be leached out of irradiated rock [Tho88]. Given the probabilities of radionuclide production in molasse listed in Table 3.9, 0.03 nuclei of ^{3}H and 0.0017 nuclei of ^{22}Na will be found in the groundwater for each star produced in the molasse. Since the proportion by volume of water in the molasse is estimated to be 10% [Ste89], the concentration of radioactivity that will be found in the water for a star density of 1 cm^{-3} in the molasse is 5.34×10^{-10} Bq/cm^3 of ^{3}H and 1.44×10^{-10} Bq/cm^3 of ^{22}Na. In addition, the direct production of tritium by spallation reactions in the oxygen of the water has to be added to the previous ^{3}H value. The number of nuclei of ^{3}H produced per star in water is 0.113 [Tho88]. The interaction mean free path in water, obtained from FLUKA, is approximately twice that in rock and, therefore, the tritium activity produced directly in water for unit star density in rock is 1.0×10^{-10} Bq/cm^3. Consequently, the total tritium activity for unit star density in rock is 6.34×10^{-10} Bq/cm^3.

By multiplying these figures by the number of protons sent to the neutrino facility per year and by the star production in rock of 37.1 (NGS-99) per proton an annual production of 1.2×10^{12} Bq of ^{3}H and 2.7×10^{11} Bq of ^{22}Na is given. It should be emphasized that the values for NGS-98 are higher by the factor of 1.2. In essence, the figure for tritium is very small compared to the CERN annual release constraint of 1.2×10^{15} Bq but the calculated figure for ^{22}Na is nearly as large as the annual release constraint which is 2.8×10^{11} Bq. It is intended that all drainage water from both the target cavern (released via ECA4 of the SPS) and from the hadron-stopper region (released at LHC Point 8) will be checked for its radioactivity concentration before release. In the event of high levels of ^{22}Na, the water will have to be evaporated and the activity disposed of as solid waste as is done in the present V0 pit of the present neutrino facility.

5.4 Determination of Radioactivity in the Air

Radioisotope production in air is one of the major radiological concerns at hadron accelerators. This chapter gives a detailed account on the production of radioactivity produced in the air of the neutrino facility. If the accelerator enclosures were completely sealed there would be no releases to the outside world and the hazard of these airborne radionuclides would be entirely restricted to people who might have to enter the enclosure. In general, ventilation is required to provide cooling of components and fresh breathing air for workers.

Commonly, the principle source of radioactivity in air is due to the direct interaction of primary and secondary particles with the constituent target nuclei in the air. The most abundant stable isotopes which can be found in the atmosphere are given in Table 5.9.

Table 5.9: *Isotope composition of air (adapted from Tho88).*

Isotope	**Percentage by volume**
^{14}N	78.1
^{16}O	21.2
^{40}Ar	0.46
^{15}N	0.28
^{18}O	0.04

Particular emphasis is often only put on some isotopes, such as ^{3}H, ^{7}Be, ^{11}C, ^{13}N, ^{14}O, ^{15}O and ^{41}Ar [Sul92] in case of activation, neglecting those which could also contribute to radioactivity. Many of these radioisotopes have half-lives of a few minutes, like the one from oxygen and nitrogen, while others have half-lives of several years as, for example, spallation isotopes from argon.

In the following a detailed method for the calculation of air activation is developed. In essence, the hadron tracklength in a Monte-Carlo simulation has to be scored and the results obtained have to be folded with the partial production cross-section of the radioactive isotopes. The yield Y_i of a radionuclide i produced by a hadronic interaction in air is calculated by integrating the production cross-sections with the particle track-length spectra and summing over all possible parent elements j and all hadron components k in the cascade

$$Y_i = \sum_{j,k} n_j \int \sigma_{ijk}(E)\, \Lambda_k(E)\, \mathrm{d}E \,, \tag{5.3}$$

where n_j is the atomic concentration of the element j in air per cm^3 and σ_{ijk} is the cross-section for the production of the radionuclide i in the reaction of the particles of type k and

energy E on the nucleus *j*. Assuming that Λ_k is the sum of track-lengths in cm of the hadrons of type *k* and energy E.

The succeeding simulations underlying the preceding formula were calculated by scoring the hadron track-length of all regions of the target cavern containing air by using a logarithmic energy binning with ten bins per decade. In order to be consistent with the cross-section data base [Huh97] used for this analysis which was set up for the LHC, the upper energy limit for scoring was taken to be 10 TeV. The lower limit for charged hadrons was 10 MeV and low-energy neutrons were scored in the 72-group structure of FLUKA. Since the upper bound of the low-energy neutron group structure is 19.6 MeV, 57 logarithmic bins will have a factor width of 1.2593 which is close to $10^{0.1}$= 1.2589. By default FLUKA normalizes track-lengths by assuming that all regions have a volume of 1 cm^3. The track-length spectra as a function of energy of neutrons, protons, and charged pions summed over all the air regions of the neutrino cavern (NGS-99) are illustrated in Figure 5.4. For a detailed comparison, the spectra taken from the study of air activation in the LHC dump cavern [Daw98] and the CMS experimental cavern [Huh96] are also given. The spectra for the neutrino cavern resemble the CMS spectra which include the high-energy secondaries produced in the p-p collisions in the forward regions of the detector. The high-energy part of the spectra of the dump cavern are characteristic of those for lateral shields [Roe93]. For the neutron spectra, the ratio of the 0.1–1 MeV peak to the 70 MeV peak is very similar for all the cases. However, there are relatively more neutrons below 0.1 keV in the dump cavern than in the other two cases.

For the calculation of the production yield Y_i, the integration over energy in equation (5.3) was replaced by a summation over the energy bins which were used in the track-length scoring, whereby, the effective energy binning was taken as the geometrical mean of the upper and the lower bin limits. The calculated production yield for 39 radioisotopes of interest to the neutrino target cavern of NGS-98 and NGS-99 are given in Table 5.10 along with their half-lives taken from [ICR83]. In addition, the ratio between both cases is also listed. It can be seen that, in general, the isotope production per proton is slightly smaller in NGS-99; only for a small number of isotopes which are dominantly produced by thermal neutrons the production is lower by 20 %. This decrease is due to an additional concrete shielding in NGS-99 and can be explained by the different neutron fluxes shown in Figure 5.5.

In order to compare the production in the neutrino cavern with other experiments planned at CERN the calculated production yield in the LHC dump cavern and in the CMS experimental cavern of the LHC are summarized in Table 5.11. More information about the comparison is contained in Table 5.12, where the relative production rates are given. The data are only presented for selected isotopes: a) ^{7}Be as a typical spallation product from C, N and O and ^{32}P as a typical spallation product from Ar, b) ^{3}H, ^{13}N and ^{15}O as typical products of reactions in the 10–100 MeV region, c) ^{11}C as an isotope produced mainly by spallation from O and N but also by low-energy neutron reactions with C and d) ^{14}C and ^{41}Ar as typical products of thermal neutron reactions. Furthermore, the particle spectra illustrated in Figure 5.4 demonstrate that proton and pion spallation reactions dominate in the neutrino and CMS case whereas thermal neutrons are more important for the dump cavern. This is reflected in the isotope ratios of Table 5.12.

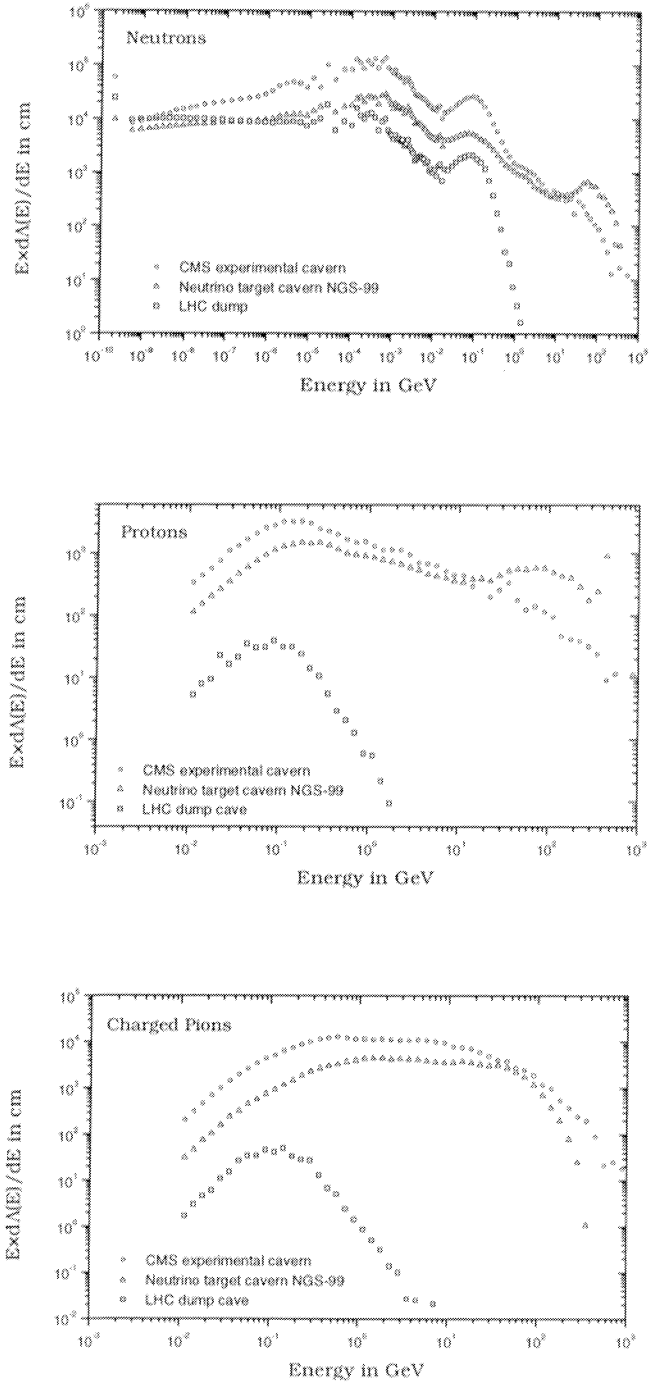

Figure 5.4: *Comparison of particle spectra in the air for the CMS experimental cavern, the neutrino target cavern, and an LHC dump cave.*

Table 5.10: *Production of radionuclides in the air of the target cavern of NGS-98 and NGS-99 (in nuclei per proton).*

Radionuclide	Half-life	Neutrino cavern NGS-98	Neutrino cavern NGS-99	Ratio NGS-99/NGS-98
^{3}H	12.35 y	4.57×10^{-2}	4.16×10^{-2}	0.91
^{7}Be	53.3 d	1.39×10^{-2}	1.34×10^{-2}	0.96
^{10}Be	1.60×10^{6} y	7.18×10^{-3}	7.13×10^{-3}	0.99
^{11}C	20.38 m	2.34×10^{-2}	2.31×10^{-2}	0.99
^{14}C	5730.0 y	6.30×10^{0}	5.00×10^{0}	0.79
^{13}N	9.965 m	2.29×10^{-2}	2.21×10^{-2}	0.97
^{14}O	71.0 s	1.32×10^{-3}	1.31×10^{-3}	1.00
^{15}O	122.24 s	1.55×10^{-2}	1.55×10^{-2}	1.00
^{19}O	27.1 s	2.94×10^{-6}	2.69×10^{-6}	0.91
^{18}F	109.77 m	5.03×10^{-5}	4.68×10^{-5}	0.93
^{23}Ne	28.0 s	6.23×10^{-6}	5.74×10^{-6}	0.92
^{24}Ne	3.38 m	1.47×10^{-6}	1.35×10^{-6}	0.92
^{22}Na	2.602 y	1.73×10^{-5}	1.62×10^{-5}	0.94
^{24}Na	15.0 h	2.33×10^{-5}	2.18×10^{-5}	0.93
^{25}Na	60.0 s	1.02×10^{-5}	9.45×10^{-6}	0.93
^{27}Mg	9.5 m	1.09×10^{-5}	1.01×10^{-5}	0.93
^{28}Mg	20.91 h	3.66×10^{-6}	3.45×10^{-6}	0.94
^{26}Al	7.16×10^{5} y	2.46×10^{-5}	2.32×10^{-5}	0.94
^{28}Al	2.24 m	5.78×10^{-5}	5.54×10^{-5}	0.96
^{29}Al	6.6 m	2.00×10^{-5}	1.88×10^{-5}	0.94
^{31}Si	157.3 m	3.22×10^{-5}	3.12×10^{-5}	0.97
^{32}Si	450.0 y	1.74×10^{-5}	1.70×10^{-5}	0.98
^{30}P	2.499 m	1.70×10^{-5}	1.64×10^{-5}	0.96
^{32}P	14.29 d	1.50×10^{-4}	1.47×10^{-4}	0.98
^{33}P	25.4 d	2.13×10^{-4}	2.11×10^{-4}	0.99
^{35}P	47.4 s	1.43×10^{-5}	1.42×10^{-5}	1.00
^{35}S	87.44 d	1.56×10^{-4}	1.55×10^{-4}	0.99
^{37}S	5.06 m	3.37×10^{-5}	3.36×10^{-5}	1.00
^{38}S	2.87 h	2.75×10^{-5}	2.71×10^{-5}	0.99
^{34m}Cl	32.0 m	6.96×10^{-6}	6.92×10^{-6}	0.99
^{36}Cl	3.01×10^{5} y	3.44×10^{-4}	3.41×10^{-4}	0.99
^{38}Cl	37.21 m	2.45×10^{-4}	2.42×10^{-4}	0.99
^{39}Cl	55.6 m	4.65×10^{-4}	4.58×10^{-4}	0.99
^{40}Cl	1.4 m	4.33×10^{-5}	4.32×10^{-5}	1.00
^{37}Ar	35.02 d	5.93×10^{-4}	5.18×10^{-4}	0.87
^{39}Ar	269.0 y	1.38×10^{-3}	1.36×10^{-3}	0.99
^{41}Ar	1.827 h	1.39×10^{-2}	1.10×10^{-2}	0.79
^{38}K	7.636 m	5.10×10^{-6}	5.03×10^{-6}	0.99
^{40}K	1.28×10^{9} y	1.98×10^{-5}	1.96×10^{-5}	0.99

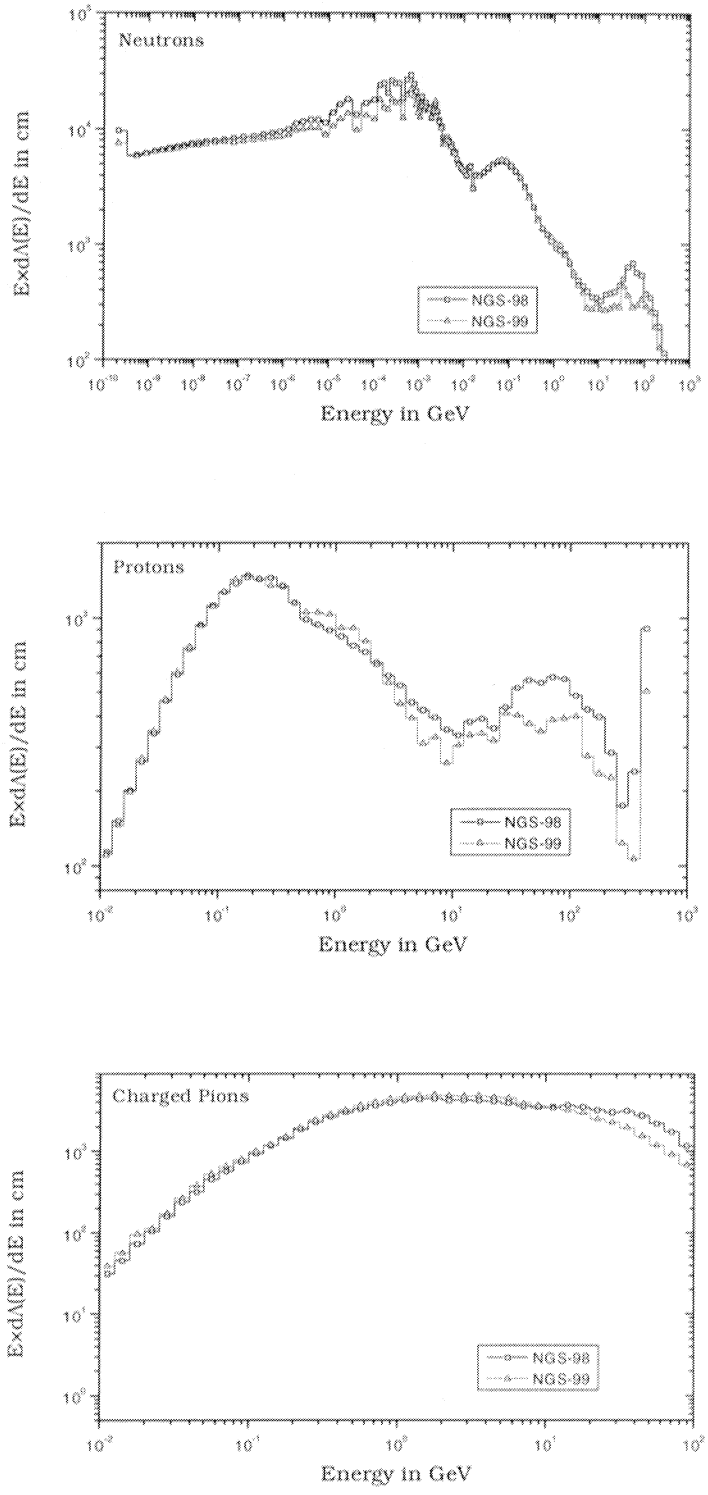

Figure 5.5: *Comparison of particle spectra in the air for the NGS-98 and NGS-99 neutrino target cavern.*

Table 5.11: *Production of radionuclides in the air of the target cavern (in nuclei per proton).*

Radionuclide	Half-life	Neutrino cavern NGS-99	LHC dump cavern	CMS experimental cavern
^{3}H	12.35 y	4.16×10^{-2}	2.47×10^{-5}	1.11×10^{-3}
^{7}Be	53.3 d	1.34×10^{-2}	4.68×10^{-4}	3.54×10^{-2}
^{10}Be	1.60×10^{6} y	7.13×10^{-3}	1.51×10^{-3}	2.59×10^{-2}
^{11}C	20.38 m	2.31×10^{-2}	9.94×10^{-4}	6.35×10^{-2}
^{14}C	5730.0 y	5.00×10^{0}	1.52×10^{1}	7.82×10^{0}
^{13}N	9.965 m	2.21×10^{-2}	2.63×10^{-3}	6.74×10^{-2}
^{14}O	71.0 s	1.31×10^{-3}	5.09×10^{-5}	3.69×10^{-3}
^{15}O	122.24 s	1.55×10^{-2}	1.14×10^{-3}	4.65×10^{-2}
^{19}O	27.1 s	2.69×10^{-6}	4.07×10^{-9}	5.53×10^{-6}
^{18}F	109.77 m	4.68×10^{-5}	2.30×10^{-7}	9.98×10^{-5}
^{23}Ne	28.0 s	5.74×10^{-6}	1.95×10^{-8}	1.21×10^{-5}
^{24}Ne	3.38 m	1.35×10^{-5}	2.68×10^{-9}	2.80×10^{-6}
^{22}Na	2.602 y	1.62×10^{-5}	1.40×10^{-7}	3.66×10^{-5}
^{24}Na	15.0 h	2.18×10^{-5}	2.42×10^{-7}	4.91×10^{-5}
^{25}Na	60.0 s	9.45×10^{-6}	5.12×10^{-8}	2.02×10^{-5}
^{27}Mg	9.5 m	1.01×10^{-5}	1.17×10^{-7}	2.17×10^{-5}
^{28}Mg	20.91 h	3.45×10^{-6}	8.10×10^{-8}	8.31×10^{-6}
^{26}Al	7.16×10^{5} y	2.32×10^{-4}	1.72×10^{-7}	5.42×10^{-5}
^{28}Al	2.24 m	5.54×10^{-5}	7.44×10^{-7}	1.39×10^{-4}
^{29}Al	6.6 m	1.88×10^{-5}	3.48×10^{-7}	4.37×10^{-5}
^{31}Si	157.3 m	3.12×10^{-5}	6.17×10^{-7}	8.50×10^{-5}
^{32}Si	450.0 y	1.70×10^{-5}	4.73×10^{-7}	4.75×10^{-5}
^{30}P	2.499 m	1.64×10^{-5}	1.50×10^{-7}	4.30×10^{-5}
^{32}P	14.29 d	1.47×10^{-4}	4.34×10^{-6}	4.13×10^{-4}
^{33}P	25.4 d	2.11×10^{-4}	9.96×10^{-6}	6.18×10^{-4}
^{35}P	47.4 s	1.42×10^{-5}	1.11×10^{-6}	4.44×10^{-5}
^{35}S	87.44 d	1.55×10^{-4}	1.52×10^{-5}	4.98×10^{-4}
^{37}S	5.06 m	3.36×10^{-5}	5.43×10^{-6}	1.18×10^{-4}
^{38}S	2.87 h	2.71×10^{-5}	2.78×10^{-6}	8.70×10^{-5}
^{34m}Cl	32.0 m	6.92×10^{-6}	2.48×10^{-7}	1.97×10^{-5}
^{36}Cl	3.01×10^{5} y	3.41×10^{-4}	4.18×10^{-5}	1.16×10^{-3}
^{38}Cl	37.21 m	2.42×10^{-4}	3.89×10^{-5}	8.41×10^{-4}
^{39}Cl	55.6 m	4.58×10^{-4}	6.04×10^{-5}	1.48×10^{-3}
^{40}Cl	1.4 m	4.32×10^{-5}	1.30×10^{-5}	1.75×10^{-4}
^{37}Ar	35.02 d	5.18×10^{-4}	9.10×10^{-4}	1.25×10^{-3}
^{39}Ar	269.0 y	1.36×10^{-3}	2.95×10^{-4}	4.57×10^{-3}
^{41}Ar	1.827 h	1.10×10^{-2}	3.40×10^{-2}	1.69×10^{-2}
^{38}K	7.636 m	5.03×10^{-6}	9.70×10^{-8}	1.34×10^{-5}
^{40}K	1.28×10^{9} y	1.96×10^{-5}	6.82×10^{-7}	5.67×10^{-5}

Table 5.12: *Total production of selected radionuclides in the neutrino target cavern (NGS-99) relative to the total production in the LHC dump and CMS experimental caverns.*

Radionuclide	Neutrino/ LHC dump	Neutrino/CMS	CMS/LHC dump
^{3}H	16.8	0.37	44.9
^{7}Be	28.6	0.38	75.6
^{11}C	23.2	0.36	63.9
^{14}C	0.3	0.64	0.5
^{13}N	8.4	0.33	25.6
^{15}O	13.6	0.33	40.8
^{32}P	33.9	0.36	95.2
^{41}Ar	0.3	0.65	0.5

In fact, a considerably higher reduction concerning the release of radioactivity will be achieved if the air remains in a closed ventilation system. The ventilation unit of the target cavern and the service gallery is placed underground on the second level of the ventilation chamber and will cool and dehumidify the air in order to prevent any risk of corrosion of the equipment. This unit operates entirely on recirculated air except during access, with a circulation speed of 16000 m^3 per hour. The same air flow rate is foreseen for the ventilation system of the access gallery but it will only operate during access periods.

Since the volume of the target cavern, the service gallery, and the seven cross-galleries is approximately 5000 m^3, the so- called "mixing time" is 1125 seconds. When access to the target is required cavern the fresh air from the access gallery will be mixed with the air of the cavern. The activity of an isotope is generally given by λN, where λ is the decay constant and N is the number of radioactive nuclides. Adjustments for the presence of ventilation can be quite conveniently made for a given radionuclide, see [Huh96], by using an effective decay constant which includes the physical decay constant λ along with a ventilation term Q/V_{irr}, where Q is the volume of fresh air cycled through the cavern per second, and V_{irr} is the volume of air irradiated in the cavern. Thus, Q/V_{irr} is the number of air exchanges per unit time. The change in the number of nuclei N of a given radionuclide per time unit, due to air extraction and radioactive decay, is then given by

$$\frac{dN}{dt} = -N(\lambda + \frac{Q}{V_{irr}}). \qquad (5.4)$$

The solution to equation (5.4) is the well-known exponential decay law

$$N(t) = N_i \exp[(-\lambda + \frac{Q}{V_{irr}})t], \tag{5.5}$$

with N_i being the number of radionuclides in the cavern when ventilation with fresh air starts. N_i is given by

$$N_i = \frac{p\,x_i}{\lambda}\,[1 - \exp(-\lambda\, t_{irr})]\,\exp(-\lambda\, t_{lapse}), \tag{5.6}$$

where p is the average proton intensity on the target per second (5×10^{19} protons for 200 days), x_i is the production per proton taken from Table 5.10, t_{irr} is the irradiation time which is taken to be one-third of the 200 days and t_{lapse} is the delay between the end of the irradiation and the start of ventilating with fresh air. In the present calculations this waiting time was taken to be two hours.

The rate of the released activity extracted from the cavern is $\lambda\, N(t)\, Q/V_{irr}$, where N(t) is given by equation (5.5). Taking into account a delay time t_d which the air needs to reach the outside world from the target cavern via the access gallery and the ventilation ducts (1390 seconds) the rate of release of activity, $R(t)$, in Bq per second of a given radionuclide into the atmosphere is

$$R(t) = \frac{Q}{V_{irr}}\lambda\, N(t)\, \exp(-\lambda\, t_d). \tag{5.7}$$

The released activity, A_{rel}, vented to the atmosphere is obtained by integrating equation (5.7) from $t = 0$ to $t = \infty$. The solution is

$$A_{rel} = \frac{\lambda Q}{\lambda V_{irr} + Q} N_i \exp(-\lambda t_d). \tag{5.8}$$

In Table 5.13 the basic assumptions of the activity in the cavern at the end of an operating period of 67 days and the releases are given. Their importance can be judged by comparing them with the CERN Reference values which are valid for a single release point on the Meyrin Site [Hoe97] (see Table 5.14) The only point of concern could be the release of long-lived β/γ radionuclides because the release would exceed the daily reference value for NGS-98, as well as, for NGS-99.

Table 5.13: *Target cavern-production and release of radioactivity from 67 days of neutrino operation.*

Radionuclide	NGS-98		NGS-99	
	Production	Release	Production	Release
^{3}H	1.35×10^{9}	1.35×10^{9}	1.23×10^{9}	1.23×10^{9}
^{7}Be	2.33×10^{10}	2.33×10^{10}	2.24×10^{10}	2.24×10^{10}
^{10}Be	1.64×10^{3}	1.64×10^{3}	1.63×10^{3}	1.63×10^{3}
^{11}C	6.77×10^{10}	3.17×10^{8}	6.67×10^{10}	3.12×10^{8}
^{14}C	4.03×10^{8}	4.03×10^{8}	3.19×10^{8}	3.19×10^{8}
^{13}N	6.63×10^{10}	1.36×10^{6}	6.41×10^{10}	1.31×10^{6}
^{14}O	3.80×10^{9}	-	3.80×10^{9}	-
^{15}O	4.48×10^{10}	-	4.48×10^{10}	-
^{19}O	8.50×10^{6}	-	7.77×10^{6}	-
^{18}F	1.45×10^{8}	5.27×10^{7}	1.35×10^{8}	4.90×10^{7}
^{23}Ne	1.80×10^{7}	-	1.66×10^{7}	-
^{24}Ne	4.27×10^{6}	-	3.91×10^{6}	-
^{22}Na	2.38×10^{6}	2.38×10^{6}	2.23×10^{6}	2.23×10^{6}
^{24}Na	6.75×10^{7}	5.96×10^{7}	6.31×10^{7}	5.57×10^{7}
^{25}Na	2.95×10^{7}	-	2.73×10^{7}	-
^{27}Mg	3.15×10^{7}	3.86×10^{2}	2.92×10^{7}	3.57×10^{2}
^{29}Mg	1.06×10^{7}	9.67×10^{6}	9.99×10^{6}	9.14×10^{6}
^{26}Al	1.26×10^{4}	1.26×10^{4}	1.18×10^{4}	1.18×10^{4}
^{28}Al	1.67×10^{8}	-	1.60×10^{8}	-
^{29}Al	5.78×10^{7}	5.72×10^{9}	5.44×10^{7}	5.38×10^{9}
^{31}Si	9.32×10^{7}	4.58×10^{7}	9.04×10^{7}	4.44×10^{7}
^{32}Si	1.42×10^{4}	1.42×10^{4}	1.39×10^{4}	1.39×10^{4}
^{30}P	4.92×10^{7}	-	4.75×10^{7}	-
^{32}P	4.16×10^{8}	4.14×10^{8}	4.08×10^{8}	4.06×10^{8}
^{33}P	5.17×10^{8}	5.16×10^{8}	5.11×10^{8}	5.10×10^{8}
^{35}P	4.13×10^{7}	-	4.12×10^{7}	-
^{35}S	1.85×10^{8}	1.85×10^{8}	1.84×10^{8}	1.84×10^{8}
^{37}S	9.75×10^{7}	-	9.73×10^{7}	-
^{38}S	7.95×10^{7}	4.16×10^{7}	7.85×10^{7}	4.10×10^{7}
^{34m}Cl	2.01×10^{7}	6.44×10^{5}	2.00×10^{7}	6.40×10^{5}
^{36}Cl	4.19×10^{2}	4.19×10^{2}	4.15×10^{2}	4.15×10^{2}
^{38}Cl	7.08×10^{8}	3.64×10^{7}	7.01×10^{8}	3.61×10^{7}
^{39}Cl	1.35×10^{9}	1.83×10^{8}	1.33×10^{9}	1.80×10^{8}
^{40}Cl	1.25×10^{8}	-	1.25×10^{8}	-
^{37}Ar	1.26×10^{9}	1.25×10^{9}	1.10×10^{9}	1.09×10^{9}
^{39}Ar	1.88×10^{6}	1.88×10^{6}	1.85×10^{6}	1.85×10^{6}
^{41}Ar	4.03×10^{10}	1.46×10^{10}	3.19×10^{10}	1.15×10^{10}
^{38}K	1.48×10^{7}	1.23×10^{1}	1.46×10^{7}	1.22×10^{1}
^{40}K	5.66×10^{-3}	-	5.62×10^{-3}	-

Table 5.14: *Comparison of release from 67 days of neutrino operation with CERN Reference Values.*

Radionuclide	Release in Bq		CERN limits in Bq	
	NGS-98	NGS-99	Annual release in Bq	Daily release in Bq
^{3}H	1.35×10^{9}	1.23×10^{9}	1.00×10^{16}	2.30×10^{14}
^{7}Be	2.33×10^{10}	2.24×10^{10}	3.00×10^{13}	1.40×10^{12}
All β/γ with $T_{½} < 1$ day	1.53×10^{10}	1.23×10^{10}	3.80×10^{15}	5.00×10^{13}
Other β/γ with $T_{½} > 1$ day	2.77×10^{9}	2.52×10^{9}	4.00×10^{10}	2.00×10^{9}

In addition to the CERN limits shown in Table 5.14 a recent paper [Voj98] describes the calculation of effective dose due to releases of radioactivity around the CERN Meyrin site. It contains new annual release limits which are lower than the present CERN limits, see Table 5.15. The daily release limits are scaled from the CERN reference values in Table 5.15 as annual release.

Table 5.15: *Release limits into the air from [Voj98].*

Radionuclide	New limits in Bq	
	Annual release in Bq	Daily release in Bq
^{3}H	3.50×10^{15}	8.05×10^{13}
^{7}Be	1.00×10^{13}	4.67×10^{11}
All β/γ with $T_{½} < 1$ day	6.00×10^{14}	7.89×10^{12}
Other β/γ with $T_{½} > 1$ day	1.30×10^{10}	6.50×10^{8}

Several ventilation scenarios were considered in order to satisfy the limits of Table 5.15 for NGS-99, especially the limit of radionuclides with a half-life greater than one day. The waiting time of 2 hours before the ventilation starts was left unchanged because the limits of short-lived isotopes were always fulfilled. In addition to 67 days of operation the daily and the corresponding annual release were calculated after 7, 14, 21 and 28 days of neutrino operation, respectively. Table 5.16 depicts that the release of isotopes with half lives greater than 1 day exceeds the new daily release limit in all cases except the one for 7 days. But, nevertheless, if the release was done every 7 days the annual release limit would be too high (see Table 5.17). In Figure 5.6 the basic assumptions of the annual and the daily release of

longer lived isotopes ($T_{½}$>1 day) together with the present CERN limits and the new limits are presented. Besides, the annual release is in all cases below the CERN limit whereas the daily release will be too high if the air is released more than 40 days after continuous operation. Furthermore, it can be concluded that the new daily release limit is reached after 10 days of operation and, in addition, the release is below the new annual release limit. Note that for all scenarios a waiting time of 2 hours was assumed and an increased waiting time of about 8 hours would only slightly improve the situation.

Table 5.16: *Release of radioactivity after 7, 14, 21 and 28 days of neutrino operation.*

Radionuclide	Daily release in Bq			
	7d	14d	21d	28d
^{3}H	1.29×10^{8}	2.59×10^{8}	3.88×10^{8}	5.17×10^{8}
^{7}Be	3.36×10^{9}	6.43×10^{9}	9.23×10^{9}	1.18×10^{10}
All β/γ with $T_{½}$ < 1 day	1.23×10^{10}	1.23×10^{10}	1.23×10^{10}	1.23×10^{10}
Other β/γ with $T_{½}$ > 1 day	4.79×10^{8}	8.78×10^{8}	1.21×10^{9}	1.50×10^{9}

Table 5.17: *Annual release of radioactivity when ventilating the cavern after 7, 14, 21 and 28 days of neutrino operation.*

Radionuclide	Annual release in Bq			
	7d	14d	21d	28d
^{3}H	3.70×10^{9}	3.69×10^{9}	3.69×10^{9}	3.69×10^{9}
^{7}Be	9.60×10^{10}	9.19×10^{10}	8.79×10^{10}	8.42×10^{10}
All β/γ with $T_{½}$ < 1 day	3.50×10^{11}	1.75×10^{11}	1.17×10^{11}	8.76×10^{10}
Other β/γ with $T_{½}$ > 1 day	1.37×10^{10}	1.25×10^{10}	1.16×10^{10}	1.07×10^{10}

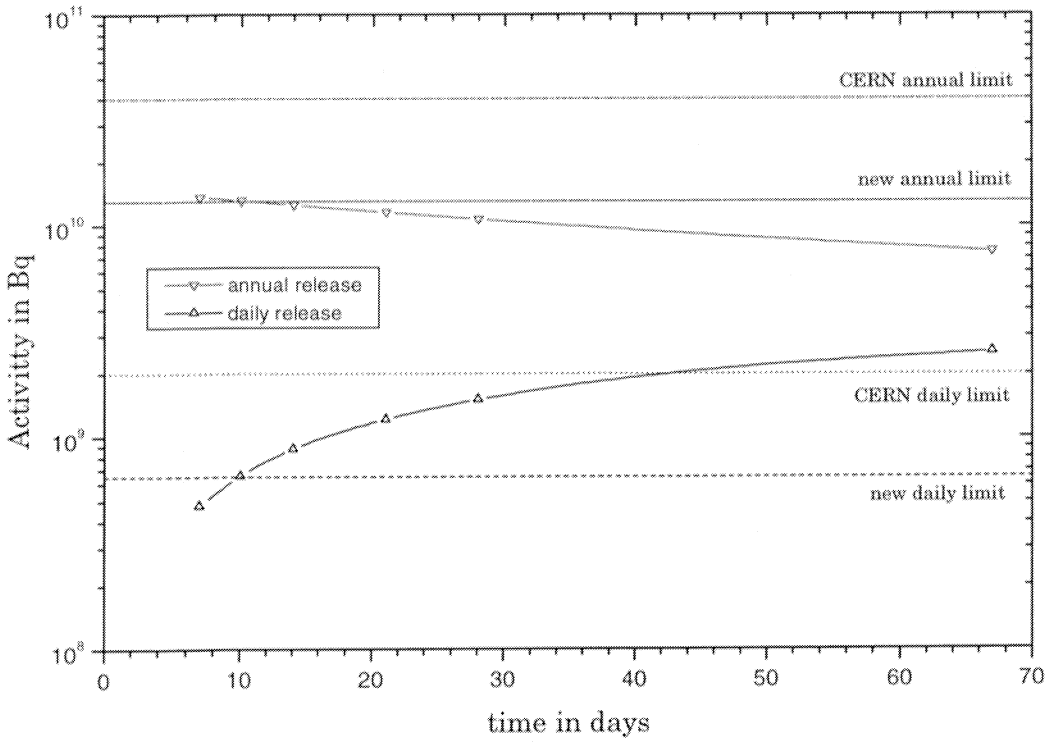

Figure 5.6: *Daily release to the atmosphere and the corresponding annual release of radioactivity from isotopes with a half-life greater than one day after different times of neutrino operation. The CERN limits and the new limits from [Voj98] are also shown.*

It is also of interest to calculate the production of radioactive nuclides in the other air volumes of the neutrino facilities, *viz.* the decay tube and the small air volume between the end of the decay tube and the graphite core of the hadron-stopper. The reduced pressure of air in the decay tube was correctly taken into account. The activity in these volumes after one year of operation is given in Table 5.18. It can be seen that the activities are at least two orders of magnitude lower than those of Table 5.13 and, thus, the actual release of air from these volumes should not be subjected to any constraints. Note that the activation in the target cavern is based on an irradiation time of only 67 days, whereas the numbers in Table 5.18 are calculated for 200 days of operation.

Table 5.18: *Production of radioactivity in the air of the decay tunnel and the upstream window of the hadron stopper after 1 year of operation.*

Radionuclide	NGS-98		NGS-99	
	Decay Tunnel Bq	Hadron Stopper Bq	Decay Tunnel Bq	Hadron Stopper Bq
^{3}H	2.10×10^{7}	2.25×10^{6}	2.67×10^{7}	3.69×10^{6}
^{7}Be	1.33×10^{8}	1.57×10^{7}	1.78×10^{8}	3.36×107
^{10}Be	8.85×10^{0}	4.32×10^{0}	1.24×10^{1}	7.84×10^{0}
^{11}C	1.87×10^{8}	3.10×10^{7}	2.46×10^{8}	6.84×10^{7}
^{14}C	1.32×10^{5}	2.07×10^{6}	1.60×10^{5}	2.67×10^{6}
^{13}N	1.74×10^{8}	4.09×10^{7}	2.26×10^{8}	8.05×10^{7}
^{14}O	7.54×10^{6}	1.82×10^{6}	1.03×10^{7}	3.86×10^{6}
^{15}O	9.00×10^{7}	2.07×10^{7}	1.24×10^{8}	5.05×10^{7}
^{19}O	4.66×10^{4}	3.35×10^{3}	5.88×10^{4}	5.60×10^{3}
^{18}F	7.08×10^{5}	5.45×10^{4}	9.03×10^{5}	1.01×10^{5}
^{23}Ne	9.40×10^{4}	6.89×10^{3}	1.19×10^{5}	1.23×10^{4}
^{24}Ne	2.30×10^{4}	1.66×10^{3}	2.90×10^{4}	2.84×10^{3}
^{22}Na	3.12×10^{4}	2.43×10^{3}	4.06×10^{4}	4.91×10^{3}
^{24}Na	3.15×10^{5}	2.51×10^{4}	4.00×10^{5}	4.99×10^{4}
^{25}Na	1.48×10^{5}	1.11×10^{4}	1.88×10^{5}	2.06×10^{4}
^{27}Mg	1.59×10^{5}	1.27×10^{4}	1.94×10^{5}	2.34×10^{4}
^{28}Mg	4.35×10^{4}	3.89×10^{3}	5.55×10^{4}	8.60×10^{3}
^{26}Al	1.64×10^{-3}	1.29×10^{-2}	2.18×10^{-1}	2.76×10^{-2}
^{28}Al	6.23×10^{5}	5.53×10^{4}	8.48×10^{5}	1.32×10^{5}
^{29}Al	2.56×10^{5}	2.24×10^{4}	3.17×10^{5}	4.63×10^{4}
^{31}Si	2.99×10^{5}	3.26×10^{4}	4.20×10^{5}	8.10×10^{4}
^{32}Si	1.26×10^{2}	1.52×10^{1}	1.78×10^{2}	3.86×10^{1}
^{30}P	1.66×10^{5}	1.62×10^{4}	2.34×10^{5}	4.05×10^{4}
^{32}P	1.23×10^{6}	1.57×10^{5}	1.73×10^{6}	4.02×10^{5}
^{33}P	1.57×10^{6}	2.47×10^{5}	2.23×10^{6}	6.15×10^{5}
^{35}P	9.39×10^{4}	1.92×10^{4}	1.32×10^{5}	4.57×10^{4}
^{35}S	7.81×10^{5}	1.87×10^{5}	1.10×10^{6}	4.22×10^{5}
^{37}S	1.41×10^{5}	7.16×10^{4}	2.05×10^{5}	1.53×10^{5}
^{38}S	2.07×10^{5}	4.18×10^{4}	2.67×10^{5}	9.25×10^{4}
^{34m}Cl	5.07×10^{4}	7.50×10^{3}	7.11×10^{4}	1.97×104
^{36}Cl	2.68×10^{0}	7.58E-01	3.69×10^{0}	1.61×10^{0}
^{38}Cl	1.54×10^{6}	4.88×10^{5}	2.06×10^{6}	9.56×10^{5}
^{39}Cl	3.39×10^{6}	8.36×10^{5}	4.45×10^{6}	1.67×10^{6}
^{40}Cl	1.34×10^{5}	1.38×10^{5}	2.04×10^{5}	2.44×10^{5}
^{37}Ar	1.33×10^{6}	2.23×10^{6}	1.80×10^{6}	3.18×10^{6}
^{38}Ar	1.05×10^{4}	5.02×10^{3}	1.41×10^{4}	9.49×10^{3}
^{41}Ar	3.96×10^{6}	6.93×10^{7}	4.64×10^{6}	8.90×10^{7}
^{38}K	3.42×10^{4}	6.59×10^{3}	4.92×10^{4}	1.37×10^{4}
^{40}K	2.79×10^{-5}	1.27×10^{-5}	4.42×10^{-5}	1.61×10^{-5}
Total	6.31×10^{8}	1.88×10^{8}	8.33×10^{8}	3.41×10^{8}

From Table 5.13, it can be concluded that the release of radioactivity from ^{14}C and ^{37}Ar, mainly produced by thermal neutron activation

$$^{14}N(n,p)^{14}C$$
$$^{36}Ar(n,\gamma)^{37}Ar,$$

is 1×10^9 Bq. This is more than 40 % of the total release of all isotopes with a half-life greater than one day. The (n,p) capture cross-section of ^{14}N is 1.769 b at 0.0253 eV [BNL] whereas ^{36}Ar has a neutron capture cross-section of 5b at 0.0253 eV [NDE].

One possibility to reduce the release would be to diminish the flux of low-energy neutrons, especially of thermal neutrons, which could be achieved without an additional shielding around the beam line but by using concrete mixed with a small amount of boron ignoring the additional γ's because during operation, access is denied to everybody. Boron is an excellent neutron absorber with a thermal neutron capture cross-section (n,α) of 3837 b at 0.0253 eV [BNL]. The calculation of the produced radioactivity in air by using a mixture of 1% (mass fraction) of boron and concrete after 67 days of neutrino operation is compared to the activity induced in pure concrete, therefore, see Figure 5.7. Note that the production of ^{14}C and ^{41}Ar decreased by nearly 45% and for that of ^{37}Ar still by 25%. But, nevertheless, more emphasis is put on the release of the radioactivity than on the production which is shown is Figure 5.8.

The total activity of ^{3}H and ^{7}Be produced by spallation is not influenced by the additional boron in the concrete but the release of radioisotopes with a half-life less than one day decreased by 40 % and the release of radioisotopes with a half-life greater than one day by 16 %.

Table 5.19: *Release of radioactivity to the air after 67 days of neutrino operation for normal concrete shielding and for concrete with 1% of boron.*

Radionuclide	Release in Bq		CERN limits in Bq	
	NGS-99	NGS-99 (1% Boron)	Annual release in Bq	Daily release in Bq
^{3}H	1.23×10^{9}	1.22×10^{9}	1.00×10^{16}	2.30×10^{14}
^{7}Be	2.24×10^{10}	2.24×10^{10}	3.00×10^{13}	1.40×10^{12}
All β/γ with $T_{½} < 1$ day	1.23×10^{10}	7.10×10^{9}	3.80×10^{15}	5.00×10^{13}
Other β/γ with $T_{½} > 1$ day	2.52×10^{9}	2.10×10^{9}	4.00×10^{10}	2.00×10^{9}

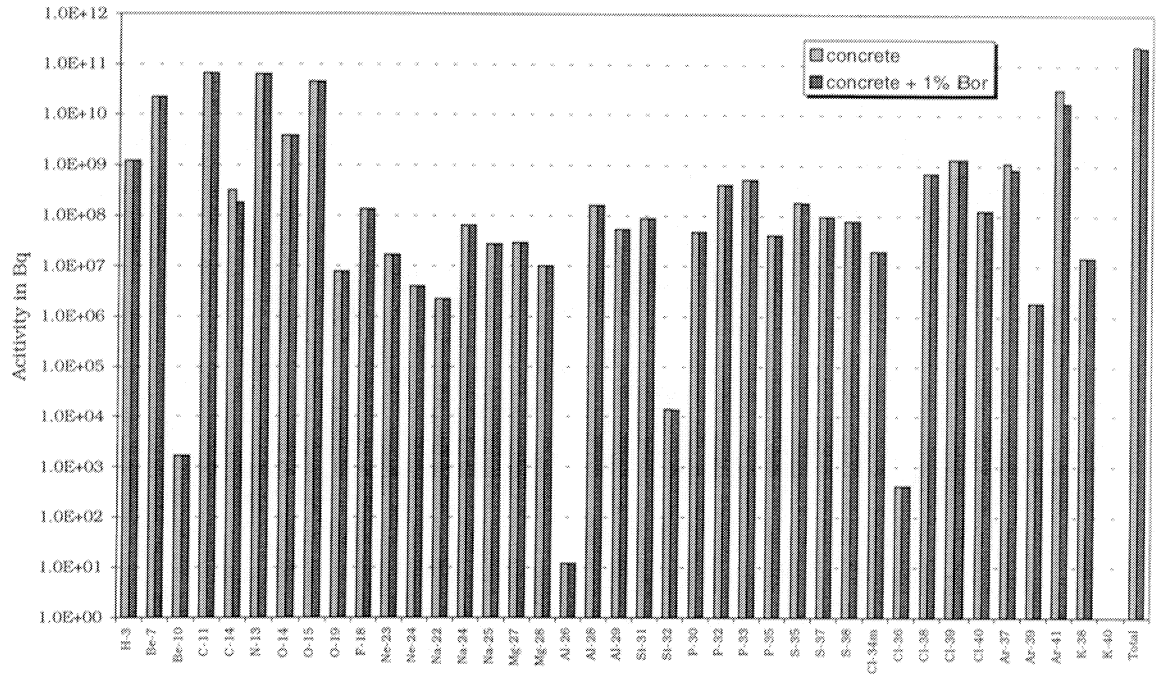

Figure 5.7: *Production of radioactivity in the air of NGS-99.*

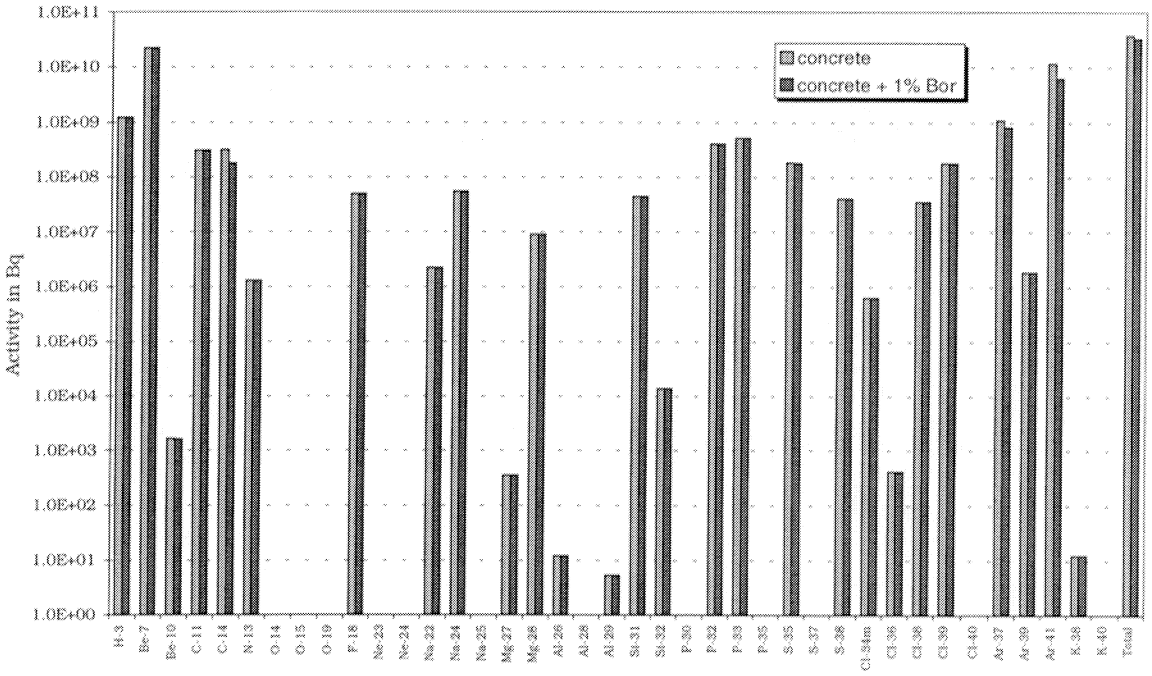

Figure 5.8: *Release of radioactivity in the air of NGS-99.*

5.5 Tritium Production in the Helium Circuits

At high-energy accelerator facilities, tritium is considered to be one of the major nuclides in residual activities, especially after long term operation. The two aluminum tubes, one between the horn and the reflector, the second one between the reflector and the beginning of the decay tunnel, and the target box are filled with helium to reduce particle interactions with air molecules. The only radioactive isotope which can be produced is tritium and the following is intended to give an estimate for the production of tritium in the helium tanks and in the helium regions around the target.

The cross-section for the production of tritium in hadron interactions with helium is approximately 30 mbarns [Ste71, Ilj91]. The lack of experimental knowledge concerning this cross-section means that in the present work this cross-section was assumed to be constant above 30 MeV and to be independent of the hadron type. Thus, from the total hadron track-lengths in the helium regions it is possible to estimate the production of tritium. The conversion factor F_{tl} is given by

$$F_{tl} = \frac{Avogadro's \quad Number}{22.4 liters} \times 30 mbars = 8.1 \times 10^{-7} \text{ cm}^{-1}. \qquad (5.9)$$

Another way of calculating the tritium activity in helium is provided by FLUKA simulations. In this particular case, the total number of stars in the helium was scored. Since the inelastic cross-section σ is approximately 110 mbarns, which is based on the formula

$$\sigma = \frac{A}{N \times \lambda \times \rho}, \qquad (5.10)$$

where A is the atomic weight, N is the Avogadro number, ρ is the density of He and λ is the interaction length in He, stars can be converted to tritium production using the factor F_{stars}

$$F_{stars} = 30 \ mbarns \ / \ 110 \ mbarns = 0.27. \qquad (5.11)$$

The track-lengths and stars with corresponding estimates of tritium production in atoms per proton are given in Table 5.20 and in Table 5.21.

Table 5.20: *Production of tritium in the helium circuits of NGS-98.*

Region	From Track-length		From stars	
	Track-length, cm	**^{3}H per proton**	**Total stars**	**^{3}H per proton**
Target Box	3280	2.7×10^{-3}	8.37×10^{-3}	2.3×10^{-3}
Front He bag	11500	9.3×10^{-3}	2.56×10^{-2}	6.9×10^{-3}
Second He bag	1070	8.7×10^{-4}	2.37×10^{-3}	6.4×10^{-4}
Total	15850	1.3×10^{-2}	3.63×10^{-1}	9.8×10^{-3}

Table 5.21: *Production of tritium in the helium circuits of NGS-99.*

Region	From Track-length		From stars	
	Track-length, cm	**^{3}H per proton**	**Total stars**	**^{3}H per proton**
Target Box	3287	2.7×10^{-3}	9.30×10^{-3}	2.5×10^{-3}
Front He bag	16460	1.3×10^{-2}	4.11×10^{-2}	1.1×10^{-2}
Second He bag	11034	8.9×10^{-3}	2.67×10^{-2}	7.2×10^{-3}
Total	30781	2.5×10^{-2}	7.71×10^{-2}	2.1×10^{-2}

It should be emphasized that the volume of the He-bags and the position of the bags in the target cavern have completely changed in NGS-99. The total volume of helium increased from 38.8 m^3 to 82.3 m^3.

The total tritium production is 0.013 (0.025) atoms per proton if calculated using the track-lengths and 0.010 (0.021) atoms per proton if calculated from the stars (in brackets the value for NGS-99). Considering that the star-production threshold is 50 MeV and the threshold for the track-length scoring is 30 MeV, this is excellent agreement. The total number of protons on target per year is 5×10^{19}, thus, the tritium produced in one year is

$$0.013 \times 5\times10^{19} \times \ln(2.0)/ (12.4 \times 365.25 \times 86400)$$
$$= 1.2 \times 10^{9}\,\text{Bq}$$

for NGS-98 and

$$0.025 \times 5\times10^{19} \times \ln(2.0)/ (12.4 \times 365.25 \times 86400)$$
$$= 2.2 \times 10^{9}\,\text{Bq}$$

for NGS-99. This is by about 40% lower than the production of tritium in the air per year, so it can be concluded, however, that even in the case of a total rupture of the helium circuit after one year's operation the release of tritium should be insignificant.

5.6 Activity in Iron

The relatively high density of iron, in conjunction with its low cost, makes iron an attractive shielding material. As discovered by Alsmiller and Barish (Als73), iron has a major deficiency as a shield for fast neutrons. Consequently, cast iron, iron that contains several percent of carbon, is often used as shielding material.

Nevertheless, one of the problems concerning the estimation of induced radioactivity in iron is the calculation of the production of ^{3}H. However, a large tritium production cross-section of 160 mbarn in iron was reported by Noguchi [Nog91] and the value 155 mbarn in copper was measured by Cumming *et al.* [Cum74]. They pointed out that the tritium cross-section depends largely on the incident proton energies and further proved a gradual increase with energy and level off at an energy range above approximately 2 GeV. Tritium emits only beta rays of 0.018 MeV, and in order to measure these beta rays rather complicated procedures such as chemical separation of tritium from irradiated materials are required. Consequently, a correct chemical analysis of the amount of produced ^{3}H is always complicate. The value of 160 mbarn for the ^{3}H production in iron is used as an over-estimation.

Since the inelastic cross-section used in the FLUKA program for iron is 740 mbarn, the number of nuclei of ^{3}H created per star is 0.216 (160 divided by 740). The number of stars produced per proton on target in various iron regions are summarized in Table 5.22 and in Table 5.23. Thus, the inventory of ^{3}H after 10 years of operation is equal to the number of stars multiplied by

$$0.216\ [\text{nuclei per star}] \times \frac{5\times10^{19}\ [\text{protons per year}]}{365.25\times86400\ [\text{secondes per year}]} \times \{1.0\text{-}\exp(\text{-}\ln(2)\times10/12.4)\}$$
$$= 1.5 \times 10^{11}\ \text{Bq}.$$

Furthermore, the tritium activities in the iron regions after 10 years of operation are given in Table 5.22 and in Table 5.23. The activities after 5, 50 and 100 years are simply obtained by multiplying the values of this table by 0.76, 0.061, and 3.7×10^{-3}, respectively. It should be stressed that the calculation of the tritium activity is based on production cross-sections of energies at 2 GeV. Taking into account that the cross-section increases with energies and levels off at 2 GeV these results are definitely very pessimistic.

The number of stars in the iron reinforcements of the concrete of the target cavern was estimated by assuming that one percent of the mass of the concrete is, in fact, iron. The copper collimator COLL.1 in NGS-98 is included in this study since the production cross-sections and assumptions made are also approximately as valid for copper as they are for iron.

Table 5.22: *Activity of tritium in the iron of NGS-98.*

Region	Total stars	Activity in Bq after a 10 year operation	Mass in t	Specific activity in Bq/g
Around the target station and around COLL1	28	4.2×10^{12}	128	3.4×10^{4}
In COLL1	160	2.4×10^{13}	12	2.1×10^{6}
Around the collimator COLL2	38	5.7×10^{12}	64	8.9×10^{4}
In COLL3	26	3.9×10^{12}	26	1.5×10^{5}
In the decay-pipe	22	3.3×10^{12}	1090	3.0×10^{3}
In the hadron stopper	32	4.8×10^{12}	1970	2.4×10^{3}
Collimator at the start of the decay tunnel	85	1.3×10^{13}	490	2.7×10^{4}
Reinforcement in the concrete of the cavern	0.66	1.0×10^{11}	43	2.3×10^{3}
Total	392	5.9×10^{13}	3823	1.5×10^{4}

Table 5.23: *Activity of tritium in the iron of NGS-99.*

Region	Total stars	Activity in Bq after a 10 year operation	Mass in t	Specific activity in Bq/g
Around the target station	31	4.7×10^{12}	106	4.4×10^{4}
Aside the horn	16	2.4×10^{12}	81	3.0×10^{4}
In the TDX	90	1.4×10^{13}	361	3.9×10^{4}
Around the 1.He-tube	56	8.4×10^{12}	193	4.4×10^{4}
In the decay-pipe	38	5.7×10^{12}	1090	5.2×10^{3}
In the hadron stopper	18	2.7×10^{12}	1970	1.4×10^{3}
Collimator at the end of the target cavern	46	6.9×10^{12}	353	2.0×10^{4}
Reinforcement in the concrete of the cavern	0.39	5.85×10^{10}	43	1.4×10^{3}
Total	296	4.4×10^{13}	4197	1.0×10^{4}

The Exemption Limit in Swiss Legislation, below which substances are not considered to be radioactive is 300 Bq/g for substances containing tritium. All items are considerably above this limit. It must be noted, however, that since tritium is not the only radionuclide produced, other limits may dominate the analysis.

It turned out to be reasonable to estimate the activity of gamma-emitting isotopes in cobalt-free iron or steel by assuming that one of three stars give rise to an isotope which decays by the emission of a single photon [Huh98]. The saturation activity is, thus, the star production rate averaged over the 200 days of operation in a year multiplied by 0.33. Using a number of 5×10^{19} protons on target during 200 days and the star data contained in Table 5.22 and Table 5.23, a value of 374 TBq (NGS-98) and 283 TBq (NGS-99) is obtained for the saturation activity for the iron comprising the shield. From the data of Gabriel and Santoro [Gab72] it is possible to estimate that the activity after a one-year irradiation and 100 hours of decay is 0.3 times the saturation activity. Furthermore, the activity after different decay times can be calculated using the Sullivan-Overton formula [Sul65]. For an irradiation time T and a decay time t, Sullivan and Overton showed that dose rates from irradiated materials such as iron varied as

$$\dot{D}(t) = B\,\Phi \ln[(T + t)/t], \tag{5.12}$$

where B is a constant of proportionality and Φ is the irradiating flux density. Using this, the activity after 200 days of operation and 100 hours of cooling relative to the one year of operation and 100 hours of cooling can be obtained. The Sullivan-Overton formula provides also a method to sum the contributions over the ten years of operation and for different cooling times after the end of neutrino target operation. Studies on the activation of materials [Huh98] suggest that the use of the Sullivan-Overton formula is valid for iron, for cooling times up to several years. For longer cooling times, however, activities calculated using the Sullivan-Overton formula tend to increasingly overestimate, so that for a cooling time of 30 years the overestimate could be greater by an order of magnitude. The resulting activities are given in Table 5.24 (NGS-98) and Table 5.25 (NGS-99).

Table 5.24: *Activity of gamma emitting isotopes in the iron (NGS-98) after 10 years of operation and for different cooling times.*

Region	Total Activity in Bq after different cooling times				Specific activity in Bq/g after
	1 years	5 years	50 years	500 years	5 years
Around the target station and around COLL1	2.7×10^{12}	1.2×10^{12}	1.9×10^{11}	2.1×10^{10}	9.3×10^{3}
In COLL1	1.6×10^{13}	6.8×10^{12}	1.1×10^{12}	1.2×10^{11}	5.7×10^{5}
Around the collimator COLL2	3.7×10^{12}	1.6×10^{12}	2.6×10^{11}	2.9×10^{10}	2.5×10^{4}
In COLL3	2.5×10^{12}	1.1×10^{12}	1.8×10^{11}	2.0×10^{10}	4.2×10^{4}
In the decay-pipe	2.2×10^{12}	9.5×10^{11}	1.5×10^{11}	1.7×10^{10}	8.7×10^{2}
In the hadron stopper	3.1×10^{12}	1.4×10^{12}	2.2×10^{11}	2.4×10^{10}	6.9×10^{2}
Collimator at the start of the decay tunnel	8.3×10^{12}	3.6×10^{12}	5.9×10^{11}	6.5×10^{10}	7.4×10^{3}
Reinforcement in the concrete of the cavern	6.5×10^{10}	2.8×10^{10}	4.6×10^{9}	5.1×10^{8}	6.6×10^{2}
Total	3.8×10^{13}	1.7×10^{13}	2.7×10^{12}	3.0×10^{11}	4.4×10^{5}

Table 5.25: *Activity of gamma emitting isotopes in the iron (NGS-99) after 10 years of operation and for different cooling times.*

Region	Total Activity in Bq after different cooling times				Specific activity in Bq/g after
	1 years	5 years	50 years	500 years	5 years
Around the target station	3.0×10^{12}	1.3×10^{12}	2.1×10^{11}	2.4×10^{10}	1.2×10^{4}
Aside the horn	1.6×10^{12}	6.8×10^{11}	1.1×10^{11}	1.2×10^{10}	8.4×10^{3}
In the TDX	8.8×10^{12}	3.8×10^{12}	6.2×10^{11}	6.9×10^{10}	1.1×10^{4}
Around the 1.He-tube	5.5×10^{12}	2.4×10^{12}	3.9×10^{11}	4.3×10^{10}	1.2×10^{4}
In the decay-pipe	3.7×10^{12}	1.6×10^{12}	2.6×10^{11}	2.9×10^{10}	1.5×10^{3}
In the hadron stopper	1.8×10^{12}	7.7×10^{11}	1.2×10^{11}	1.4×10^{10}	3.9×10^{2}
Collimator at the end of the target cavern	4.5×10^{12}	2.0×10^{12}	3.2×10^{11}	3.5×10^{10}	5.6×10^{3}
Reinforcement in the concrete of the cavern	3.8×10^{10}	1.7×10^{10}	2.7×10^{9}	3.0×10^{8}	3.9×10^{2}
Total	2.9×10^{13}	1.3×10^{13}	2.0×10^{12}	2.3×10^{11}	3.0×10^{5}

It should be noted that the activity in the iron of the decay-pipe of NGS-99 is nearly 70 % higher than in the design of NGS-98 whereas the activity in the iron of the hadron stopper is by 42% lower. This increase can be explained by the optimization of the horn and of the reflector and by the two omitted collimators after the target whereas the lower activity in the stopper of NGS-99 is due to the fact that the target box contains now 13 rods instead of 11.

Variation of the radioactivity in the iron regions which form an essential part of the civil engineering is illustrated in Figure 5.9 (NGS-98) and Figure 5.10 (NGS-99). During the optimization of the target cavern and the beam optics it turned out that the collimator at the beginning of the decay tunnel should be installed inside the target cavern. Therefore, this collimator is not an essential part of the civil engineering anymore and, consequently, not shown in Figure 5.10. The total amount of radioactivity of the shielding elements which are not essential parts of the civil engineering is now lower by more than a factor of 2.

The specific activities of all the iron comprising the shield remain significant, when compared with the Swiss exemption limit for general gamma-emitting isotopes of 1 Bq/g. These will have to be finally disposed of as radioactive waste. Furthermore, it should be noted that the specific activity of the items embedded in the civil engineering construction is also significantly above the exemption limit.

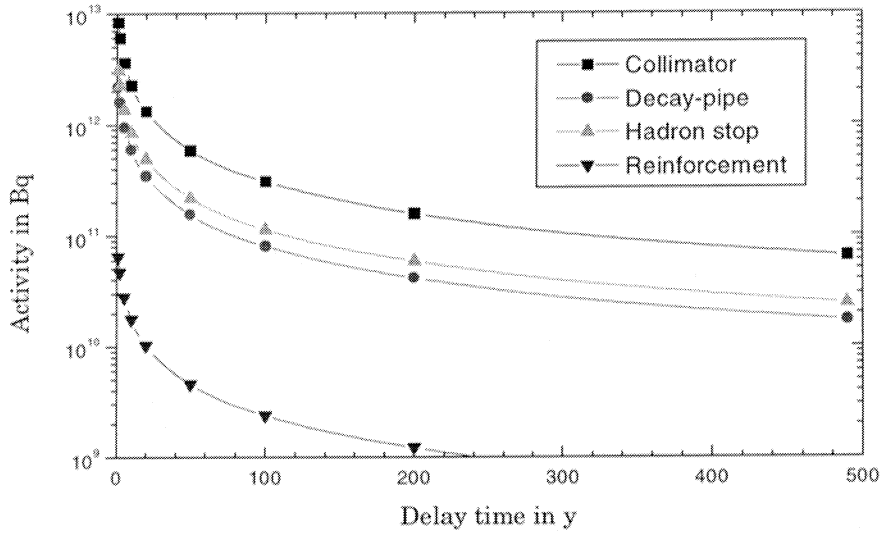

Figure 5.9: *Variation of the total activity in the iron of NGS-98 associated with the civil engineering with time after shutdown of the neutrino facitity.* ■ *represents the activity in the collimator at the start of the decay tunnel and* ▼ *the activity in the reinforcement in the concrete of the cavern.*

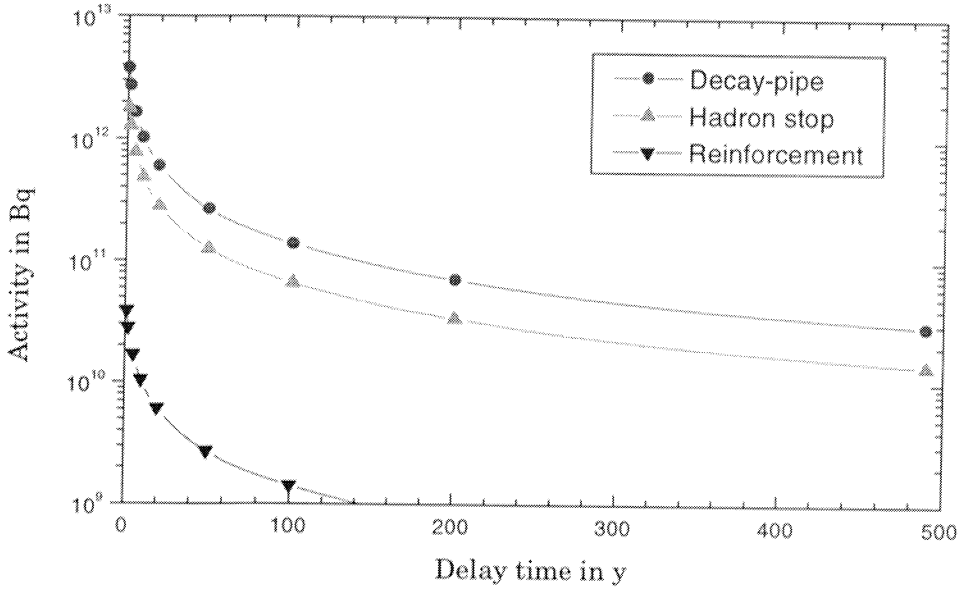

Figure 5.10: *Variation of the total activity in the iron of NGS-99 associated with the civil engineering with time after shutdown of the neutrino facility.*

In this study, the possibility of scoring directly the residual nuclei distribution in iron is also used for the calculation of the production of induced radioactivity in the iron pipe of the decay tunnel. FLUKA, in fact, gives the production rate of an isotope per primary particles, hence, the activity after 10 years of operation can be calculated by summing the activity produced in each period (200 days per year and 5×10^{19} protons on target per year) and multiplying it by the appropriate decay factor. In Table 5.26 the activity in the decay-pipe of NGS-99 after 10 years of operation and one year of cooling are given. A comparison of the tritium production of Table 5.23 with the result of the residual nuclei calculation shows that the ^{3}H activity decreased from $5.7\times10^{12}\times \exp(-\ln2/12.33) = 5.38\times10^{12}$ to 8.14×10^{11} Bq. This number seems to be more realistic since the first estimate is based on a high-energy production cross-section of 160 mbarn and does not include the increase of the cross-section in energy. The total activity in the decay-pipe is 1.87×10^{13} Bq whereby 66.3% due to ^{55}Fe, 20.4% due to ^{54}Mn, 8.3% due to ^{49}V and 4.4% due to ^{3}H. The sum of activity of these 4 isotopes is more than 99% of the total activity.

The radioactivity of gamma-emitting isotopes can be obtained from Table 5.26 by taking only those isotopes into account which emit gammas, see Table 5.27. It can be seen that the amount of γ-emitting isotopes is 3.91×10^{12} Bq which is about 20% of the total activity. By multiplying the activity of an isotope with the probability of the gamma emission and with the energy of the gamma the total emitted γ-energy of this isotope is given. Results of the dominant contributors to gamma energy emission are listed in Table 5.28 and it should be noted that ^{54}Mn contributes by more than 95% to the total energy of

3.33×10^{15} keV s^{-1} after 1 year cooling. Although ^{44}Sc has a half-life of only 3.9 hours it is still present in the iron after one year because it is reproduced by the decay of ^{44}Ti.

A comparison of the activity of gamma-emitting isotopes between the Sullivan-Overton formula and the FLUKA calculation is given in Figure 5.11. It provides an interesting view of the activity in the decay pipe of NGS-99 after several years of cooling. In addition, this figure presents the Swiss exemption limit for γ-emitting isotopes of the decay-pipe. As the mass of the decay-pipe is 1.1×10^{9} g the exemption limit of 1 Bq/g will be reached after 230 years of decay. By using the Sullivan-Overton formula the specific activity is still too high by more than a factor of ten after 500 years. As already initially mentioned, the Sullivan-Overton formula should be valid for iron for cooling times up to several years but it overestimates the activity on longer time scales significantly. Concerning the cooling time there is a perfect agreement between both calculation methods for the first two years but for cooling times greater than 10 years the overestimate is sometimes greater than 2 orders of magnitudes.

Table 5.26: *Radioactivity in the decay-pipe one year after shutdown.*

Radionuclide	Activity in Bq	Half-life
^{55}Fe	1.24×10^{13} ± 0.7 %	2.73 y
^{54}Mn	3.80×10^{12} ± 0.5 %	312.12 d
^{49}V	1.55×10^{12} ± 0.3 %	338.00 d
^{3}H	8.14×10^{11} ± 0.8 %	12.33 y
^{46}Sc	3.09×10^{10} ± 1 %	83.79 d
^{22}Na	1.71×10^{10} ± 6.2 %	2.60 y
^{56}Co	1.53×10^{10} ± 1.1 %	77.27 d
^{45}Ca	1.52×10^{10} ± 3.2 %	163.80 d
^{44}Sc	1.51×10^{10} ± 2.4 %	3.93 h
^{44}Ti	1.51×10^{10} ± 2.4 %	49.00 y
^{35}S	1.13×10^{10} ± 2.6 %	87.51 d
^{39}Ar	6.85×10^{9} ± 1.8 %	269.00 y
^{57}Co	4.95×10^{9} ± 7.7 %	271.79 d
^{42}K	1.85×10^{9} ± 1.9 %	12.36 h
^{42}Ar	1.85×10^{9} ± 1.9 %	32.90 y
^{32}P	1.27×10^{9} ± 4.3 %	14.26 d
^{32}Si	1.27×10^{9} ± 4.3 %	172.00 y
^{51}Cr	8.72×10^{8} ± 0.3 %	27.70 d
^{59}Fe	6.33×10^{8} ± 0.8 %	44.50 d
^{37}Ar	2.29×10^{8} ± 2.4 %	35.04 d
^{58}Co	6.00×10^{7} ± 7 %	70.82 d
^{33}P	1.93×10^{7} ± 3 %	25.34 d
^{7}Be	1.76×10^{7} ± 19 %	53.29 d
^{41}Ca	1.32×10^{7} ± 2.8 %	1.03×10^{5} y
^{53}Mn	1.27×10^{7} ± 0.8 %	3.74×10^{6} y
^{36}Cl	8.07×10^{6} ± 2.5 %	3.01×10^{5} y
^{14}C	3.35×10^{6} ± 24 %	5730 y
^{48}V	4.14×10^{5} ± 0.5 %	16 d
^{26}Al	1.63×10^{5} ± 4.3 %	7.4×10^{5} y
^{40}K	3.27×10^{3} ± 0.7 %	1.3×10^{9} y
^{10}Be	2.43×10^{3} ± 25 %	1.6×10^{6} y
^{52}Mn	4.85×10^{-8} ± 1.1 %	5.59 d
^{56}Ni	2.30×10^{-10} ± 50 %	5.90 d
^{47}Sc	1.92×10^{-14} ± 12 %	80.28 h
^{47}Ca	5.05×10^{-15} ± 12 %	4.54 d
Total	1.87×10^{13} ± 0.6 %	

Table 5.27: *Radioactivity in the decay-pipe from γ-emitting isotopes one year after shut-down.*

Radionuclide	Activity in Bq	Half-life
^{54}Mn	3.80×10^{12} ± 0.5 %	312.12 d
^{46}Sc	3.09×10^{10} ± 1 %	83.79 d
^{22}Na	1.71×10^{10} ± 6.2 %	2.60 y
^{56}Co	1.53×10^{10} ± 1.1 %	77.27 d
^{44}Sc	1.51×10^{10} ± 2.4 %	3.93 h
^{44}Ti	1.51×10^{10} ± 2.4 %	49.00 y
^{57}Co	4.95×10^{9} ± 7.7 %	271.79 d
^{42}K	1.85×10^{9} ± 1.9 %	12.36 h
^{51}Cr	8.72×10^{8} ± 0.3 %	27.70 d
^{59}Fe	6.33×10^{8} ± 0.8 %	44.50 d
^{58}Co	6.00×10^{7} ± 7 %	70.82 d
^{7}Be	1.76×10^{7} ± 19 %	53.29 d
^{48}V	4.14×10^{5} ± 0.5 %	16 d
^{26}Al	1.63×10^{5} ± 4.3 %	7.4×10^{5} y
^{40}K	3.27×10^{3} ± 0.7 %	1.3×10^{9} y
^{52}Mn	4.85×10^{-8} ± 1.1 %	5.59 d
^{56}Ni	2.30×10^{-10} ± 50 %	5.90 d
^{47}Sc	1.92×10^{-14} ± 12 %	80.28 h
^{47}Ca	5.05×10^{-15} ± 12 %	4.54 d
Total	3.91×10^{12} ± 0.6 %	

Table 5.28: *Main contributors to γ-energy emission in the decay-pipe one year after shut-down*

Radionuclide	Energy in keV s^{-1}	Half-life
^{54}Mn	3.18×10^{15} ± 0.5 %	312.12 d
^{46}Sc	6.22×10^{13} ± 1 %	83.79 d
^{56}Co	5.27×10^{13} ± 1.1 %	77.27 d
^{22}Na	2.17×10^{13} ± 6.2 %	2.60 y
^{44}Sc	1.77×10^{13} ± 2.4 %	3.93 h
^{44}Ti	2.10×10^{12} ± 2.4 %	49.00 y
^{59}Fe	7.52×10^{11} ± 0.8 %	44.50 d

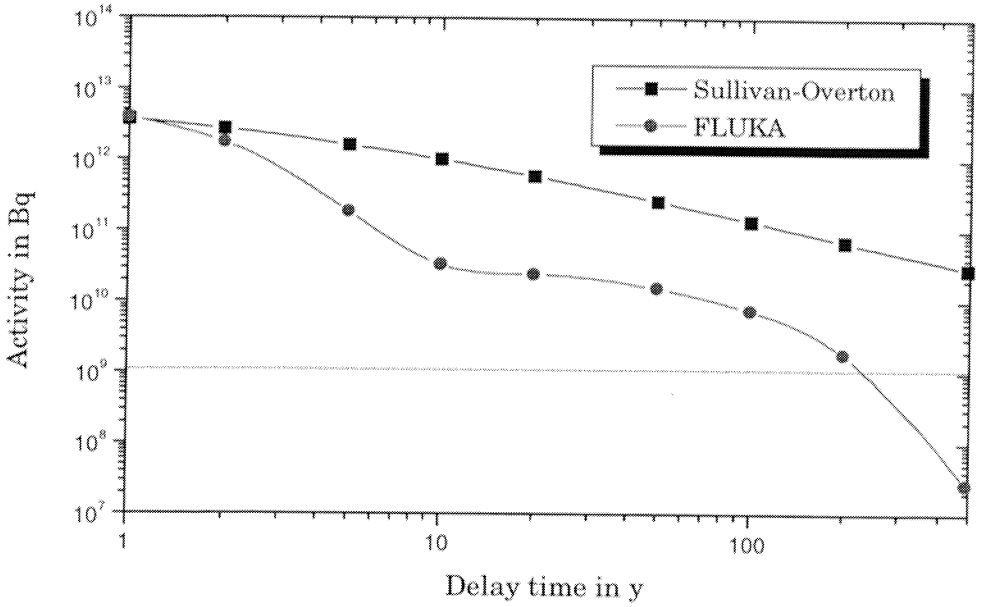

Figure 5.11: *Variation of the activity in the decay-pipe of NGS-99 with time after shutdown. The horizontal dashed line indicates the swiss exemption limit for general emitting γ-isotopes of the decay-pipe.*

5.7 Activity in the Graphite Core

The first component of the hadron stopper is a block of graphite which is used to diffuse the hadron cascade over a large volume to reduce the temperature gradient in the dump and take advantage of the better heat conductivity.

The measured high-energy cross-section for the production of ^{3}H and ^{7}Be in carbon are 20 mbarn and 10mbarn, respectively [Ilj91]. Since the inelastic cross-section used in the FLUKA program is 244 mbarn for carbon, the number of ^{3}H and ^{7}Be nuclei created per star is 0.082 and 0.041.

There are 74 stars per proton on target produced in the graphite core of the hadron-stopper (NGS-98) which weighs 33.4 t. The inventory of the induced radioactivity after 10 years of operation and after a further 10 and 50 years of decay is given in Table 5.29. In Table 5.30 the results of the NGS-99 calculations, in which 47 stars were scored in the core are summarized. The overall decrease in specific activity is due to two additional target rods which reduce the number of primary protons hitting the stopper.

Table 5.29: *Total activity in the graphite core for different decay times (NGS-98).*

Nuclide	0 years		10 years		50 years	
	Bq	Bq/g	Bq	Bq/g	Bq	Bq/g
^{3}H	4.18×10^{12}	1.25×10^{5}	2.39×10^{12}	7.16×10^{4}	2.52×10^{11}	7.54×10^{3}
^{7}Be	8.20×10^{12}	2.46×10^{5}	—	—	—	—
Total	1.38×10^{13}	4.13×10^{5}	2.39×10^{12}	7.16×10^{4}	2.52×10^{11}	7.54×10^{3}

Table 5.30: *Total activity in the graphite core for different decay times (NGS-99).*

Nuclide	0 years		10 years		50 years	
	Bq	Bq/g	Bq	Bq/g	Bq	Bq/g
^{3}H	2.66×10^{12}	7.96×10^{4}	1.52×10^{12}	4.56×10^{4}	1.60×10^{11}	4.79×10^{3}
^{7}Be	5.21×10^{12}	1.56×10^{5}	—	—	—	—
Total	7.87×10^{12}	2.36×10^{5}	1.52×10^{12}	4.56×10^{4}	1.60×10^{11}	4.79×10^{3}

The residual nuclei distribution was also scored in the graphite core of NGS-99. The results of the production of ^{3}H, ^{7}Be and ^{10}Be per proton and per star are listed in Table 5.31 which also includes the calculated production cross-section of these nuclei in graphite. Note that the numbers for radionuclides with half-lives less than 10 minutes and stable isotopes are not given.

Table 5.31: *Production of selected radionuclides in graphite.*

Nuclide	per proton	per star	σ in mbarn
^{3}H	4.17	0.089	21.7
^{7}Be	1.77	0.038	9.3
^{10}Be	0.80	0.017	4.2

It can easily be seen in this table that the data coincides with the measured data of 20 mbarn and 10 mbarn, respectively. In addition, a value of 4.2 mbarn is obtained for the production cross-section of ^{10}Be. This isotope only significantly contributes on very long time scales due to a half-life of 1.6×10^{6} years. The produced radioactivity of ^{10}Be after 10 years of operation is 5.8×10^{6} Bq or 0.17 Bq/g.

5.8 Activity in the Aluminum

The aluminum structures of the target cavern of NGS-98 are: the collimator COLL.2, the horn, the reflector, and the two helium pipes. The number of stars per proton on target are given in Table 5.32. In the NGS-99 design COLL.2 is omitted, the horn and the reflector are redesigned and the two helium pipes are enlarged. Moreover, the position of the horn and the reflector in the target cavern changed.

The high-energy cross-sections for the production of the long-lived radionuclides ^{3}H, ^{7}Be and ^{22}Na in aluminum are 55 mbarn, 9 mbarn and 12 mbarn, respectively [Nog91, Tob71]. Since the inelastic cross-section used in the FLUKA program is 440 mbarn for aluminum, the numbers of nuclei of ^{3}H, ^{7}Be and ^{22}Na created per star are 0.125, 0.021 and 0.027, respectively.

The inventory of long-lived induced radioactivity after 10 years of operation is given in Table 5.32 (NGS-98) and in Table 5.33 (NGS-99). The total activities after 10 years of decay after shutdown will be 3.6 times lower than the values of these tables. It is evident that all aluminum items will also have to be treated as radioactive waste after dismantling.

Table 5.32: *Radioactivity in the aluminum structures of the target cavern (NGS-98).*

Structure	Mass T	Number of Stars	Activity, Bq				Specific activity Bq/g
			^{3}H	^{7}Be	^{22}Na	Total	
COLL2	1.3	28	2.4×10^{12}	1.6×10^{12}	1.2×10^{12}	5.2×10^{12}	4.0×10^{6}
Horn-98	0.42	2.3	2.0×10^{13}	1.3×10^{11}	9.7×10^{10}	4.3×10^{11}	1.0×10^{6}
Reflector-98	0.60	0.93	8.0×10^{10}	5.3×10^{10}	3.9×10^{10}	1.7×10^{11}	2.9×10^{5}
Upstream He-pipe-98	0.85	1.3	1.1×10^{11}	7.4×10^{10}	5.5×10^{10}	2.4×10^{11}	2.8×10^{5}
Downstream He-pipe-98	0.14	0.082	7.1×10^{9}	4.7×10^{9}	3.5×10^{9}	1.5×10^{10}	1.1×10^{5}

Table 5.33: *Radioactivity in the aluminum structures of the target cavern (NGS-99).*

Structure	Mass t	Number of Stars	Activity, Bq ^{3}H	^{7}Be	^{22}Na	Total	Specific activity Bq/g
Horn-99	0.46	10.1	8.7×10^{11}	5.7×10^{11}	4.3×10^{11}	1.9×10^{12}	4.1×10^{6}
Horn frame-99	0.55	2.4	2.1×10^{11}	1.4×10^{11}	1.0×10^{11}	4.4×10^{11}	8.1×10^{5}
Reflector-99	0.93	1.7	1.5×10^{11}	9.6×10^{10}	7.2×10^{10}	3.1×10^{11}	3.4×10^{5}
Reflector frame-99	0.93	0.22	1.9×10^{10}	1.2×10^{10}	9.3×10^{9}	4.1×10^{10}	4.4×10^{4}
Upstream He-pipe-99	1.45	4.2	3.6×10^{11}	2.4×10^{11}	1.8×10^{11}	7.8×10^{11}	5.4×10^{5}
Downstream He-pipe-99	2.35	2.2	1.9×10^{11}	1.2×10^{11}	9.3×10^{10}	4.1×10^{11}	1.7×10^{5}

5.9 Activity in the Cooling Water

Water cooling of NGS-98 was foreseen for the horn, the reflector, the collimator COLL.1, the collimator COLL.2, and the hadron stopper whereas in the new design COLL.1 and COLL.2 are omitted due to beam optimization.

Table 5.34 gives details of the decay and production of isotopes produced by spallation in the water [ICRP83, Tho88]. The short half-life of ^{11}C and ^{13}N implies that their activity in the water will be essentially zero only several hours after the end of an irradiation. In contrast, the very long half-lives of ^{10}Be and ^{14}C mean that their contribution to the total activity in irradiated cooling water will be extremely small. Thus, the only two isotopes of importance are ^{3}H and ^{7}Be.

Table 5.34: *Data for isotopes produced in cooling water.*

Nuclide	Half-life	Principal decay mode(s) and energies	Atoms per star
^{3}H	12.4 y	100% β^-, $E_{ave}=5.68\times10^{-3}$ MeV	0.113
^{7}Be	53.3 d	89.7% Electron capture 10.3% γ, E=0.4776 MeV	0.032
^{10}Be	1.6×10^{6} y	100% β^-, $E_{ave}=2.52\times10^{-4}$ MeV	0.0031
^{11}C	20.4 min	99.8% β^+, $E_{ave}=3.86\times10^{-1}$ MeV	0.034
^{14}C	5730 y	100% β^-, $E_{ave}=4.95\times10^{-2}$ MeV	0.0065
^{13}N	9.97 min	99.8% β^+, $E_{ave}=4.92\times10^{-1}$ MeV	0.017

The cooling systems of the horn and the reflector are identical and the flow of water is 35 l/min for each item. However, in order to calculate the activity in the water, one needs the actual volume of water being irradiated. For both, the horn and the reflector, it is assumed here that there is a 2 mm skin of water surrounding the inner conductor of the elements giving volumes of about 5 liters and 13 liters for the horn-98 and reflector-98 respectively. The volume of the cooling water in horn-99 is again 5 liters and in the reflector-99 it is 15 liters. In both designs there is a 70 liter collector tank underneath the horn and the reflector at the same radial distance as the outer conductor. The star production in the water skin per cm^3 can then be estimated from the number of stars per cm^3 in the inner conductor by using equation

$$stars_{H_2O} = \frac{stars_{Al} \cdot \lambda_{Al}}{\lambda_{H_2O}}, \tag{5.13}$$

where λ is the inelastic interaction length which has a value of 38 cm in aluminum and 80 cm in water. If the star production in water was to be estimated from the star density in the air between the two conductors then its value would be lower by a factor of three. The production in the collector tank was estimated from the stars in the outer conductor. The contributions from the skin of water around the inner conductor and the collector tank are approximately equal.

The cooling circuit of the copper collimator COLL.1 and the aluminum collimator COLL.2 will be connected to the same closed circuit as that for the horn and reflector and the flow rate will be 1.5 m^3/h. It is assumed here that the water volume will not exceed 10% of the volume of the two collimators. As before, the star production can be estimated from the number of stars in the metal of the collimators. The star production in the different water circuits and the production of ^{3}H and ^{7}Be are given in Table 5.35.

Table 5.35: *Star and radionuclide production per proton in the different water circuits.*

Structure	Number of stars	Nuclide	
		^{3}H	^{7}Be
COLL1	2.9	3.3×10^{-1}	9.3×10^{-2}
COLL2	1.3	1.5×10^{-1}	4.3×10^{-2}
Horn-98	0.69	7.8×10^{-2}	2.2×10^{-2}
Reflector-98	0.27	3.1×10^{-2}	8.6×10^{-3}
Hadron stopper-98	0.032	3.6×10^{-3}	1.0×10^{-3}
Horn-99	1.41	1.6×10^{-1}	4.5×10^{-2}
Reflector-99	0.36	4.1×10^{-2}	1.2×10^{-2}
Hadron stopper-99	0.048	5.4×10^{-3}	1.5×10^{-3}

It should be noted that the crude estimates of the irradiated volumes of water presented here cannot underestimate the real cases by more than a factor of two, and are probably over-estimates.

The heat sink which will be placed under the graphite block of the hadron-stopper has a cross section of 280×20 cm^2 and a length of 5 m. It is cooled by 24 water pipes passing longitudinally, each of 4 cm diameter, giving a total water volume of 150 liters. The star production was estimated from the star density in the inner layer of iron surrounding the graphite core.

The activities of the two radionuclides after 200 days of operation are listed in Table 5.36, together with the total activities after decay times of 1 day, 100 days, and 1 year. The data of Table 5.36 shows that the level of H production is small compared to the CERN release constraint of 1.2×10^{15} Bq for ^{3}H. Cooling water is normally kept in closed circuits, but even if the cooling water from the target cavern was to be released to the drains 100 days after 200 days of operation, the amount of radioactivity of 1.2×10^{11} Bq (mainly Be) is still 3% of the CERN annual release constraint for ^{7}Be of 3.6×10^{12} Bq. In addition, the cooling water must be checked for its radioactivity concentration before release to the drains after passage through an ion-exchange resin to remove the ^{7}Be. Furthermore, care must be taken to filter corrosion products from the cooling water and at the same time to take the appropriate precautions in the disposal of these filters and ion-exchange resins.

Table 5.36: *Production of radioactivity in the cooling water with regard to the different locations after 200 days of operation and various decay times.*

Structure	Activity in Bq		Total activity in Bq			
	^{3}H	^{7}Be	0 days	1 day	100 days	1 year
COLL1	2.9×10^{10}	2.5×10^{11}	2.8×10^{11}	2.7×10^{11}	9.6×10^{10}	2.9×10^{10}
COLL2	1.3×10^{10}	1.1×10^{11}	1.3×10^{11}	1.3×10^{11}	4.4×10^{10}	1.3×10^{10}
Horn-98	6.8×10^{9}	5.9×10^{10}	6.6×10^{10}	6.5×10^{10}	2.3×10^{10}	6.9×10^{9}
Reflector-98	2.7×10^{9}	2.3×10^{10}	2.6×10^{11}	2.5×10^{10}	8.9×10^{9}	2.7×10^{9}
Total target cavern-98	5.1×10^{10}	4.4×10^{11}	4.9×10^{11}	4.9×10^{11}	1.7×10^{11}	5.2×10^{10}
Hadron stopper-98	3.2×10^{8}	2.7×10^{9}	3.1×10^{9}	3.0×10^{9}	1.1×10^{9}	3.2×10^{8}
Horn-99	1.4×10^{10}	1.2×10^{11}	1.4×10^{11}	1.3×10^{11}	4.7×10^{10}	1.4×10^{10}
Reflector-99	3.6×10^{9}	3.1×10^{10}	3.5×10^{11}	3.3×10^{10}	1.2×10^{10}	3.6×10^{9}
Hadron stopper-99	4.8×10^{8}	4.1×10^{9}	4.7×10^{9}	4.5×10^{9}	1.7×10^{9}	4.8×10^{8}

5.10 Activity in the Concrete Shielding Blocks

The activity in the additional concrete shielding blocks of NGS-99 in the target cavern can be calculated by using the total number of stars produced in these blocks. The positions of the concrete blocks are shown in the drawings of chapter 4. In Table 5.6 the yields per star of the dominant radionuclides produced in the concrete of the target cavern are depicted. The number of stars in the different shielding blocks are listed in Table 5.37.

Table 5.37: *Production of stars per proton in the concrete shielding blocks.*

Region	Stars
Below the horn	9
Edgeways of the horn	3
Around 1.He-pipe	6
Around 2.He-pipe	32
Total	51

The total activity can then be calculated by summing the production in each operating year and multiplying it with the appropriate decay factor. The results are given together with the activity of γ-emitters after shutdown with respect to different decay times, therefore, see Table 5.38.

Table 5.38: *Radioactivity in the concrete shielding blocks after shutdown with respect to different decay times.*

Decay time, y	Total activity, Bq	γ–activity, Bq	Specific γ-activity, Bq/g
0	2.58×10^{13}	1.14×10^{13}	6.17×10^{5}
1	3.35×10^{12}	4.98×10^{11}	2.70×10^{3}
5	1.31×10^{12}	1.44×10^{11}	7.80×10^{2}
10	7.53×10^{11}	3.77×10^{10}	2.05×10^{2}
100	2.69×10^{10}	8.90×10^{7}	4.83×10^{-1}

5.11 Activity in the Marble

With respect to high-energy accelerator shielding it is indispensable to choose shielding materials which are less susceptible to activation. Among the various kinds of shielding materials, marble shows radiation levels of induced radioactivity which are much lower than those of other shielding materials like iron or normal concrete [Yam80].

The isotope production in marble per star was scored with FLUKA and the results are shown in Table 5.39 but including only those isotopes with half-lives greater than several hours and those who significantly contribute to the radioactivity.

From the number of stars produced in the different marble blocks of NGS-99, see Table 5.40, the total radioactivity after the end of the neutrino operation, can again be calculated by adding the activity of each operational period multiplied by the appropriate decay factor. The results are given in Table 5.41 together with the γ-activity and it also shows that the marble will have to be disposed of as radioactive waste. The specific γ-activity of the marble of the table is an average of all marble shielding except the shielding around the iron block of the target-station. This structure has a specific γ-activity of 507 Bq/g after the end of the operation of the facility and it has only 0.88 Bq/g after 10 years of cooling. Hence, it can be handled as non-active material after 10 years whereas the other blocks still have to be considered as radioactive waste after 100 years.

Table 5.39: *Radioactive isotope production in marble.*

Radionuclide	Half-life	Atoms per star
^{3}H	12.4 y	0.04 ± 0.8%
^{7}Be	53.3 d	0.014 ± 1.4%
^{10}Be	1.6×10^{6} y	0.0077 ± 2.8%
^{14}C	5730 y	0.014 ± 0.2%
^{22}Na	2.60 y	0.0005 ± 6.0%
^{24}Na	15.0 h	0.00023 ± 3.5%
^{26}Al	7.16×10^{5} y	0.00064 ± 4.0%
^{32}Si	280 y	0.0037 ± 3.9%
^{32}P	14.3 d	0.0057 ± 2.5%
^{33}P	25.4 d	0.0074 ± 2.6%
^{35}S	87.4 d	0.0017 ± 5.4%
^{36}Cl	3.01×10^{5} y	0.027 ± 0.7%
^{37}Ar	35.0 d	0.077 ± 0.9%
^{39}Ar	269 y	0.01 ± 1.0%
^{42}Ar	33 y	0.0001 ± 8.0%
^{42}K	12.4 h	0.001 ± 8.1%
^{43}K	22.3 h	0.0011 ± 2.7%
^{41}Ca	1.03×10^{5} y	0.31 ± 0.6%
^{45}Ca	163 d	0.014 ± 0.7%

Table 5.40: *Production of stars per proton in the marble blocks.*

Region	Stars
Around the target	0.1
Edgeways of the horn	62
In front of the TDX	27
Total	89

Table 5.41: *Radioactivity in the marble blocks after shutdown and different decay times.*

Decay time, y	Total activity, Bq	γ–activity, Bq	Specific γ-activity, Bq/g
0	3.23×10^{13}	4.04×10^{12}	1.75×10^{6}
1	3.04×10^{12}	8.50×10^{10}	3.68×10^{3}
5	1.92×10^{12}	2.07×10^{10}	8.95×10^{2}
10	1.46×10^{12}	7.02×10^{9}	3.04×10^{2}
100	5.23×10^{10}	3.29×10^{8}	1.42×10^{1}

5.12 Dose-rates from Neutrinos

As the project developed, it has been thought necessary to turn to questions concerning the dose rates due to neutrinos at Gran Sasso (LBL) and the optional Short-Base-Line facility (SBL). This requires a precise knowledge of the expected neutrino fluxes, and of the conversion factors for neutrinos.

5.12.1 Neutrino Fluence

The predicted performance of the ν_μ at the SBL and the LBL facilities was calculated with FLUKA and results can be found in Table 5.42. The values of the fluences are integrated from 0 to 100 GeV. Compared to the NGS-98 values, a substantial increase of about a factor of 1.7 in the expected fluences is found. In addition, the energy distribution of the ν_μ is shown in Figure 5.12. It should be pointed out that appearance experiments at Gran Sasso typically do not want the ν_μ spectrum to extend much beyond 30 GeV because at higher energies background channels open up which could be difficult to separate from the ν_τ events. Consequently, the decrease in mean energy is also advantageous.

The calculations, especially for a LBL detector, are very time consuming. Primary 400 GeV protons and all the secondaries produced are tracked in each run through the entire beam line from the target until they interact, decay, or escape. A detailed description of the geometry and the magnetic field was implemented in each of the beam simulations. The neutrinos coming from secondaries produced in reinteractions are included in the neutrino spectrum. In order to collect sufficient events, in particular for the LBL detector, special decay biasing was used. For all unstable particles, except muons, the mean decay length in the laboratory frame was set to be 10 m when smaller than the physical decay length otherwise it was left unchanged. For muons the decay length was set to be 200 m. At the decay point according to the biased probability, Russian Roulette (i.e. random choice) decides whether the particle will actually survive or not after creation of the decay products. The latter are created in any case and their weight adjusted taking into account the ratio between biased and physical survival probability. A statistical accuracy of 1% or better is, thus, achieved at the price of some increase in local statistical fluctuations.

Neutrinos from the decays were scored at a LBL detector if they hit a circular area of 100 m radius which is significantly larger than any conceivable detector and it is only used to collect higher statistics. However, it is shown in [NGS98] that the radial distribution of the ν_μ fluence at Gran Sasso is nearly constant within the first 200 m. The sensitive area of a SBL detector was taken to be that of the proposed TOSCA detector, which is 1.44×1.44 m^2.

Table 5.42: *Predicted performance of the ν_μ beam at different locations.*

Location	ν_μ Fluence , $(m^2\ pot)^{-1}$	Mean ν_μ energy in GeV
SBL detector NGS-98	$1.09 \times 10^{-3} \pm 0.3\%$	27
LBL detector NGS-98	$4.39 \times 10^{-9} \pm 0.7\%$	24
SBL detector NGS-99	$1.85 \times 10^{-3} \pm 0.4\%$	19
LBL detector NGS-99	$7.45 \times 10^{-9} \pm 0.9\%$	17

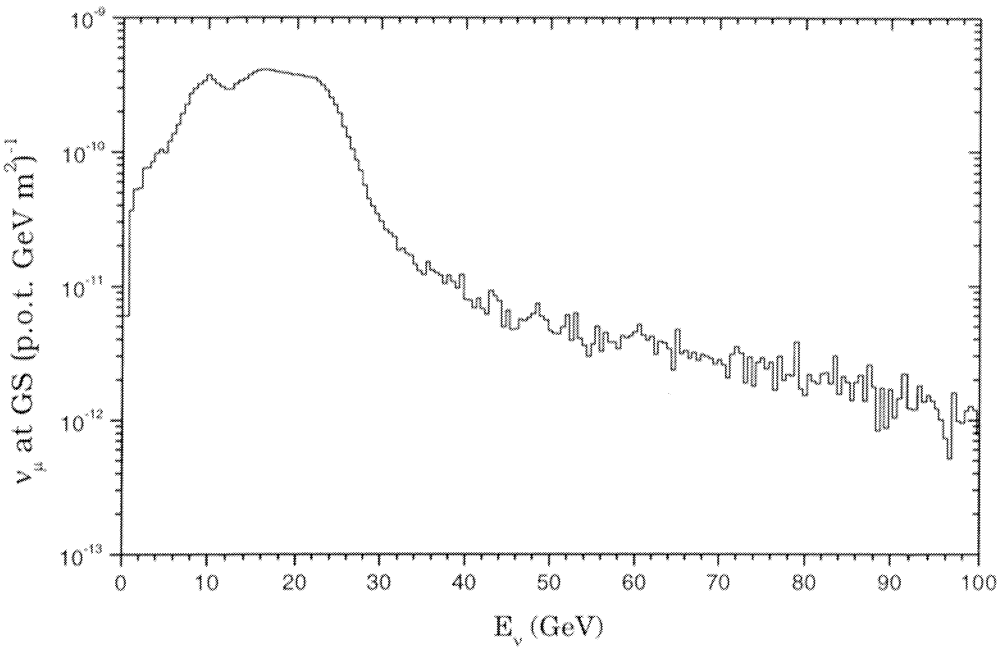

Figure 5.12: *Energy distribution of the ν_μ fluence at the LBL detector at Gran Sasso.*

5.12.2 Dose Rates for NGS-99

The neutrino fluence at the SBL and the LBL facilities of NGS-99 will be 1.85×10^{-3} m^{-2} and 7.45×10^{-9} m^{-2}, respectively, per proton on target. For 5×10^{12} protons per second on target, the fluence rates are 3.33×10^{9} cm^{-2} h^{-1} and 1.34×10^{4} cm^{-2} h^{-1}. The factor to convert neutrino fluence to dose equivalent at energies of around several tens of GeV is close to 10^{-18} Sv cm^2 as will be seen in Figure 5.13, which was supplied by N. Mokhov [Mok98]. Thus, the dose equivalent rates are 3.33×10^{-9} Sv/h at the SBL facility and 1.34×10^{-14} Sv/h at Gran Sasso. For comparison, natural background radiation levels are typically 100×10^{-9} Sv/h at the ground surface and are a factor of about three to four times lower than in a limestone underground environment. The levels of neutrinos are, thus, insignificant.

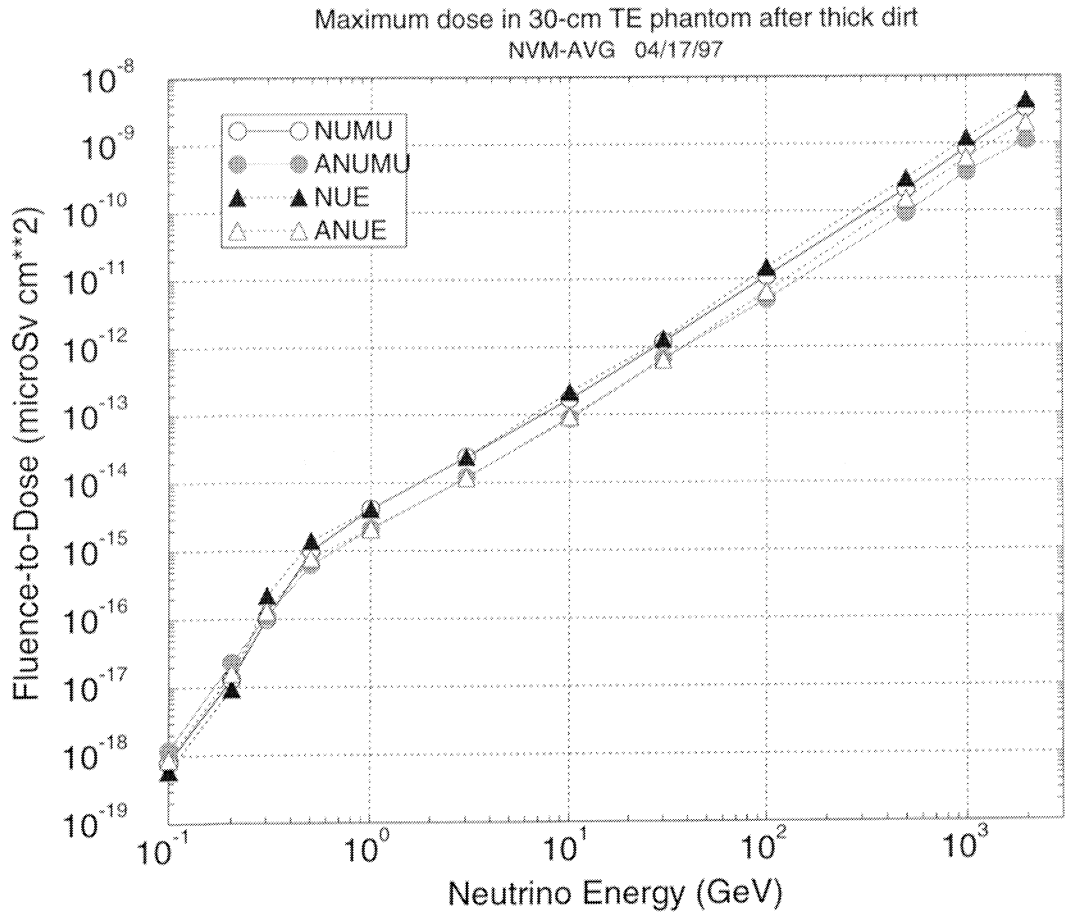

Figure 5.13: *Maximum dose equivalent as a function of energy for neutrinos in equilibrium with their secondaries [Mok98].*

Chapter 6

Summary

In the present work various radiation-related matters and explanations of the methodology that guided the design of the radiation protection system in the CERN neutrino beam to Gran Sasso are presented. Inherent in the designs is the fact that radiation protection is of the greatest importance in the target cavern, the decay tunnel, and the hadron stopper.

Few experimental data of the production of radioisotopes in molasse rock necessitated to irradiate several molasse samples with high-energy proton beams. The results of this experiment are, and will be used in the future as 'new' conversion factors between inelastic interactions in the molasse-rock and the production of radioactivity. A comprehensive study showed differences in the production of ^{3}H (factor 1.67 lower), ^{7}Be (factor 4 higher) and ^{46}Sc (factor 9 higher) compared to the values obtained from a previous irradiation experiment of 1987. It is important to stress that the chemical composition of glacial till was used for molasse in the Monte-Carlo calculations of the old experiment. Concerning the production of ^{45}Ca, ^{54}Mn, ^{152}Eu and ^{154}Eu there is a fairly good agreement between the old and the new conversion factors. Moreover, it is worth mentioning that in the new study 40 isotopes were identified whereas only 9 isotopes were found in the old measurement. Some of the new isotopes have half-lives greater than one year and although they are produced in small quantities, they contribute to the remaining radioactivity on longer times scales. In addition, the natural radioactivity of the molasse was measured and lower values were found than previously reported at CERN.

On the assumption that the facility will run for ten years at reference intensities, the radioactivity induced in the molasse around the underground structures and in the concrete of the structures themselves will decay to insignificant levels within 70-80 years after the end of target operation. The iron shielding around the target and the collimators have to be disposed of as radioactive waste. Parts of the massive iron in the hadron stopper will also require special disposal facilities.

The iron of the decay tunnel and the iron reinforcements in the concrete of the target chamber will probably stay in place at the end of the target operation. The reinforcements will reach insignificant levels of radioactivity within 50 years, but the time for the decay tunnel to reach similar levels will be of the order of 120 years.

The aluminum of the collimator COLL.2, the horn, the reflector, and the two helium-pipes in the target cavern will have significant, specific activities after 10 years of operation. Disposal of these items as radioactive waste must also be foreseen.

However, the activity in the graphite core of the hadron stopper will probably reach levels where normal disposal will be possible after ten years of decay.

Demineralised water in the cooling circuits of the horn, reflector, collimators, and hadron stopper will be kept in closed circuits. Emptying of these circuits will only take place after having measured the radioactivity contained. It is to be expected that the tritium concentrations will allow immediate emptying to drains, but the water must pass through a demineralising resin where any ^{7}Be and other radioisotopes will be removed before draining.

The air of the target chamber will remain within a closed circuit during operation. After targeting stops, a cooling-down period of several hours will be imposed before flushing the target chamber with fresh air. It will take at least several hours to flush all the original air from the target chamber. Control of the radioactivity by careful determination of delay time, flushing time, and transit time for the air to reach the exhaust stack from the target chamber will ensure that any radioactivity vented will be less than the relevant CERN Reference Release Constraints.

The radioactivity contained in the residual air of the decay tunnel and in the front part of the hadron stop area is significantly lower than the radioactivity in the target chamber. Estimates were made of the quantity of tritium which will be created in the closed helium-gas cooling circuit for the target and the helium containers in between the horn and reflector and the reflector and the end of the target chamber. Since the release of tritium from this source is much lower than the CERN reference value and, therefore, is of no radiological importance, the regular flushing of one of the helium circuits will not create significant release of tritium.

The drains in the target chamber will collect any ground-water that might seep into the excavation, as well as, any spillage water. Concerning, the radioactivity in the ground-water, even though at a low level, it is prudent to impose controls on the release of the drain-water. In addition to routine controls of the drain-water leaving the facility, water will not be released unless point controls have proven that the radioactivity in the water meets CERN Release Standards, only then, the drain water will be released. If the radioactivity exceeds the levels, then drain-water will have to be evaporated, as is done in some present CERN facilities, and the residue is disposed of as solid radioactive waste.

The expected dose-rates from neutrinos at the Gran-Sasso and an optional short base-line facility at CERN were calculated. A comparison with natural background radiation levels at the ground surface revealed much lower values, therefore, the levels from neutrinos are insignificant.

In June 1998 the Super-Kamiokande collaboration reported compelling evidence for neutrino oscillation. Their results indicated that the optimum neutrino energy for a beam produced at CERN may be lower than that of the preliminary NGS-98 version. As a consequence, the beam layout changed which required a complete redesign of the shielding around the beam components.

Estimates of the radiological parameters of concern for the environment and facility maintenance are revised according to the new reference parameters. The new shielding around the horn, decay tube etc. already takes into account the need to reduce doses received by personnel maintaining these components. Furthermore, the extra shielding also keeps the radioactivity induced in the air and the rock outside the target cavern per proton on target to values lower than those achieved in the study of 1998. However, the present project suggests that the upper limit of the number of protons on target could be up to 50% higher than before. This upper limit would be reached if the NGS beam were to run in dedicated mode (no other SPS users). Optimization studies are continuing.

Appendix A

Reference parameter list (NGS-98)

Proton Beam	
Maximum proton beam momentum (design)	450 GeV/c
Proton beam momentum (assumed for operation)	400 GeV/c
Proton beam normalized emittance (1σ)	12π mm mrad
β^+ at the focus (H and V)	2.5 m
→ minimum beam size/divergence (1σ)	0.27mm, 0.1mrad
Minimum repetition time (dedicated operation at 400 GeV/c)	7.2 s
Time between bursts	50 ms
Proton intensity (for hadron stop considerations)	5×10^{12} protons/sec, 200 days/year
Proton intensity (for environmental considerations)	5×10^{19} protons/y
Expected integrated number of protons per 200 days (" = 50 %), running with 2 subcycles for neutrinos and 16 % duty cycle for slow extraction	
at 350 GeV/c (SPS acc. limited)	3.4×10^{19} protons
at 400 GeV/c (SPS acc. + target limited)	3.0×10^{19} protons
at 450 GeV/c (graphite target limited)	2.0×10^{19} protons
Expected period of operation	10 years
Target Chamber	
Length of target chamber	115 m
Diameter of target chamber	6.5 m (int.)
Floor width of target chamber	5.6 m
enlargement at target (optional)	7.4 m
Crane capacity	10 t
Free height under crane hook	3.7 m
Beam height in target chamber	1.6 m
Diameter of neutrino service gallery	3.4 m (int.)
Distance of service gallery from cavern	6.0 m
Length of junction tunnel to target chamber	8 m
Distance of proton focus to entrance of decay tunnel	100 m
Target	
Start coordinate (w.r.t. proton focus)	-0.5 m

End coordinate (w.r.t. proton focus)	+1.5 m
Target material	carbon
Target rod length	10 cm
Diameter of rods	3 mm
Number of rods	11
Distance between rods	9 cm

Note: it is possible that a more compact target (i.e. more rods) will finally be used inside the defined space.

Collimators

COLL1 (at target exit)

Material	copper
Start coordinate (w.r.t. proton focus)	+1.70 m
End coordinate (w.r.t. proton focus)	+2.90 m
Cross-section: square	1×1m 2
Opening: cylindrical, radius such that limitation at exit is (seen from the proton focus)	±20 mrad

COLL2 (before the horn)

Material	aluminum
Start coordinate (w.r.t. proton focus)	+4.30 m
End coordinate (w.r.t. proton focus)	+7.00 m
Cross-section: cylindrical diameter	0.5 m
Opening: conical, opening angle seen from focus	±15 mrad

Horn and Reflector (dimensions referring to magnetic length):

Distance proton beam focus - horn entrance	7.85 m
Length of horn	6.65 m
Current in horn	120 kA
Distance proton beam focus - reflector entrance	80.35 m
Length of reflector	6.65 m
Current in reflector	120 kA

Collimator COLL3

Distance from proton beam focus to COLL3 entrance	25 m
Length of collimator	1.6 m
Opening of collimator	0.8×0.8 m^2

Decay Tunnel

Upstream end of decay tunnel (w.r.t. focus)	100 m

Length of decay tunnel	992 m
Diameter of decay tunnel (TBM)	3.50 m (ext.)
Length of decay pipe	994.5 m
Diameter of decay pipe (inner diam. steel pipe)	2.45 m (96 inch)
Wall thickness decay pipe	20 mm
Concrete filling around pipe	ca. 53 cm
Entrance window decay pipe: diameter	1 m,
	2 mm Titanium
Exit window decay pipe:	5 cm steel
Pressure in decay pipe (min.)	1-2 Torr
Pumping down time (max.)	2 weeks
Decay Pipe Collimator (iron)	
Start of collimator (w.r.t. proton beam focus)	100 m
Length of collimator	10 m
Inner diameter of collimator	1 m
Outer diameter of collimator (= inner diameter of shotcrete)	3.1 m
Hadron Stop and Muon Chambers	
Upstream end of hadron stop cavern (w.r.t. proton focus)	100 + 992 m
Length of hadron stop cavern	26 m
Diameter of hadron stop cavern	6 m (int.)
Length of hadron stop	18.2 m
Cross-section of hadron stop	$4\times4m^2$
Length of graphite insert	3 m
Cross-section of graphite insert	$2.6\times2.6\ m^2$
Wall thickness of Al box around graphite	0.1 m
Length of airgap upstream of hadron stop	0.25 m
Length of airgap downstream of hadron stop	5 m
(= length of first muon chamber)	
Length of "muon filter": Molasse	67 m
Length of 2nd muon chamber	3.5 m
Muon pit "service alcove" surface	$10\times4m^2$
Access gallery to hadron stop: diameter	3.1 m (int.)
Access gallery to 2nd muon pit: diameter	2.5 m (int.)
Short-baseline Experiment	
Distance proton focus to SBL cavern approx.	1850 m

Updated Reference Parameter List (NGS-99)

Proton Beam

Maximum proton beam momentum (design)	450 GeV/c
Proton beam momentum (assumed for operation)	400 GeV/c
Proton beam normalised emittance (1σ)	12π mm mrad
β^* at the focus (H and V)	2.5 m
$\rightarrow$ minimum beam size / maximum divergence (1σ)	0.27 mm, 0.1 mrad
Minimum repetition time (dedicated operation at 400 GeV/c)	6 s
Time between bursts 50 ms	
Proton intensity (for hadron stop considerations)	6×10^{12} protons/sec, 200 days/year
Proton intensity (for environmental considerations)	7.6×10^{19} protons/y
Expected integrated number of protons per year at 400 GeV/c	4.5×10^{19} protons
Expected period of operation 10 years	

Target Chamber

Length of target chamber	115 m
Diameter of target chamber	6.5 m (int.)
Floor width of target chamber	5.6 m
Enlargement at target (optional)	7.4 m
Crane capacity	10 t
Free height under crane hook	3.7 m
Beam height in target chamber	1.6 m
Diameter of neutrino service gallery	3.4 m (int.)
Distance of service gallery from cavern	6.0 m
Length of junction tunnel to target chamber	8 m
Distance of proton focus to entrance of decay tunnel	100 m

Target

Start coordinate (w.r.t. proton focus)	-0.5 m
End coordinate (w.r.t. proton focus)	+1.5 m
Target material carbon, density	1.81 g/cm^3
Target rod length	10 cm
Diameter of rods	4 mm
Number of rods	13
Distance between rods	5.5 cm

Note: the exact configuration of the 13 target rods is under investigation.

Helium tubes

Helium tube I

Start coordinate (w.r.t. proton focus)	11.00 m
End coordinate (w.r.t. proton focus)	42.00 m
Diameter first 6 m	0.80 m
Diameter remaining length	1.20 m

Helium tube II

Start coordinate (w.r.t. proton focus)	52.00 m
End coordinate (w.r.t. proton focus)	99.00 m
Diameter	1.20 m

Shielding / Collimation

Shielding around the target

Material	iron / marble
Start coordinate (w.r.t. proton focus)	-1.5 m
End coordinate (w.r.t. proton focus)	+1.7 m
Cross-section	rectangular
Opening for target box	60×60 cm^2
30 cm of marble added at downstream end of target	

Shielding around the horn

Shielding underneath the horn	40 cm concrete
Side walls of 30 cm marble / 20 cm iron / 30 cm concrete	
Height of walls	3.20 m
Left wall, start coordinate (w.r.t. proton focus)	2.30 m
Left wall, end coordinate	10.80 m
Right wall, start coordinate	2.00 m
Right wall, end coordinate	11.00 m

Shielding around helium tube I

Upstream shielding	0.50 m marble
Shielding collar, first 5 m	iron, 3×3m^2
opening	0.80×0.80 m^2
Shielding collar, remaining 25.5 m	0.20 m iron, 0.30 m concrete
opening	1.20×1.20 m^2
(Height of collar 2.70 m)	

Shielding along helium tube II	
Shielding underneath the tube	0.40 m concrete
Side walls height	3.20 m
Left wall distance to axis	1.00 m
Left wall thickness	0.80 m
Right wall distance to axis	1.00 m
Right wall thickness	0.80 m
Shielding collimator around helium tube II	
Start of shielding	85 m
Length of shielding	5 m
Inner diameter	1.20 m
Outer diameter	3.80 m (exception: downwards)

Horn and Reflector (dimensions referring to magnetic length):	
Distance proton beam focus - horn entrance	1.7 m
Length of horn	6.65 m
Current in horn	150 kA
Distance proton beam focus - reflector entrance	43.35 m
Length of reflector	6.65 m
Current in reflector	150 kA
Decay Tunnel	
Upstream end of decay tunnel (w.r.t. focus)	100 m
Length of decay tunnel	992 m
Diameter of decay tunnel (TBM)	3.50 m (ext.)
Length of decay pipe	994.5 m
Diameter of decay pipe (inner diam. steel pipe)	2.45 m (96 inch)
Wall thickness decay pipe	16 - 19 - 22 mm
Concrete filling around pipe	ca. 53 cm
Entrance window decay pipe diameter	1.40 m, 2 mm titanium T40
Protecting shutter (thickness)	3 cm steel
Exit window decay pipe	5 cm steel
Pressure in decay pipe (min.)	1-2 Torr
Pumping down time (max.)	2 weeks

Hadron Stop and Muon Chambers

Upstream end of hadron stop cavern (w.r.t. proton focus)	100 + 992 m
Length of hadron stop cavern	26 m
Diameter of hadron stop cavern	6 m (int.)
Length of hadron stop	18.2 m
Cross-section of hadron stop	$4\times4m^2$
Length of graphite insert	3 m
Cross-section of graphite insert	$2.6\times2.6\ m^2$
Wall thickness of aluminium box around graphite	0.1 m
Length of airgap upstream of hadron stop	0.25 m
Length of airgap downstream of hadron stop (= length of first muon chamber)	5 m
Length of "muon filter": Molasse	67 m
Length of 2nd muon chamber	3.5 m
Muon pit "service alcove" surface	$10\times4m^2$
Access gallery to hadron stop: diameter	3.1 m (int.)
Access gallery to 2nd muon pit: diameter	2.5 m (int.)

Appendix B

Decay data for isotopes produced in molasse

Nuclide	Half-life	Principal decay modes and energies	Production mode
^{3}H	12.35 y	100% β^-, $E_{ave} = 5.68 \times 10^{-3}$ MeV	Spallation
^{7}Be	53.3 d	100.0% Electron capture 10.3% γ, E = 0.4776 MeV	Spallation
^{10}Be	1.6×10^{6} y	100% β^-, $E_{ave} = 2.52 \times 10^{-1}$ MeV	Spallation
^{14}C	5730 y	100% β^-, $E_{ave} = 4.95 \times 10^{-2}$ MeV	Spallation
^{22}Na	2.60 y	99.4% β^+, $E_{ave} = 2.15 \times 10^{-1}$ MeV 99.4% γ, E = 1.2746 MeV	Spallation
^{24}Na	15.0 h	99.9% β^- $E_{ave} = 5.54 \times 10^{-1}$ MeV 99.9% γ, E = 2.754 MeV 100.0% γ, E = 1.3986 MeV	Thermal neutrons, spallation
^{26}Al	7.16×10^{5} y	81.8% β^+, $E_{ave} = 5.44 \times 10^{-1}$ MeV 2.5% γ, E = 1.13 MeV 99.8% γ, E = 1.81 MeV	Spallation
^{32}P	14.3 d	100% β^-, $E_{ave} = 6.95 \times 10^{-1}$ MeV	Spallation
^{33}P	25.4 d	100% β^-, $E_{ave} = 7.66 \times 10^{-2}$ MeV	Spallation
^{35}S	87.44 d	100% β^-, $E_{ave} = 4.88 \times 10^{-2}$ MeV	Thermal neutrons, spallation
^{36}Cl	3.01×10^{5} y	98.1% β^-, $E_{ave} = 2.79 \times 10^{-1}$ MeV	Thermal neutrons, spallation
^{37}Ar	35.02 d	100% E.C.	Thermal neutrons, spallation
^{39}Ar	269.0 y	100% β^-, $E_{ave} = 2.19 \times 10^{-1}$ MeV	Spallation, Thermal neutrons
^{41}Ca	1.03×10^{5} y	100% E.C.	Thermal neutrons
^{45}Ca	163 d	100.0% β^-, $E_{ave} = 7.72 \times 10^{-2}$ MeV	Thermal neutrons
^{46}Sc	83.3 d	100.0% β^-, $E_{ave} = 1.12 \times 10^{-1}$ MeV 100.0% γ, E = 0.889 MeV 100.0% γ, E = 1.120 MeV	Spallation
^{44}Ti	47.3 y	100% E.C. 94.4% γ, E = 0.068 MeV 96.0% γ, E = 0.0784 MeV	Spallation
^{48}V	16.0 d	50.0% β^+, $E_{ave} = 2.941 \times 10^{-1}$ MeV 100.0% γ, E = 0.984 MeV 100.0% γ, E = 1.312 MeV	Spallation
^{49}V	330 d	100% E.C.	Spallation
^{51}Cr	27.7 d	100% E.C. 9.83% γ, E = 0.32 MeV	Spallation, Thermal neutrons

Nuclide	Half-life	Principal decay modes and energies	Production mode
^{52}Mn	5.59 d	29.6% β^+ $E_{ave} = 2.416 \times 10^{-1}$ MeV 90.0% γ, E = 0.7442 MeV 94.5% γ, E = 0.9355MeV 90.0% γ, E = 0.7442 MeV 100.0% γ, E = 1.434 MeV	Spallation
^{54}Mn	313.0 d	100% E.C. 100.0% γ, E = 0.8348 MeV	Spallation
^{55}Fe	2.7 y	100% E.C.	Thermal neutrons, spallation
^{59}Fe	44.5 d	45.6% β^-, $E_{ave} = 8.095 \times 10^{-2}$ MeV 52.8% β^-, $E_{ave} = 1.492 \times 10^{-1}$ MeV 56.1% γ, E = 1.099 MeV 43.6% γ, E = 1.192 MeV	Thermal neutrons
^{56} Co	78.8 d	18.8% β^+ $E_{ave} = 6.321 \times 10^{-1}$ MeV 99.9% γ, E = 0.8468 MeV 14.1% γ, E = 1.038 MeV 67.0% γ, E = 1.238 MeV 15.5% γ, E = 1.771 MeV 16.7% γ, E = 2.599 MeV 7.4% γ, E = 3.254 MeV	Spallation
^{57}Co	271 d	100% E.C. 9.19% γ, E = 0.0144 MeV 85.6% γ, E = 0.1221 MeV 10.6% γ, E = 0.1365 MeV	Spallation
^{58}Co	70.8 d	15.0% β^+ $E_{ave} = 2.011 \times 10^{-1}$ MeV 99.4% γ, E = 0.8108MeV	Spallation
^{60}Co	5.27 y	99.9% β^-, $E_{ave} = 9.58 \times 10^{-2}$ MeV 99.9% γ, E = 1.173 MeV 100.0% γ, E = 1.332 MeV	Thermal neutrons
^{63}Ni	96.0 y	100.0% β^-, $E_{ave} = 1.713 \times 10^{-2}$ MeV	Thermal neutrons
^{65}Zn	244.0 d	50.7% γ, E = 1.116 MeV	Thermal neutrons
^{86}Rb	19.0 d	8.78% β^-, $E_{ave} = 2.326 \times 10^{-1}$ MeV 91.2% β^-, $E_{ave} = 7.094 \times 10^{-1}$ MeV 8.78% γ, E = 1.077 MeV	Thermal neutrons
^{134}Cs	2.06 y	70.1% β^-, $E_{ave} = 2.101 \times 10^{-1}$ MeV 15.4% γ, E = 0.569 MeV 97.6% γ, E = 0.6047 MeV 85.1% γ, E = 0.7958 MeV	Thermal neutrons
^{131}Ba	11.8 d	100% E.C. 29.1% γ, E = 0.124 MeV 19.9% γ, E = 0.216 MeV 13.3% γ, E = 0.372 MeV 43.8% γ, E = 0.496MeV	Thermal neutrons
^{133}Ba	10.7 y	100% E.C. 33.8% γ, E = 0.081 MeV 18.4% γ, E = 0.303 MeV 62.1% γ, E = 0.356 MeV 13.3% γ, E = 0.372 MeV	Thermal neutrons

Nuclide	Half-life	Principal decay modes and energies	Production mode
^{141}Ce	32.5 d	70.0% β^-, $E_{ave} = 1.298 \times 10^{-1}$ MeV 30.0% β^-, $E_{ave} = 1.809 \times 10^{-1}$ MeV 48.0% γ, E = 1.454 MeV	Thermal neutrons
^{152}Eu	13.3 y	1.8% β^-, $E_{ave} = 4.75 \times 10^{-2}$ MeV 2.4% β^-, $E_{ave} = 1.12 \times 10^{-1}$ MeV 13.8% β^-, $E_{ave} = 2.22 \times 10^{-1}$ MeV 8.3% β^-, $E_{ave} = 5.36 \times 10^{-1}$ MeV 28.4% γ, E = 0.1218 MeV 7.5% γ, E = 0.2447 MeV 26.6% γ, E = 0.3443 MeV 13.0% γ, E = 0.7789 MeV 10.2% γ, E = 1.086 MeV 13.6% γ, E = 1.112 MeV 20.9% γ, E = 1.408 MeV	Thermal neutrons
^{154}Eu	8.8 y	27.9% β^-, $E_{ave} = 6.88 \times 10^{-2}$ MeV 1.6% β^-, $E_{ave} = 1.01 \times 10^{-1}$ MeV 36.6% β^-, $E_{ave} = 1.76 \times 10^{-1}$ MeV 17.4% β^-, $E_{ave} = 2.76 \times 10^{-1}$ MeV 2.1% β^-, $E_{ave} = 3.28 \times 10^{-1}$ MeV 11.5% β^-, $E_{ave} = 6.95 \times 10^{-1}$ MeV 40.5% γ, E = 0.123 MeV 6.6% γ, E = 0.248 MeV 4.8% γ, E = 0.592 MeV 19.7% γ, E = 0.723 MeV 4.3% γ, E = 0.757 MeV 11.5% γ, E = 0.873 MeV 10.3% γ, E = 0.996 MeV 17.9% γ, E = 1.005 MeV 35.5% γ, E = 1.274 MeV	Thermal neutrons
^{160}Tb	72.3 d	10.0% β^-, $E_{ave} = 1.436 \times 10^{-1}$ MeV 47.0% β^-, $E_{ave} = 1.736 \times 10^{-1}$ MeV 26.8% β^-, $E_{ave} = 2.874 \times 10^{-1}$ MeV 13.2% γ, E = 0.0868 MeV 26.9% γ, E = 0.2986 MeV 29.5% γ, E = 0.8794 MeV 25.0% γ, E = 0.9662 MeV 15.2% γ, E = 1.178 MeV	Thermal neutrons
^{181}Hf	42.0 d	93.0% β^-, $E_{ave} = 1.189 \times 10^{-1}$ MeV 43.0% γ, E = 0.1330 MeV 14.0% γ, E = 0.3458 MeV 86.0% γ, E = 0.4820 MeV 25.0% γ, E = 0.9662MeV 15.2% γ, E = 1.178 MeV	Thermal neutrons
^{182}Ta	115.0 d	28.6% β^-, $E_{ave} = 7.149 \times 10^{-2}$ MeV 20.0% β^-, $E_{ave} = 1.285 \times 10^{-1}$ MeV 40.0% β^-, $E_{ave} = 1.570 \times 10^{-1}$ MeV 41.2% γ, E = 0.0678 MeV 14.0% γ, E = 0.1 MeV 34.9% γ, E = 1.121 MeV 16.4% γ, E = 1.189 MeV 27.3% γ, E = 1.221MeV 11.6% γ, E = 1.231 MeV	Thermal neutrons
^{233}Pa	27.0 d	14.6% β^-, $E_{ave} = 4.637 \times 10^{-2}$ MeV 26.9% β^-, $E_{ave} = 6.306 \times 10^{-2}$ MeV 30.9% β^-, $E_{ave} = 7.146 \times 10^{-2}$ MeV 36.0% γ, E = 0.312 MeV	Thermal neutrons

Appendix C

Neutron capture cross-sections

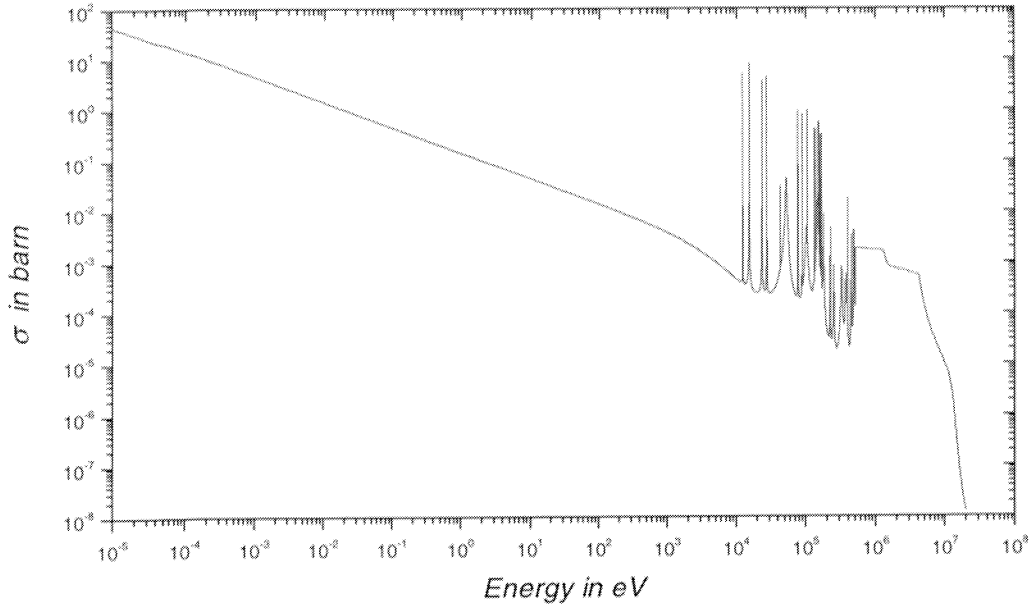

Figure 1: *^{44}Ca neutron capture cross-section.*

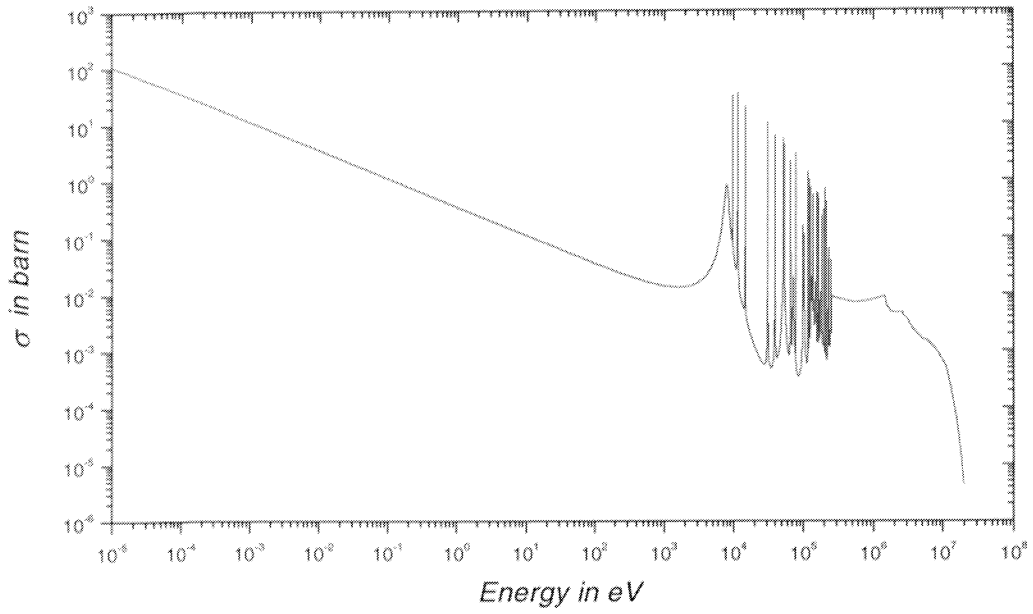

Figure 2: *^{54}Fe neutron capture cross-section.*

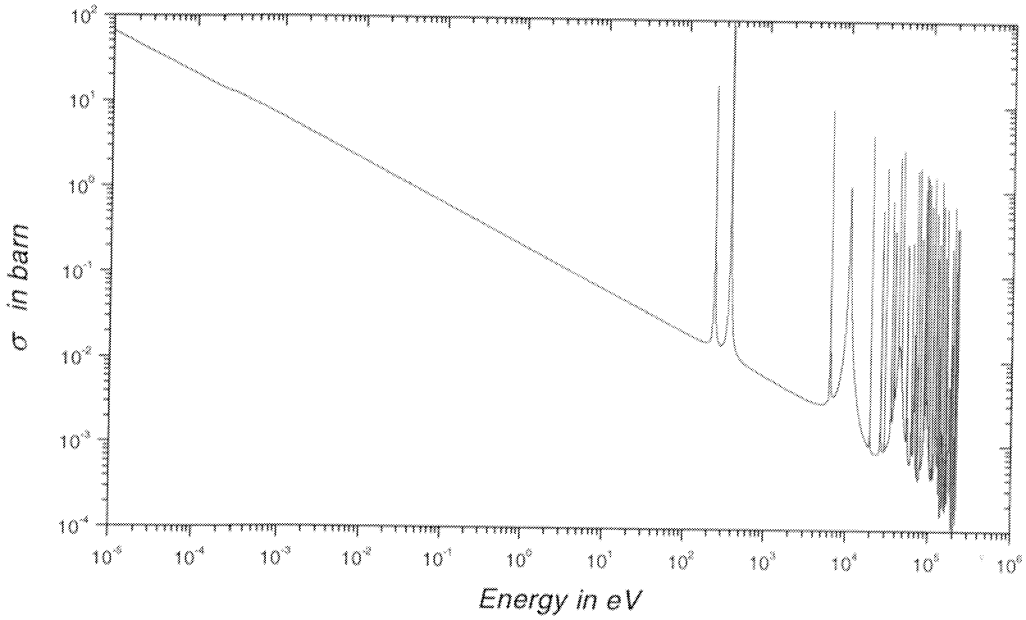

Figure 3: *^{58}Fe neutron capture cross-section.*

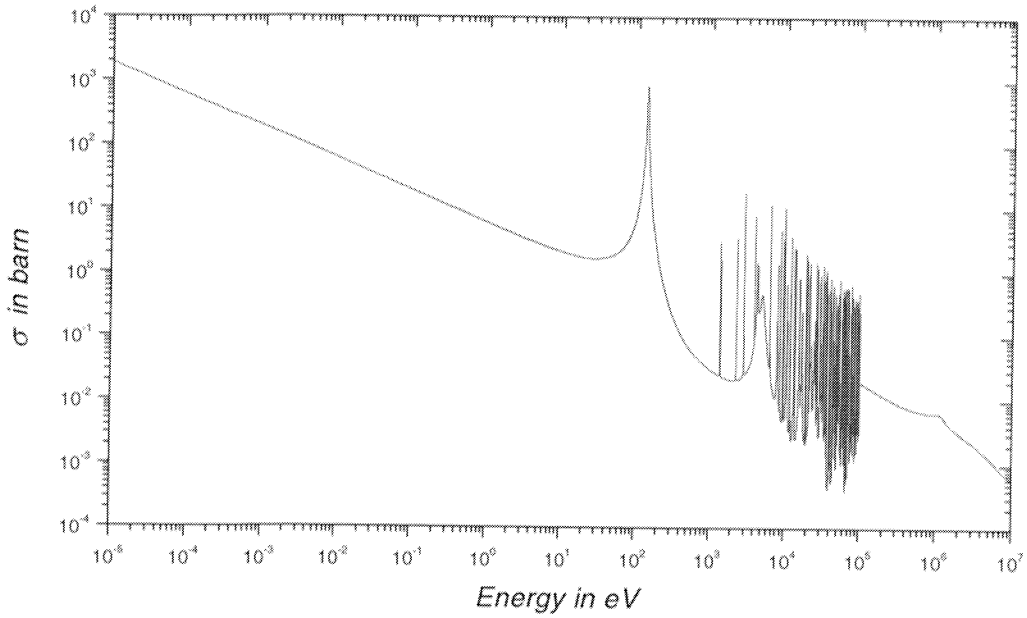

Figure 4: *^{59}Co neutron capture cross-section.*

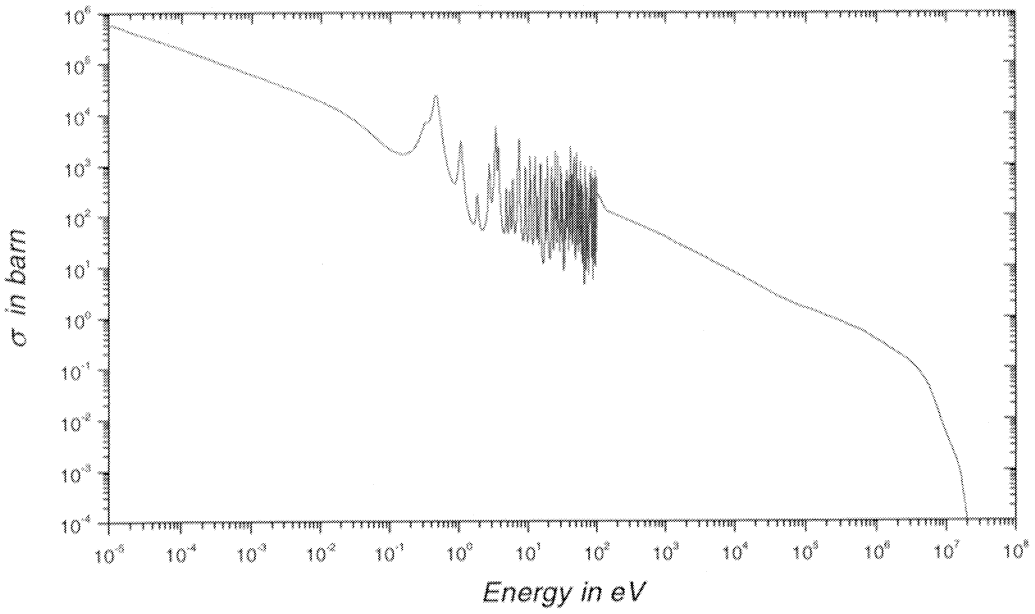

Figure 5: ^{151}Eu *neutron capture cross-section.*

Bibliography

[Aar94] P. A. Aarnio, A. Fasso, A. Ferrari, H.-J. Möhring, J. Ranft, P. R. Sala, G. R. Stevenson and J. M. Zazula, FLUKA: *hadronic benchmarks and applications.* In *Proceedings of the International Conference on Monte-Carlo Simulation in High Energy and Nuclear Physics, MC'93,* Tallahassee, U.S.A., 1993 (P. Dragovitsch, S. L. Linn and M. Burbank, Eds.), p. 88, World Scientific, Singapore, (1994).

[Abd96] D. N. Abdurashitov *et al.*, SAGE Coll., Phys. Rev. Lett. 77, 4708 (1996).

[All97] W. W. M. Allison *et al.*, Soudan Coll., Phys. Lett. B 391, 491 (1997).

[Als73] R. G. Alsmiller, Jr, and J. Barisch, *Shielding against the neutrons produced when 400 MeV electrons are incident on a thick copper target,* Particle Accelerators 5 (1973) 155-159.

[Amb95] M. Ambrosio *et al.*, *Nucl. Instrum. Methods* A 363, 604(1995).

[Amb98] M. Ambrosio *et al.*, MACRO Coll., Phys. Lett. B 434, 451 (1998).

[Aws71] M.Awschalom, *Calculation of the radionuclide production in the surroundings of the NAL neutrino laboratory*, Fermilab Internal report TM-292-A (1971).

[Aya97] A.S. Ayan *et al., A High Sensitivity Short Baseline Experiment to Search for* $\nu_\mu \rightarrow \nu_\tau$ *Oscillation,* CERN-SPSC/97-5 SPSC/I 213 (1997).

[Ath96] C. Athanassopoulos et *al.*, Lsnd Coll., Phys. Rev. Lett. 77, 3082 (1996).

[Bah98] J. N. Bahcall, S. Basau und M. H. Pinsonneault, Phys. Lett. B 433 1 (1998).

[Bak76] M. Baker and K. A. Ter-Martirosyan: *Gribov's Reggeon calculus: its physical basis and implications*, Phys. Rep. 28C (1976) 1

[Bar98] R. M. Barnett, *et al.*, E. Phys. J. C 3 23 (1998).

[Bec95] R. Becker-Szendy *et al.*, IMB Coll., Nucl. Phys. B (proc. Suppl.) 38, 331 (1995).

[Ber72] L. Bertochi: *Il Nuovo Cimento* 11A (1972) 45

[Bil98] S.M. Bilenky and C. Giunti, *Summary of the NOW '98 Phenomenology Working Group,* hep-ph/9906251.

[Bir94] C. Birattari, E. De Ponti, A. Esposito, A. Ferrari, M. Pelliccioni and M. Silari, *Measurements and characterization of high-energy neutron fields.* Nuclear Instruments and Methods A338 (1994) 534.

[Bir96] C. Birattari, E. De Ponti, A. Esposito, A. Ferrari, M. Magugliani, M. Pelliccioni, T. Rancati and M. Silari, *Measurements and simulations in high-energy neutron fields.* In *Proceedings of the 2nd Specialists' Meeting on Shielding Aspects of Accelerators, Targets and Irradiation Facilities,* CERN, Geneva, Switzerland, 1995, p. 171, published by OECD Nuclear Energy Agency, (1996).

[BNL] Brookhaven National Laboratory (BNL), http://www.dne.bnl.gov.

[Boh39] N. Bohr and J. A. Wheeler: Phys. Rev. 56 (1939) 426

[Bor72] T.B Borak, M.Awschalom, W. Fairman, F. Iwami and J. Sedlet, *The underground migration of radionuclides produced in soil near high energy proton accelerators*, Health Physics 23 (1972) 679-687.

[Cap94] A. Capella, U. Sukhatme, C. I. Tan and J. Tran Thanh Van: *Dual Parton Model*, Phys. Rep. 236 (1994) 225

[Cha75] H.-M. Chan, J. E. Paton and S. T. Tsou: *Diffractive scattering in the dual model*, Nucl. Phys. B86 (1975) 479

[Che76] G. F. Chew and C. Rosenzweig: *Asymptotic planarity: an S-matrix basis for the Okubo-Zweig-Iizuka rule*, Nucl. Phys. B104 (1976) 290

[Che78] G. F. Chew and C. Rosenzweig: *Dual topological unitarization: an ordered approach to hadron theory*, Phys. Rep. 41 (1978) 263

[Cle98] B. T. Cleveland et al., Astropys. J. 496, 505 (1998).

[Cow56] C.L. Cowan, Jr., F. Reines, F.B. Harrison, H.W. Kruse and A.D. McGuire , *Detection of the Free Neutrino: A Confirmation*, Science 124, 103 (1956).

[Cum74] J. B. Cumming, P. E. Haustein, R. W. Stoenner, L. Mausner and R. A. Naumann, *Spallation of Cu by 3.9 GeV ^{14}N ions and 3.9 GeV protons*. Phys. Rev. C10,739 (1974).

[Dav94] R. Davis, Prog. Part. Nucl. Phys. 32 (1994) 13.

[Daw98] I. Dawson and G. R. Stevenson, *Radiological Impact of the LHC Beam-dumps*, CERN Internal Report, CERN/TIS-RP/IR/98-27 (1998).

[EMPA] EMPA, Swiss Federal Laboratory for Materials Testing and Research, Überlandstrasse129, Ch-8600 Dübendorf.

[Eph67] M. Epherre and E. Gradsztajn: J. Physique 18 (1967) 48

[Fas97] A. Fassò, A. Ferrari, J. Ranft and P. R. Sala, *New developments in FLUKA modelling of hadronic and EM interactions*. In *Proceedings of The Third Workshop on Simulating Accelerator Radiation Environments (SARE-3),* KEK, Tsukuba, Japan, 1997, p. 32, (1997).

[Fer70] E. Fermi: Prog. Theor. Phys. 5 (1950) 1570

[Fer92] A. Ferrari, P. R. Sala, R. Guaraldi and F. Padoani, *An improved multiple scattering model for charged particle transport*. Nuclear Instruments and Methods B71 (1992) 412.

[Fer95] A. Ferrari and P. R. Sala: *Physics of Showers induced by Accelerator Beams*, Lecture given at the 1995 "Frederic Joliot" Summer School in Reactor Physics, Cadarache, France, 1995

[Fer96] A. Ferrari, J. Ranft, S. Roesler and P. R. Sala: *Cascade particles, nuclear evaporation, and residual nuclei in high energy hadron-nucleus interactions*, Z. Phys. C70 (1996) 413

[Fer96b] A. Ferrari and P. R. Sala: *The physics of high energy reactions*, in Proceedings of the Workshop on Nuclear Reaction Data and Nuclear Reactors Physics, Design and Safety, Miramare-Trieste, Italy, World Scientific in press, 1996

[Fer97] A. Ferrari, T. Rancati and P. R. Sala, *FLUKA applications in high-energy problems: from LHC to ICARUS and atmospheric showers.* In *Proceedings of The Third Workshop on Simulating Accelerator Radiation Environments (SARE-3),* KEK, Tsukuba, Japan, 1997, p. 165 (1997).

[Fer97b] A. Ferrari and P. R. Sala: *Intermediate and high energy models in FLUKA*: Improvements, benchmarks and applications, in Proceedings of the International Conference on Nuclear Data for Science and Technology, NDST-97, Trieste, Italy, in press, 1997

[Flu98] A. Fassò, A. Ferrari, J. Ranft and P. R. Sala, *FLUKA-98 Manual.*

[Fuk98a] Y. Fukuda et *al.*, Super-Kamiokande Coll., Phys. Rev. Lett. 81, 1158 (1998).

[Fuk98b] Y. Fukuda et *al.*, Super-Kamiokande Coll., Phys. Rev. Lett. 81, 1562 (1998).

[Fuk98c] Y. Fukuda et *al.*, Kamiokande Coll., Phys. Rev. Lett. B 335, 237 (1998).

[Gab72] T. A. Gabrial and R. J. Santoro, *Photon dose rates from the interaction of 200 GeV protons in iron and iron-lead beam stops*, Oak Ridge National Laboratory Report ORNL-TM-3945 (1972).

[Gla55] R. J. Glauber: Phys. Rev. 100 (1955) 242

[Gla69] S.L. Glashow, Nucl. Phys. 22, 597 (1961); S. Weinberg, Phys. Rev. Lett. 19, 1264 (1967); A. Salam, Proc. *Of the 8th Nobel Symposium on Elementary particle theory, relativistic groups and analyticity*, edited by N. Svartholm, 1969.

[Gri68] V. N. Gribov: *A reggeon diagram technique*, Sov. Phys. JETP 26 (1968) 414

[Gri70] V. N. Gribov: *Interaction of gamma quanta and electrons with nuclei at high energies*, Sov. Phys. JETP 30 (1970) 709

[Hag66] R. Hagedorn and J. Ranft: Suppl. Nuovo Cimento 6 (1966) 169.

[Ham96] W. Hampel *et al.*, GALLEX Coll., Phys. Rev. Lett. B 388, 384 (1996).

[Hän86] K. Hänssgen and J. Ranft: *The Monte Carlo code HADRIN to simulate inelastic hadron nucleon interactions at laboratory energies below 5 GeV*, Comp. Phys. Commun. 39 (1986) 37

[HealthPhysics] Bernard Shleien, *The Health Physics and Radiological Health Handbook*, (1992).

[Hir96] K. S. Hirata *et al.*, Kamiokande Coll., Phys. Rev. Lett. 77, 1683 (1996).

[Hoe75] M. Hoefert and A. Bonifas, *Measurement of radiation parameters for the prediction of dose rates from induced radioactivity*, CERN Internal Report HP-75-148 (1975).

[Hoe97] M. Höfert. L. E. Moritz and G. R. Stevenson, *Impact radiologique de project LHC sur l'environnement,* CERN Divisional Report CERN/TIS-RP/97-06 (1997).

[Huh96] M.Huhtinen, L. E. Moritz, K. M. Potter, S. Rollet and G. R. Stevenson, *Radiological implications of the release of air from the LHC experimental regions*, CERN Divisional Report CERN/TIS-RP/96-06 (1996).

[Huh97] M. Huhtinen, *Determination of Cross Sections for Assessments of Air Activation at LHC*, CERN/TIS-RP/TM/96-29 (1997).

[Huh98] M. Huhtinen and P. A. Aarnio, *Production of long-lived radionuclides in CMS*, CMS Note 1998/044.

[IAE] IAEA's Nuclear Data Centre, http://www-nds.iaea.or.at/.

[ICA98] *Icarus-like technology for long baseline neutrino oscillations*, by the ICARUS Coll., ICARUS-TM-98/16.

[ICR83] ICRP Publication 38, *Radionuclide transformations, energy and intensity of emissions*, International Commission on Radiological Protection, Pergamon Press [Oxford and Chambridge] (1983).

[Ilj91] A. S. Iljinov, V. G. Semenov, M. P. Semenova, N. B. Sobolevsky and L. V. Udovenko, *Production of radionuclides at intermediate energies a) Interaction of protons with targets from He to Br*, Landolt-Börnstein Numerical Data and Functional Relationships in Science and Technology, New Series, Group 1: Nuclear and Particle Physics, Volume 13, Editor H. Schopper, Springer-Verlag (1991).

[Iso] Isotope Explorer from the LBNL-Lund collaboration http://ie.lbl.gov/endsf/; general tool for displaying ENSDF-formatted nuclear data.

[Lel] Luigi di Lella, *Neutrino oscillations*, CERN,Geneva, Switzerland.

[Mak62] Z. Maki *et al.*, *Progr. Theor. Phys.28* (1962) 870.

[Mok98] N. Mokhov, *Private Communication.*

[NGS98] G. Acquistapace *et al.*, *The CERN Neutrino Beam to Gran Sasso, Report*, CERN 98-02 and INFN/AE-98/05.

[NGS99] *The CERN Neutrino beam to Gran Sasso (NGS), Addendum to report*, CERN 98-02, INFN/AE-98/05, CERN-SL/99-034(DI) INFN/AE-99/05

[NIC98] *Sensitivity to long baseline neutrino oscillations of a large mass calorimatric and spectrometric detector (NICE)*, CERN/SPSC 98-34.

[NDE] Nuclear Data Evaluation Lab, http://hpngp01.kaeri.re.kr/.

[Nog91] M. Noguchi, T. Miura, K. Kondo, T. Suzuki, Y. Oki, M. Takasaki, K. H. Tanaka and M. Ieiri, *Production cross-sections of tritium in high-energy nuclear reactions with 12 GeV protons*, Appl. Radiat. Isot. 42 (1991) 577.

[OPE98] *The OPERA* ν_τ *appearance experiment in the CERN-Gran Sasso neutrino beam*, CERN/SPSC 98-25.

[Pir96] F. Pirotte, M. Silari and L. Ulrici, *Induced radioactivity in concrete and rock in BA4 and TCC6 (BA7),* CERN Internal Report CERN/TIS–RP/IR/96–03 (1996).

[Pon58] B. Pontecorvo, *Sov. Phys. JETP 6* (1958) 429.

[Raf97] G. G. Raffelt, *Neutrino Masses in Astrophysics and Cosmology*, Contribution to the Proceedings of the 5th International Workshop on Topics in Astroparticles and Undergroundphysics, Laboratori Nazionale del Gran Sasso, Italy, 7-11 September 1997

[Ran66] J. Ranft: *Estimation of radiation problems around high energy accelerators using calculations of the hadronic cascade in matter*, Particle Accelerators 3 (1972) 129

[Ran70] J. Ranft: *Monte Carlo calculation of energy deposition by the nucleon-meson cascade and total-absoption nuclear cascade (TANC) counters*, Nucl. Instrum. Methods 81 (1970) 29

[Ran89] J. Ranft: Z. Phys. C43 (1989) 439

[Roe93] S. Roesler and G. R. Stevenson, July 1993, *CERN-CEC experiments: calculation of hadron energy spectra from tracklength distributions using FLUKA*, CERN Internal Report CERN-TIS-RP/IR/93-47 (1993).

[Rub95] C. Rubbia, Nucl. Instrum. Methods A 363, 604 (1995).

[Sal94] P. R. Sala and A. Ferrari: *A new model for hadronic interactions at intermediate energies for the FLUKA code*, in Proceedings of the International Conference onMonte Carlo Simulation in High Energy and Nuclear Physics, MC'93, Tallahassee, U.S.A., 1993, ed. by P. Dragovitsch, S. L. Linn and M. Burbank, World Scientific, Singapore, p. 277, 1994

[Sta73] G. B. Stapleton et R. H. Thomas, *The effect of sorption on the migration of ^{7}Be from high energy accelerator constructed on a chalk site*, Water research 7 (1973) 1259.

[Ste71] G. R. Stevenson, *Estimates of tritium and other hydrogen isotopes production in the helium of superconducting synchrotron magnets*, Rutherford Laboratory Internal Report RP/PN/59 (1971).

[Ste89] G. R. Stevenson and R. H. Thomas (eds.), *Radiological considerations for the enviroment around the LHC*, Minutes of a Workshop, 22-26th May 1989, CERN Divisional Report CERN-TIS/89-19 (LHC note 115) (1989).

[Sto75] L. Stodolsky: *Formation Zone Description in Multiproduction*, in Proceedings of the VIth International Colloquium on Multiparticle Reactions, Oxford, U.K., p. 577, 1975.

[Sul65] A. H. Sullivan and T. R. Overton, *Time variation of the dose rate from induced radioactivity induced in high-energy particle accelerators*, Health Physics 11 (1965) 1101.

[Sul87] A. H. Sullivan, *Ground activation around the AA and ACOL target areas,* Internal report CERN TIS-RP/IR/87-34.

[Sul92] A. Sullivan, *A guide to Radiation and Radioactivity Levels near High Energy Particle Accelerators*, Nucl. Tech. Publ. (1992).

[Tho88] R. H. Thomas and G. R. Stevenson, *Radiological safety aspects of the operation of proton accelerators*, Technical Report Series No.283, IAEA Vienna (1988).

[Tob71] Tobailem, C-H. de Lassus St Genies et L. Leveque, *Sections efficace des réactions nucléaires induites par protons, deutons, particules alpha, I. Réactions nucléaites moniteurs,* Saclay Report CEA-N-1466(1) (1971).

[UN88] United Nations Scientific Committee on the Effects of Atomic Radiation, *Sources, Effects and Risks of Ionizing Radiation,* 1988 Report to the General Assembly, with annexes.

[Voj98] P.Vojtyla, *Calculation of the effective dose to the public due to releases from the CERN Meyrin site implementing the Swiss directive HSK-R-41,* CERN/TIS-TE/98-20 (1998).

[Wei37] V. F. Weisskopf: Phys. Rev. 52 (1937) 295.

[Wet81] H. Wetzig, K. Hänßgen, J. Ranft, *Monte-Carlo simulation of elastic hadron nucleus reactions with the computer code NUCREL,* KMU-HEP 81-07 (1981).

[Yam80] C. Yamaguchi and M. Höfert, *Induced radioactivity from Marble and $CaCO_3$ irradiated by 19 GeV/c protons: Gamma and beta spectroscopy,* CERN, HS-Division Report HS-RP/054 (1980).

[Yps96] T. Ypsilantis et al., Preprint LPC/96-01, CERN-LAA/96-13.

Acknowledgments

Many people contributed to the successful completion of this doctoral thesis.

First, I am indebted to Dr. Graham Stevenson, for giving me the opportunity to work on this thesis at CERN. This work would not have been possible without his assistance and continuous support.

I would like to thank my supervisor Prof. Dr. Ewald Schachinger who supported and supervised my work.

Special thanks go to my colleagues Stefan Roesler, Ian Dawson and to my brother Helmut Vincke. Numerous fruitful and crucial discussions with them influenced my work tremendously.

I would like to acknowledge the collaboration with the CERN/INFN working group and especially with colleagues from the beam optics group.

I would like to thank the authors of the current FLUKA program, Dr. A. Fassò, Dr. A. Ferrari, Dr. J. Ranft and Dr. P. R. Sala for providing the FLUKA code.

A special word of thanks is due to Dr. N. Mokhov of Fermilab for permission to use his published work on dose conversion factors for neutrinos.

Finally, I am grateful to my parents for their encouragement and support.